NAGR-14-005-181

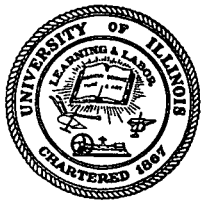

UNIVERSITY OF ILLINOIS
URBANA

(NASA-CR-176648) ROCKET EXPERIMENTS FOR SPECTRAL ESTIMATION OF ELECTRON DENSITY FINE STRUCTURE IN THE AURORAL AND EQUATORIAL IONOSPHERE AND PRELIMINARY RESULTS (Illinois Univ.) 164 p HC A08/MF A01 CSCL 04A G3/46 08686
N86-22026
Unclas

AERONOMY REPORT NO. 119

ROCKET EXPERIMENTS FOR SPECTRAL ESTIMATION OF ELECTRON DENSITY FINE STRUCTURE IN THE AURORAL AND EQUATORIAL IONOSPHERE AND PRELIMINARY RESULTS

by
B. A. Tomei
L. G. Smith

APR 1986
RECEIVED
NASA STI FACILITY
ACCESS DEPT.

January 1, 1986

Library of Congress ISSN 0568-0581

Aeronomy Laboratory
Department of Electrical and Computer Engineering
University of Illinois
Urbana, Illinois

Supported by
National Aeronautics and Space Administration

UILU-ENG-86-2502

A E R O N O M Y R E P O R T

N O. 119

ROCKET EXPERIMENTS FOR SPECTRAL ESTIMATION OF ELECTRON DENSITY FINE STRUCTURE IN THE AURORAL AND EQUATORIAL IONOSPHERE AND PRELIMINARY RESULTS

by

B. A. Tomei
L. G. Smith

January 1, 1986

Supported by
National Aeronautics
and Space Administration
Grant NGR 14-005-181

Aeronomy Laboratory
Department of Electrical and
Computer Engineering
University of Illinois
Urbana, Illinois

ABSTRACT

Sounding rockets equipped to monitor electron density and its fine structure were launched into the auroral and equatorial ionosphere in 1980 and 1983, respectively. The measurement electronics are based on the Langmuir probe and are described in detail. An approach to the spectral analysis of the density irregularities is addressed and a software algorithm implementing the approach is given. Preliminary results of the analysis are presented.

PRECEDING PAGE BLANK NOT FILMED

TABLE OF CONTENTS

PRECEDING PAGE BLANK NOT FILMED

TABLE OF CONTENTS (Continued)

TABLE OF CONTENTS (Continued)

LIST OF TABLES

LIST OF FIGURES

LIST OF FIGURES (Continued)

LIST OF FIGURES (Continued)

1. INTRODUCTION

Many characteristics of the ionosphere have been investigated in order to increase the understanding of the mechanisms determining its behavior. Of considerable interest in recent years are irregularities in the number density of electrons and ions, primarily as indicators of the physical phenomena generating these irregularities. Emphasis has been placed on the study of sporadic-E, spread-F and the electrojet, especially in the equatorial and auroral regions where the plasma density structure shows the greatest complexity.

Measurements of electron density fine structure have been obtained with several experimental techniques. The most popular techniques involve ground-based radar sensing, in-situ probes located on sounding rockets, balloons and satellites. An overview of the experimental and theoretical work on ionospheric irregularities in past years has been presented by FEJER AND KELLY [1980].

Two major campaigns supported by the Aeronomy Laboratory of the University of Illinois under the sponsorship of NASA were undertaken to investigate the ionosphere in 1980 and 1983. The Energy Budget Campaign, a coordinated study of sources and sinks of energy in the auroral zone, took place at a launch site near Kiruna, Sweden. The Aeronomy laboratory participated with three payloads containing Langmuir probes for the measurement of electron density irregularities. Project Condor, a coordinated study of the equatorial ionosphere, occurred at Punta Lobos Rocket Range near Chilca, Peru where two launches carried payloads prepared by the Aeronomy Laboratory, both containing nose-tip

Langmuir probes. Although each payload contained varied experiments to measure electron density, electron temperature and energetic particle precipitation, the major thrust of this report is the discussion of the methods used to measure electron-density irregularities on these payloads and the analysis of the spatial characteristics of the fine structure using the techniques of spectral estimation.

The following report details, in Chapter 2, the experiments implemented for measurement of electron-density irregularities in the auroral ionosphere (Energy Budget Campaign) and in the equatorial ionosphere (Project Condor). Chapter 3 describes the techniques of spectral estimation as applied to the fine structure experiment and the software developed for the analysis. Chapters 4 and 5 present preliminary results obtained from spectral estimation of the data from the two campaigns along with possible interpretations. The report concludes with a summary of results and suggestions for future work.

2. PROBE FINE STRUCTURE EXPERIMENT

2.1 General Description

The fine structure experiment is basically an extension of the experiment which has been used for measuring ambient electron densities versus altitude. This particular experiment is based upon the DC probe experiment developed by SMITH [1964, 1967] used to measure electron densities in the 50 to 200 km altitude range. PRAKASH ET AL. [1972] adapted the experiment to also measure electron-density irregularities. For the payloads described herein, the Langmuir probe serves as the basis for the experiments measuring electron density, electron temperature, and electron density fine structure. The following description, however, will deal primarily with the fine structure measurements.

A block diagram of the fine structure experiment used in the Energy Budget Campaign is shown in Figure 2.1. The experiment consists of two boom-mounted Langmuir probes connected in parallel, a sweep generator, a logarithmic electrometer, and an AC amplifier. The sweep generator provides the voltage reference to the probes for the electron density and temperature measurements. The specific voltage profile used is shown in Figure 2.2. The voltage sweeps from -1.35 V to 4.05 V in 0.3 seconds and then remains constant at 4.05 V for 1.7 seconds. The ramped portion allows measurement of the electron temperature as described in ZIMMERMAN AND SMITH [1980], while the electron density and fine structure are monitored during the constant voltage portion. The

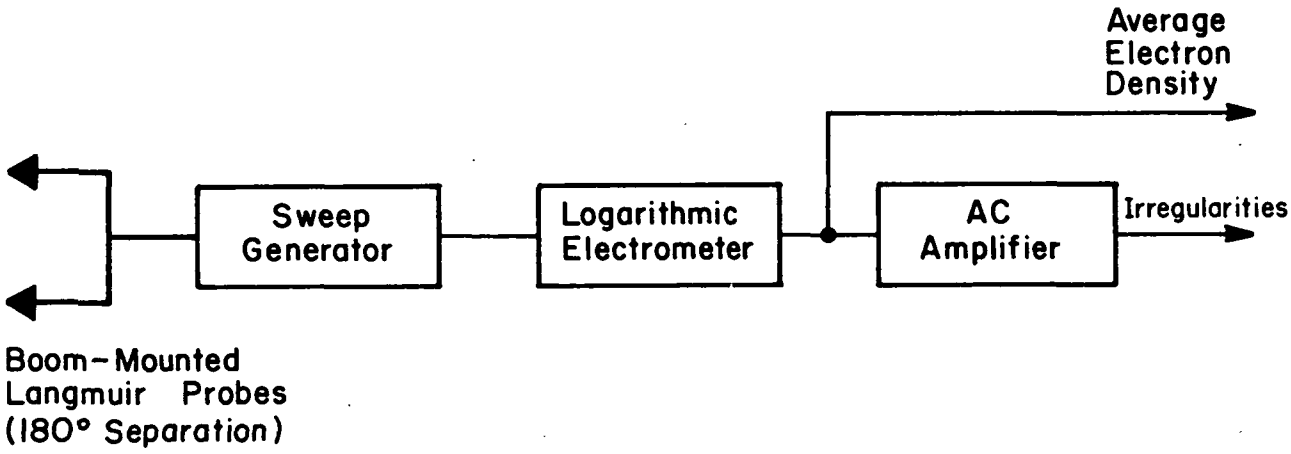

Figure 2.1. Block diagram of the electron density probe and fine structure experiment used in the Engergy Budget Campaign.

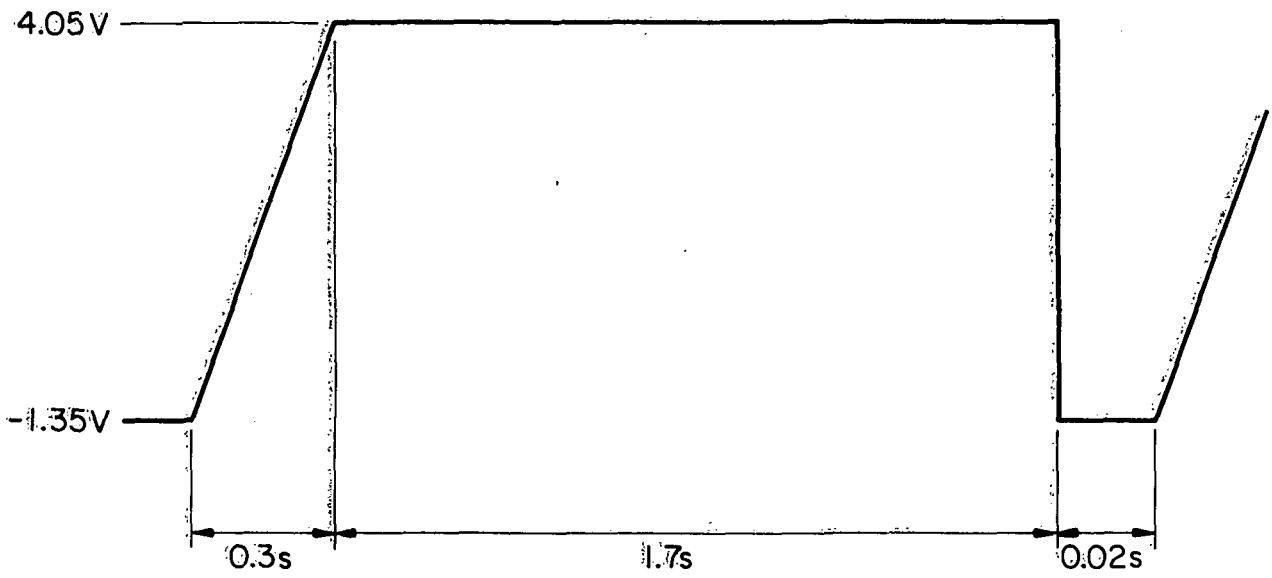

Figure 2.2. Probe voltage profile.

profile repeats every 2 seconds, providing alternating measurements of temperature and density. During the constant voltage mode, the probe current is processed by the logarithmic electrometer and AC amplifier. Both output signals are transmitted to a telemetry station and recorded on tape.

2.1.1 Langmuir probe theory. In the fine structure experiment, an electrode is inserted into the ionospheric plasma and held at a constant potential relative to the rocket body. The current into the electrode is then monitored as an indicator of electron concentrations. We now examine the relationship between the electron density, probe voltage and probe current.

Assuming the electrons in the ionosphere are in thermal equilibrium, the energy distribution may be represented by the electron temperature T_e. The average velocity of the electrons is then given by

$$\bar{v}_e = (8kT_e/\pi m_e)^{1/2}, \tag{2.1}$$

where k is the Boltzmann constant and m_e the electron mass. The current density j_o due to the random thermal motion of electrons is

$$j_o = N_e e\bar{v}_e/4, \tag{2.2}$$

where N_e is electron density and e the charge of the electron. For an ideal probe at the plasma potential, the current into the probe is

strictly dependent on the random motion of the electrons and is

$$I_o = j_o A, \tag{2.3}$$

where A is the surface area of the probe. For a probe at a positive potential V relative to the plasma potential, the current density j is given by

$$j = j_o(1 + eV/kT_e). \tag{2.4}$$

The current into the probe is

$$I = jA = \frac{AN_e e\bar{v}_e}{4}(1 + eV/kT_e). \tag{2.5}$$

This relation expresses the probe current as a function of the probe voltage V, the electron temperature T_e, and the electron density N_e.

Up to this point, currents due to negative and positive ions have been neglected. This neglect is quite valid for negative ion currents since the concentration of negative ions is negligible at altitudes above 90 km, i.e., in the E region. The positive ion current cannot be so easily dismissed. At thermal equilibrium the mean velocity of the ions is

$$\bar{v}_i = (8kT_i/\pi m_i)^{1/2}. \tag{2.6}$$

From Equations 2.1 and 2.6 we have

$$\bar{v}_e/\bar{v}_i = (m_i T_e/m_e T_i)^{1/2} \ . \qquad (2.7)$$

In the D and E regions, collision frequencies are sufficiently large to maintain reasonable thermal contact between electrons and ions so that thermal equilibrium between these may be safely assumed. Equation 2.7 is then further simplified to give

$$\bar{v}_e/\bar{v}_i = (m_i/m_e)^{1/2} \ . \qquad (2.8)$$

This ratio is roughly 170; the exact value depends on the ion composition of the specific region of interest. This fact, along with charge neutrality ($N_e = N_i$), implies that the random electron current density is approximately two orders of magnitude larger than the random positive ion current density for a probe at the plasma potential. This ratio is increased further for a probe with a positive (ion-retarding) potential, as is the case for the fine structure experiment. Likewise, the ratio is also increased if the condition that thermal equilibrium exist between electrons and ions is relaxed, since theory and observation have shown that T_e is always greater than or equal to T_i. Therefore it is reasonable to assume that the current due to positive ions is negligible in comparison with the electron current. With this in mind, Equation 2.5 will be used to express the total current into the probe.

2.1.2 Signal development and on-board processing. As mentioned earlier, the probe current as a function of voltage and temperature is given by

$$I = \frac{AN_e e\bar{v}_e}{4}(1 + eV/kT_e). \tag{2.9}$$

In the fine structure experiment, the voltage V is held constant at 4.05 V. Assuming that the electron temperature remains constant over short intervals, a linear relationship exists between the current and electron density. The assumption of constant temperature over short intervals of altitude is generally accepted and is supported by most existing data. However, HIRAO AND OYAMA [1972] have questioned this assumption. Their data seems to indicate small scale temperature fluctuations in the 100 km to 200 km range, contradicting the constant temperature assumption. DURKIN AND SMITH [1981] have designed an experiment for high resolution measurements of the electron temperature profile in order to further investigate this. The experiment was flown on two Nike-Orion rockets in 1981 and 1982 at Wallops Island, Virginia; however the temperature data are not yet available at this time. For the present, we will take the former view that electron temperatures remain constant over the observation intervals resulting in a linear relationship between probe current and electron density.

The current into the probe is then given by

$$I = PN_e, \tag{2.10}$$

where $P = \frac{A\bar{e}v_e}{4}(1 + eV/kT_e)$. Fluctuations in electron density produce changes in probe current which are monitored by the logarithmic electrometer. The probe current may be decomposed into two components:

(a) a dc (or slowly varying) component, I_{av}, associated with the average value of the ambient electron density, and

(b) an ac component, ΔI, associated with the small-scale fluctuations about the ambient density.

This signal serves as the input to a logarithmic electrometer which is a current sensitive amplifier with a logarithmic gain characteristic. A logarithmic amplifier was chosen due to the large variation of I_{av} over the duration of the flights. The output voltage of the logarithmic electrometer is then given by the expression

$$V_1 = K \ln(I/I_s) = K \ln[(I_{av} + \Delta I)/I_s]$$

$$= K \ln(I_{av}/I_s) + K \ln(1 + \Delta I/I_{av}), \qquad (2.11)$$

where I_s is the reverse saturation current of the nonlinear feedback element. Assuming that ΔI is much smaller in magnitude than I_{av}, which experiment has shown to be the case, the electrometer output may be expressed as

$$V_1 = K \ln(I_{av}/I_s) + K(\Delta I/I_{av}); \quad \text{for } \Delta I \ll I_{av}. \qquad (2.12)$$

This signal is telemetered to ground via a channel of appropriate bandwidth and stored on magnetic tape to provide the large scale structure of the electron density profile.

At this stage, the magnitude of the ac signal is quite small in comparison with the dc bias. Since this small signal is the quantity of interest, the bias must be removed and the magnitude increased in order to increase the signal-to-noise ratio at the input to the telemetry transmitter. Therefore, the signal is enhanced by an ac amplifier. The output of the ac amplifier is given by

$$V_2 = GK\,(\Delta I/I_{av}) = GK\,(\Delta N_e/N_e), \qquad (2.13)$$

where G is the voltage gain of the amplifier. This signal is representative of the relative small scale structure of the electron density profile and is telemetered to ground for storage on magnetic tape.

2.2 Circuit Implementation for the Energy Budget Campaign

The instrumentation of the fine structure experiment is shown in Figure 2.3. Following is a description of the actual circuit implementation including details of integration into the payload.

2.2.1 Langmuir probe. The probes consist of spherical aluminum electrodes, 1 cm in diameter, coated with a layer of colloidal graphite (Aquadag). The coating provides a reasonable uniformity in the contact

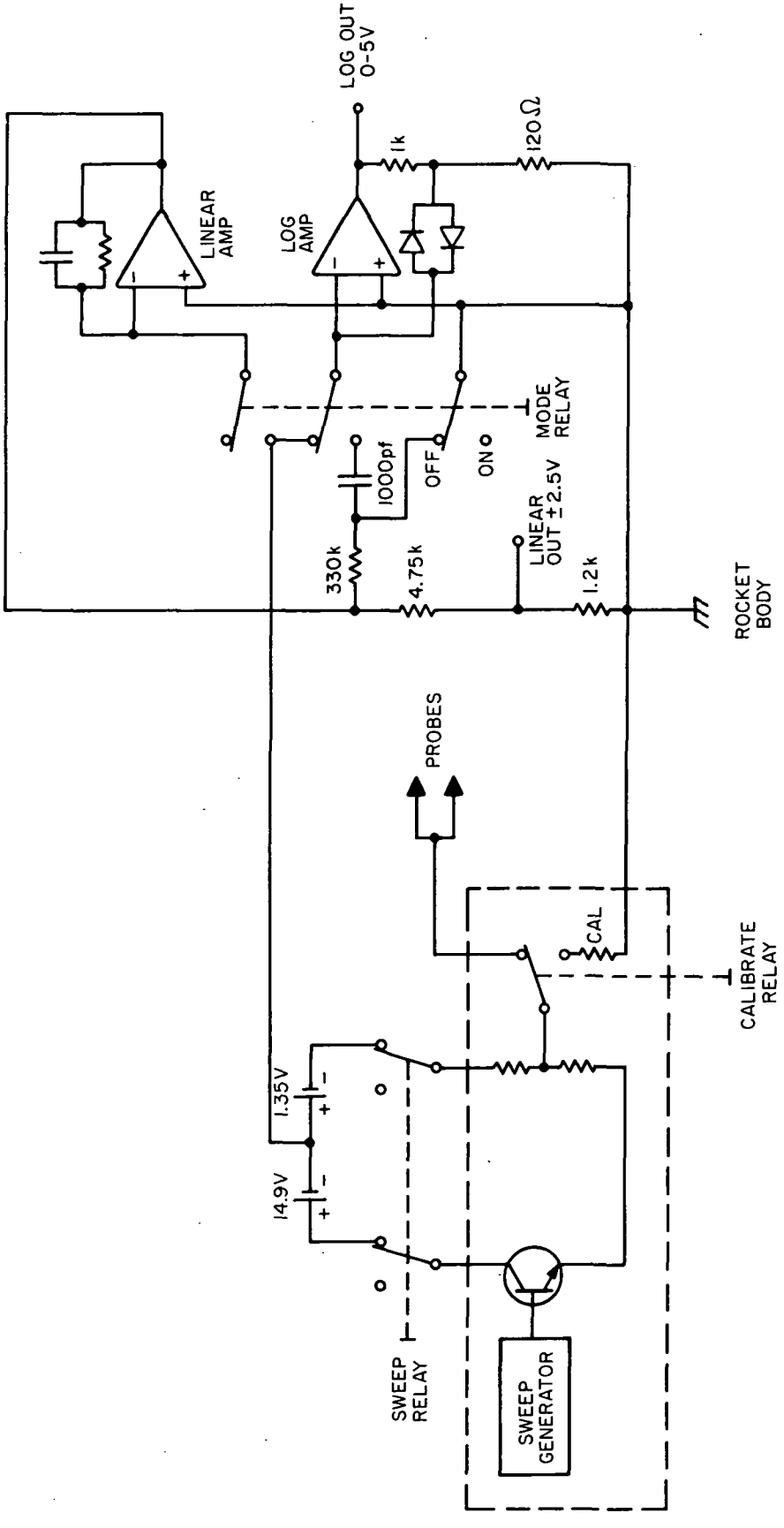

Figure 2.3. Instrumentation of the probe experiment as used in the Energy Budget Campaign.

potential of the probe surface. This is especially important in the calculation of plasma potential which is defined as the transition point in the i-v characteristic from a logarithmic dependence on voltage to a linear dependence (see Figure 2.4). If the contact potential is not uniform over the probe surface, small voltage offsets corresponding to small regions of constant contact potential occur in the equations relating probe current to voltage. Summing the contributions of each small area with a specific contact potential results in a distorted i-v characteristic in which the transition is less well defined. The colloidal graphite tends to reduce this effect while providing a smooth conducting surface.

A spherical geometry was selected for its indifference to orientation with respect to the magnetic field. SMITH [1969] has shown that the magnitude of the current for a given density is not dependent on the total surface area of the probe, but instead on the cross sectional area perpendicular to the magnetic field. Since a sphere presents the same cross section from any aspect, it is insensitive to orientation with respect to the magnetic field.

Physical dimension is another important consideration in the use of probes for rocket-based measurements. A positive voltage relative to the plasma potential placed on the probe tends to force the rocket floating potential negative which in turn decreases the probe potential. This occurs so that enough positive ion current may flow into the rocket body to equal the electron current drawn by the probe.

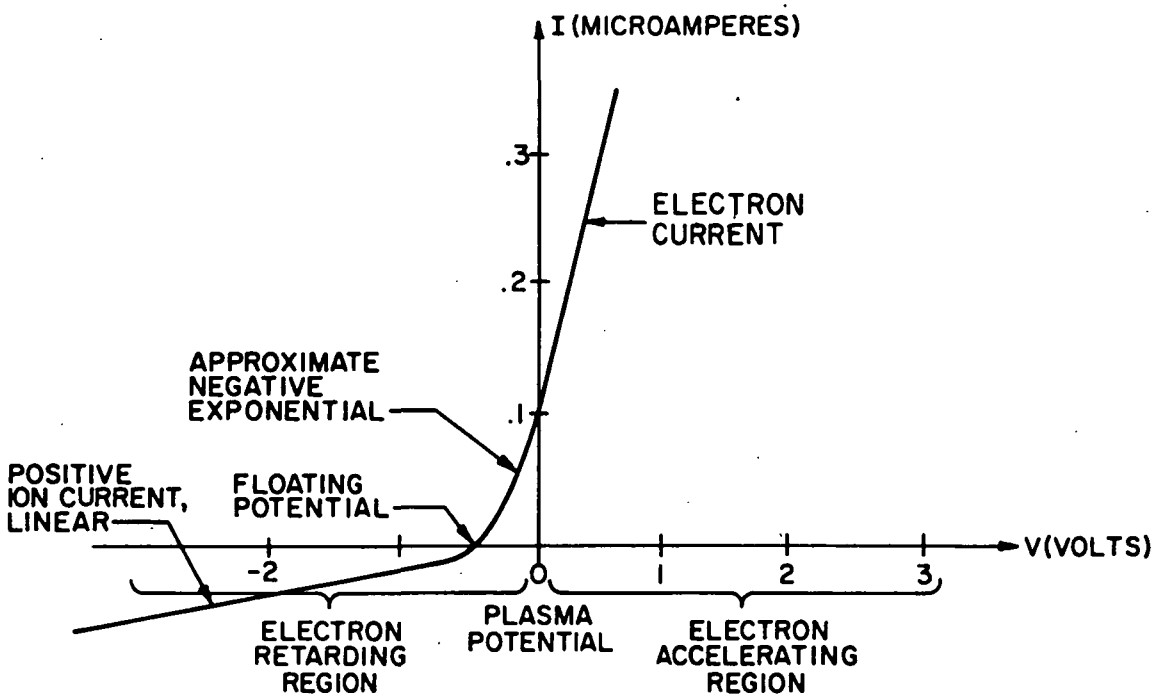

Figure 2.4. Total electrode current, including electron and positive-ion components (ZIMMERMAN AND SMITH, 1980).

The dependence on probe and rocket surface areas is shown below to be a consequence of these equal currents:

$$I_e = I_i; \tag{2.14}$$

$$j_e A_{probe} = j_i A_{rocket}; \tag{2.15}$$

$$\frac{(1 + eV_{probe}/kT_e)}{(1 - eV_{rocket}/kT_i)} = j_{oi} A_{rocket} / j_o A_{probe}. \tag{2.16}$$

If the quantity on the right is equal to one ($A_{rocket} \cong 170\ A_{probe}$) and assuming $T_e \cong T_i$, then V_{probe} is equal to $-V_{rocket}$; the voltages are symmetric about the plasma potential. Clearly, it is desirable to minimize the voltage shift and maintain V_{rocket} as near as possible to the plasma potential. This is accomplished by ensuring that the ratio on the right is as large as possible. A reasonable lower bound is ten, which for a probe voltage of 4.05 V allows a 7.4% offset. The following relation must then be satisfied:

$$A_{rocket} \geq 1700\ A_{probe}. \tag{2.17}$$

The Taurus Orion rocket and the payload are shown in Figures 2.5 and 2.6, along with the relevant dimensions. The surface area of the Orion and payload combination is approximately 5.2×10^4 cm^2 while the

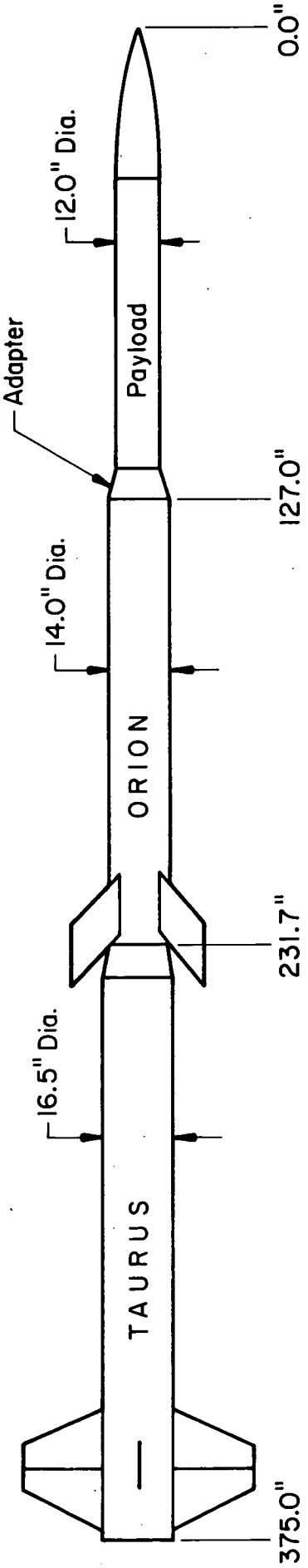

Figure 2.5. Rocket configuration for the Energy Budget Campaign.

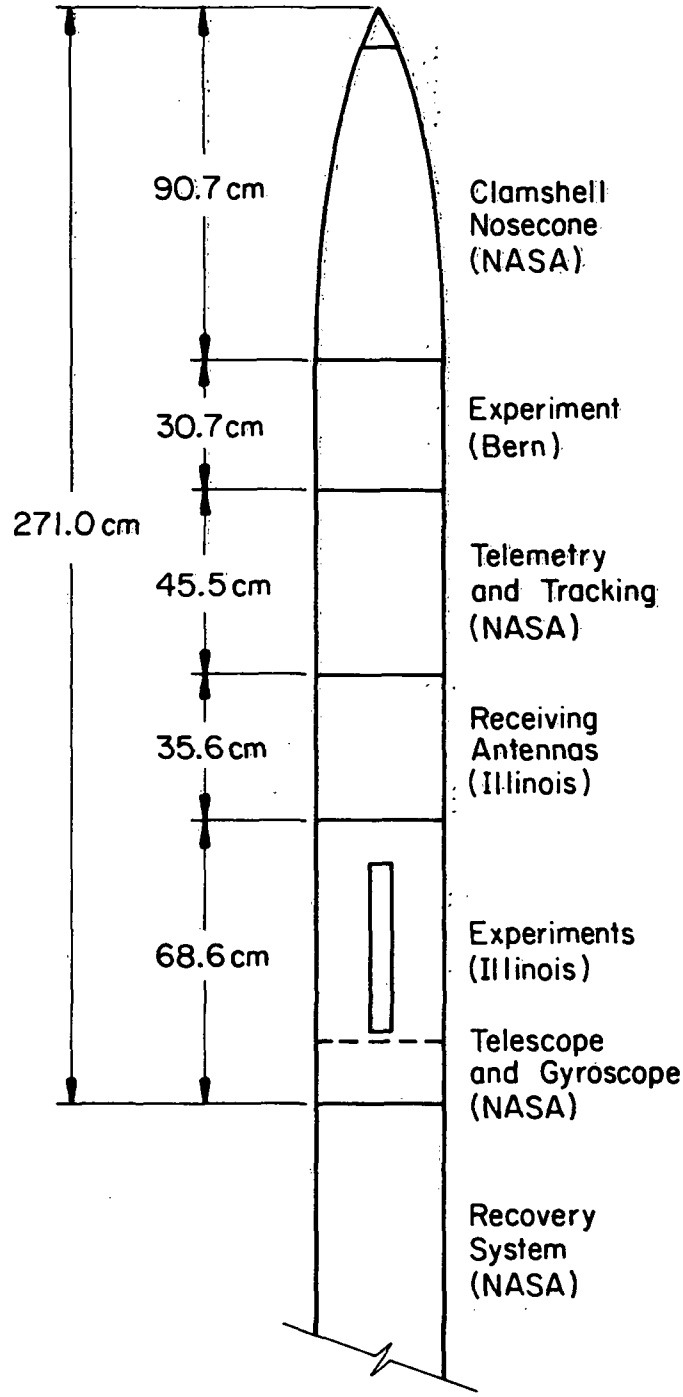

Figure 2.6. Payload configuration for the Energy Budget Campaign.

probe area (total) is 6.3 cm^2 yielding a ratio of 8197/170 ≃ 48. This is more than sufficient to keep the voltage shift of the rocket within acceptable limits.

In the above calculations, the total surface area of the Orion stage is used rather than the cross sectional area perpendicular to the magnetic field. This is reasonable since the positive ion current is not dependent on the magnetic aspect angle [ZIMMERMAN AND SMITH, 1980].

The last consideration concerning the probe is integration into the payload. In the launches of the Energy Budget Campaign, the Langmuir probes were mounted on booms with a 180° separation about the rocket axis. The booms are 76.2 cm in length and are located 243.8 cm from the nose tip. In past flights, these dimensions have proved adequate to minimize the effect of the vehicle wake on density measurements. The probes are positioned opposing each other and electrically connected in parallel in order to reduce the effect of non-uniformities of electron density in the region around the rocket. A non-uniform density distribution manifests itself as a modulation in the probe current. For a single boom mounted probe, the modulation has a frequency equal to the spin rate of the rocket and a magnitude proportional to the maximum differential in the density (Figure 2.7). The modulation frequency for the parallel pair on the other hand is twice the spin rate with a magnitude proportional to one-half the maximum density differential. Therefore, the parallel probe configuration smooths out the non-uniformities.

2.2.2 Sweep and timing circuits. The sweep circuit provides the

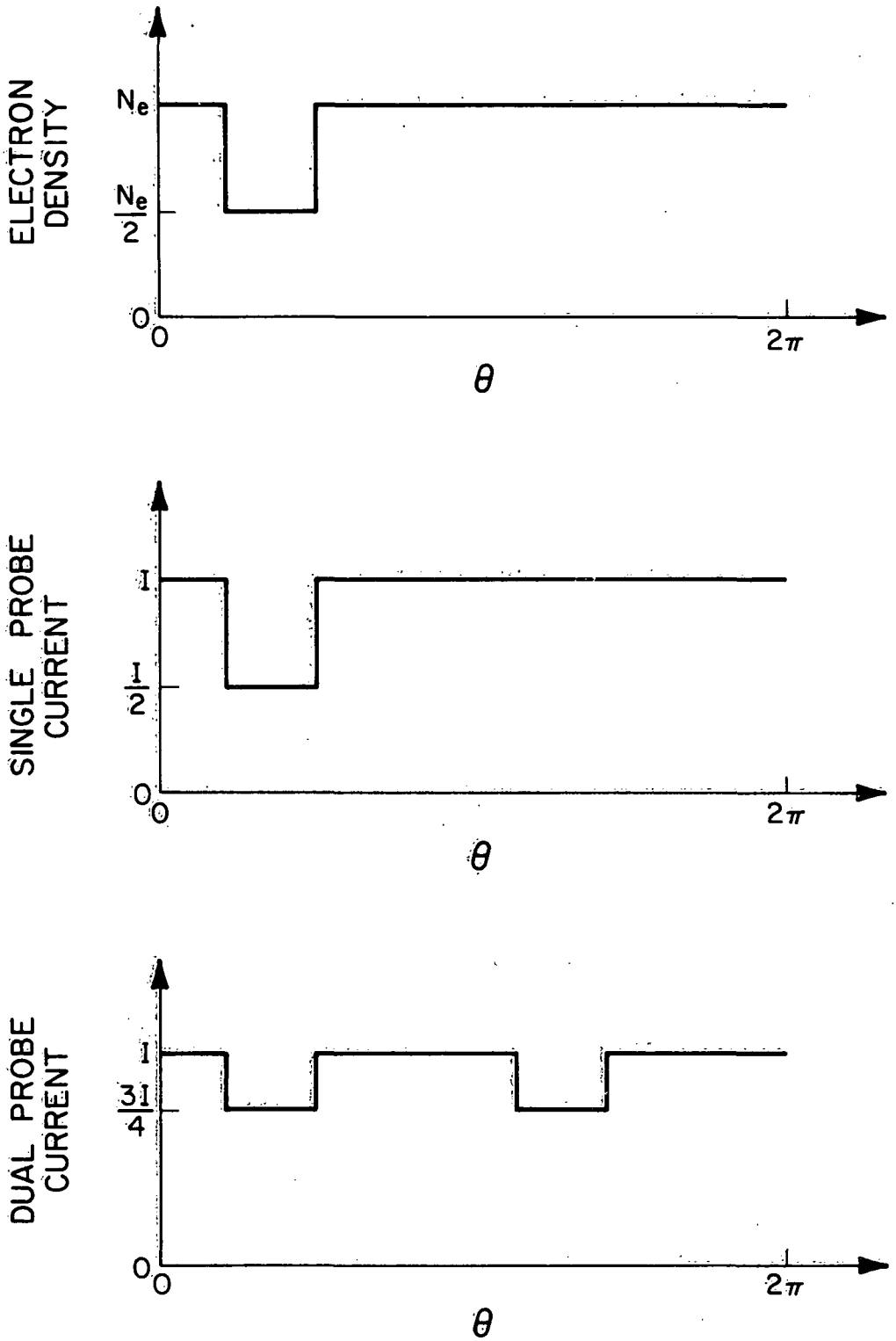

Figure 2.7. Effect of probe position on spin frequency corruption.

periodic voltage profile mentioned in Section 2.1. The circuit and pinouts are shown in Figure 2.8. Upon activation of the sweep relay K1, a linearly increasing voltage appears across C1 at a rate dictated by the time constant τ(= (R1 + R3) C1). Eventually the rising voltage on C1 turns Q1 off and the voltage remains constant until sweep relay K1 is turned off, at which time C1 discharges through R4. The cycle is repeated upon reactivation of the sweep relay. The voltage on C1 is buffered by a voltage follower Q2, and divided to obtain the required range of -1.35 to 4.05 V.

A calibration feature is also included in the sweep circuit. To perform in-flight calibrations of the probe circuitry, relay K2 may be activated, thus connecting the probe input to a grounded resistor. This provides a known current to the circuit, allowing in-flight monitoring of circuit operation.

The probe timer operates the sweep and mode relays, shown in Figures 2.3 and 2.8, and is responsible for the timing scheme of the experiment. The circuit implementation and timing diagram are given in Figures 2.9 and 2.10. When power is connected to the timer circuit, Q2 turns on and the sweep relay is initially energized. At this time, a voltage develops across C1 at a rate dependent on the time constant τ_1(= R8xC1). This voltage increases until the threshold of the unijunction transistor is reached at which time C1 is quickly discharged and Q2 is turned off, de-energizing the sweep relay. The time constant τ_1 is adjusted by selecting R8 and in this case is set for 2 seconds. With Q2 off, a reverse voltage builds on C1 with a time constant τ_2(=R2xC1). This reverse voltage increases until Q2 turns on again, beginning the

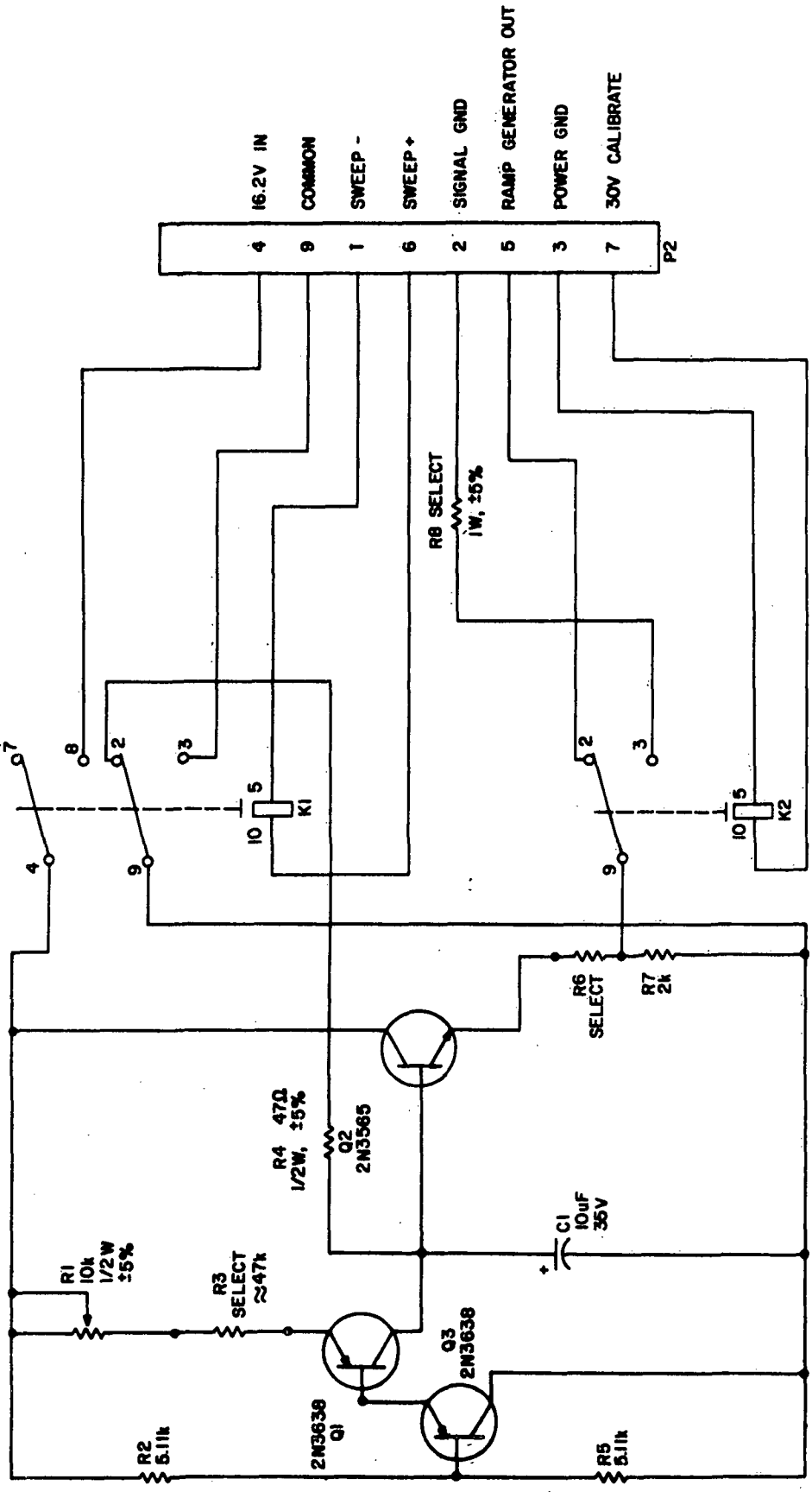

Figure 2.8. Schematic of the sweep circuit (ZIMMERMAN AND SMITH, 1980).

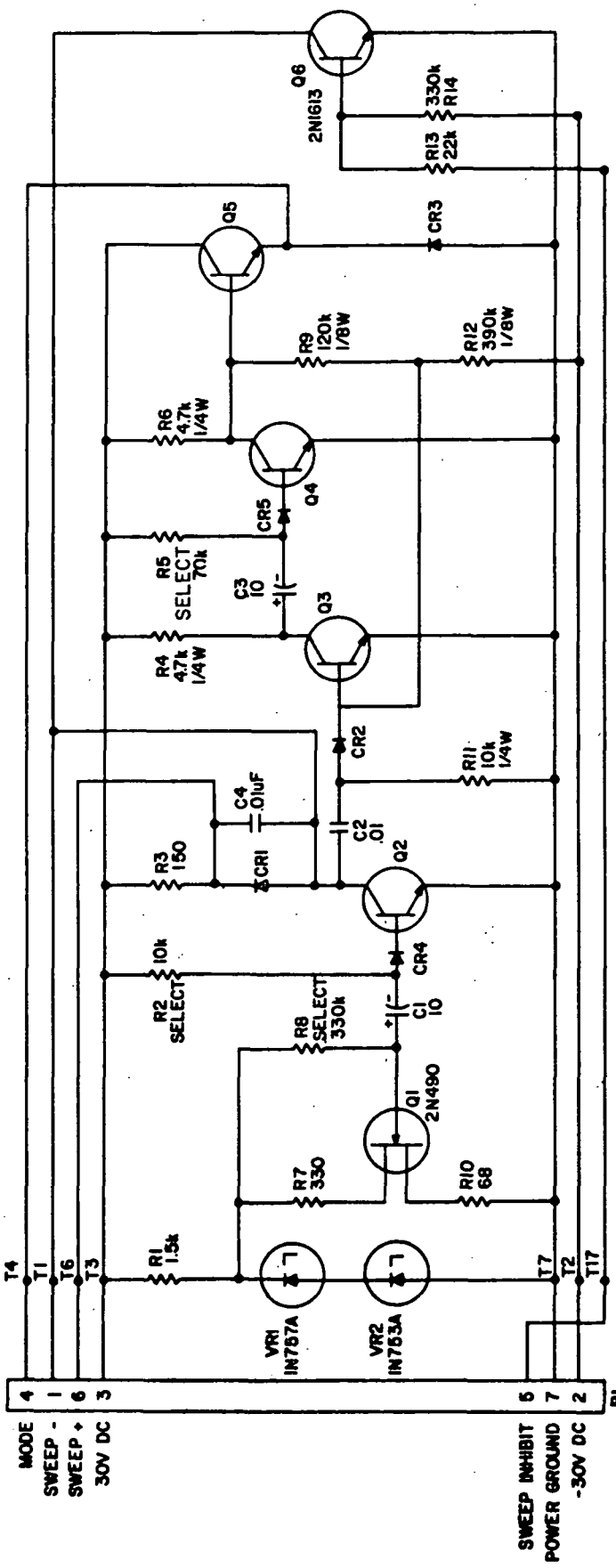

Figure 2.9. Schematic of the timing circuit (ZIMMERMAN AND SMITH, 1980).

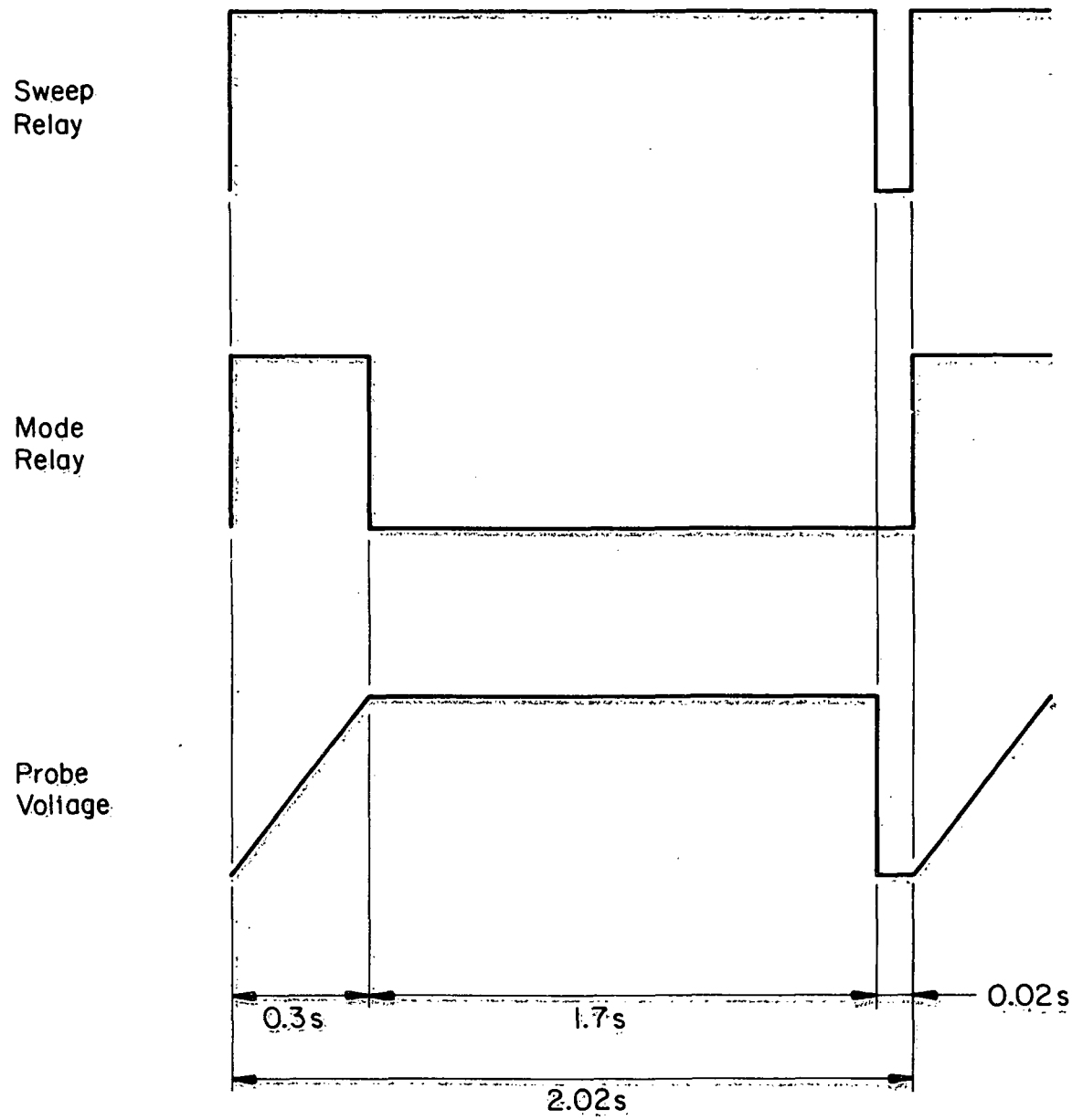

Figure 2.10. Timing diagram for the timing circuit.

next cycle. The time constant τ_2 is adjusted for 20 msec by proper selection of R2. This arrangement provides the sweep relay profile shown in the figure.

To provide synchronization between the sweep relay and mode relay, the output of Q2 serves as the input to an additional circuit (Q3, Q4, Q5). Initially, Q3 and Q5 are nonconducting while Q4 is conducting. As Q2 is turned on, Q3 conducts, Q4 shuts off and Q5 energizes the mode relay. Charge then builds on C3 at a rate specified by τ_3(= R5xC3) until Q4 conducts, cutting off Q5 and Q3. For this case, τ_3 is adjusted by R5 to be 0.3 seconds. This cycle repeats as Q2 is triggered.

2.2.3 Logarithmic electrometer. The circuit of the logarithmic electrometer is shown in Figure 2.11 [KLAUS AND SMITH, 1978] along with its ideal circuit representation. A Kiethly Instruments Inc. Model 302 was chosen for its low input impedance and the nominally low input bias current ($\approx 10^{-12}$A). The logarithmic characteristic was chosen to increase the dynamic range of the amplifier and is obtained by the diode configuration in the feedback. The current through the diode is given by

$$I_d = I_s[\exp(v_1/v_T) - 1] \tag{2.18}$$

where I_s is the reverse bias saturation current of the diode, v_1 is the voltage across the diode, and v_T (= kT/e) is approximately 25 mV. For values of v_1 greater than 90 mV (i.e., $\exp(v_1/v_T) \geq 10$), Equation 2.18 may be approximated by

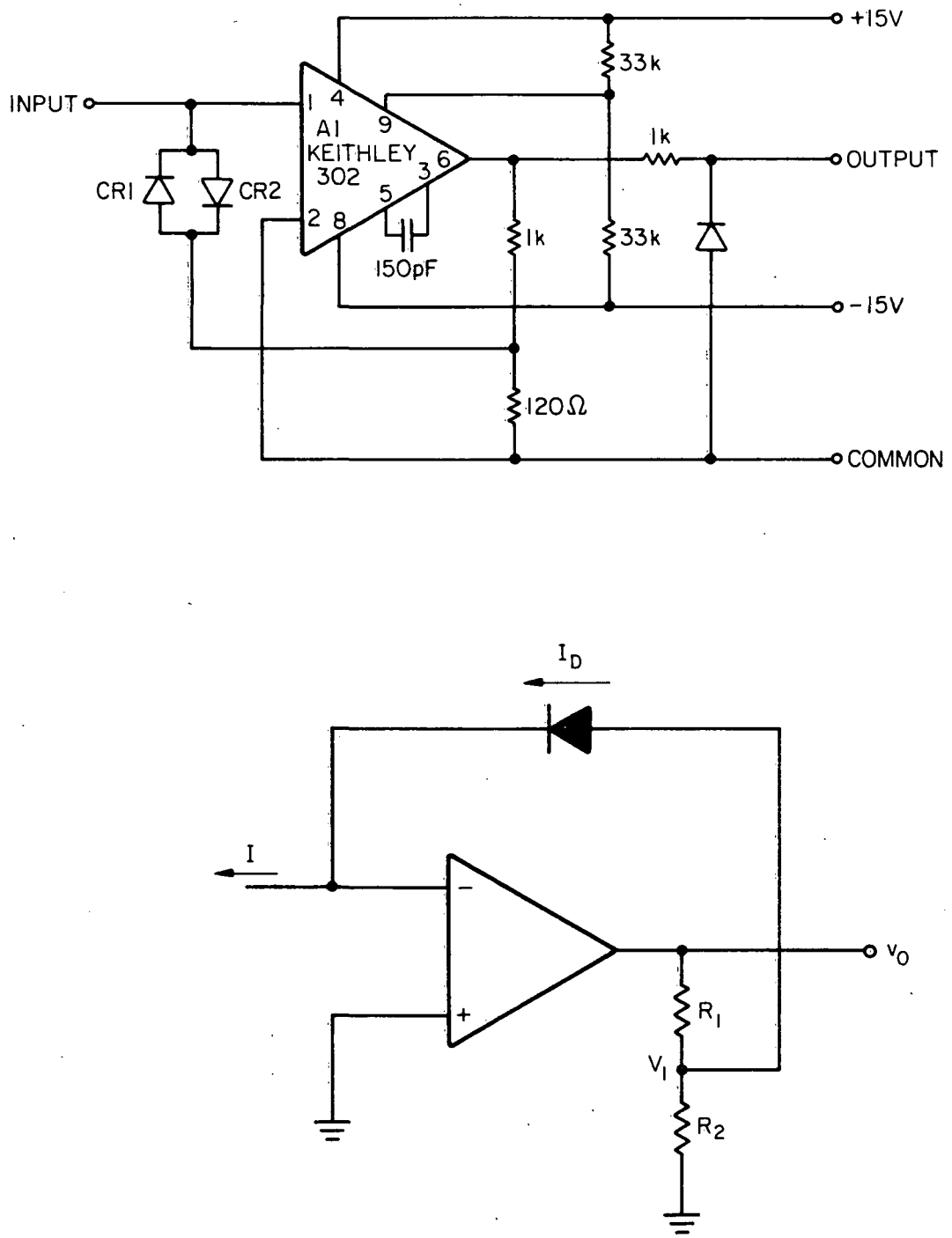

Figure 2.11. Schematic of logarithmic electrometer and a simplified representation.

$$I_d \simeq I_s[\exp(v_1/v_T)]. \tag{2.19}$$

The assumption that the measured current I is much larger than the input bias current yields

$$I \simeq I_d = I_s \exp(v_1/v_T). \tag{2.20}$$

The output of the electrometer is thus given by

$$v_o = \left(\frac{R_1 + R_2}{R_2} v_T\right)\ln(I/I_s); \qquad I > I_s. \tag{2.21}$$

The reverse bias leakage current I_s presents a lower bound on the measurable current assuming the input bias current is less than I_s. If this is not true, the measurable current is lower bounded by the bias current.

For auroral flights, electron currents in the range of 10^{-8} A to 10^{-4} A (corresponding to approximate electron densities of 10^2 to 10^6 electrons per cm^3) were expected in the D and E regions. With the low input bias current of the Model 302, electron currents as small as 10^{-10} A may be measured. The p-n junction in the feedback circuit is therefore chosen to have a logarithmic characteristic in the above-mentioned ranges and a leakage current much less than the bias

current. The gain factor K is then adjusted to provide a reasonable output to the telemetry transmitter. For the Energy Budget Campaign, a transistor junction is used in the feedback with an I_s on the order of 10^{-15} A. To provide an output in the 0-5 range, R_1 and R_2 are specified as 1 k Ω and 120 Ω respectively. This configuration yields a gain factor, K, for the fine structure signal of 0.247 V and a base-ten logarithmic voltage gain of 0.57 V/decade for the average current.

The frequency response of the logarithmic electrometer is characterized for two different situations. The first deals with the frequency response to small signal fluctuations about an average current; the second deals with large fluctuations in the average current itself. KLAUS AND SMITH [1978] measured the frequency response due to small scale signal fluctuations by imposing a square wave on an average current and measuring the rise time of the output. They found that the frequency response was proportional to the average current. For an average current of 10^{-8} A, the upper cutoff frequency was found to be 2.5 kHz. This response is important for the fine structure experiment.

ZIMMERMAN AND SMITH [1980] have included a theoretical computation of the frequency response due to large average current fluctuations based on measurements of the small signal response. The analysis considered a step input of current of magnitude I. The response was again found to be proportional to the magnitude of the current. For a current step of 10^{-8} A, the upper cutoff frequency is calculated to be 650 Hz. This is the upper cutoff frequency for large scale changes in the average electron density.

2.2.4 ac amplifier. The schematic of the ac amplifier is shown in Figure 2.12 [KLAUS AND SMITH, 1978]. The midband voltage gain of the amplifier, determined by the feedback resistor and the output voltage divider, was set at 100. This configuration was chosen to limit the output voltage range to ± 2.5 V (with a supply voltage of ± 10 V). This prevents overdriving the telemetry VCO and interfering with adjacent channels. The voltage gain of 100 allows observation of electron density irregularities up to 10%.

The frequency response of the ac amplifier was measured by the risetime-falltime method described by KLAUS AND SMITH [1978]. The upper cutoff frequency is specified by the time constant of the feedback network. The measured cutoff frequency was found to be approximately 2 kHz. The lower cutoff frequency is specified by the time constant of the input circuit. Due to a modulation of the input current at the spin frequency of the rocket (see Section 2.2.1) the lower cutoff frequency was adjusted to attenuate this low frequency signal ($\tilde{\sim}$ 12 Hz) and thereby prevent saturation of the ac amplifier. The measured cutoff was approximately 50 Hz providing 12 dB of rejection at 12 Hz.

2.2.5 Telemetry. The telemetry consists of an on-board FM/FM system with an S-band transmitter. Data from the individual experiments are assigned to specific channels corresponding to the standard IRIG format. The FM subcarriers are then used to frequency modulate the S-band carrier. The data are retrieved on the ground and the multiplexed subcarriers are obtained by discrimination of the S-band carrier. The subcarriers are then stored on tape in an analog format.

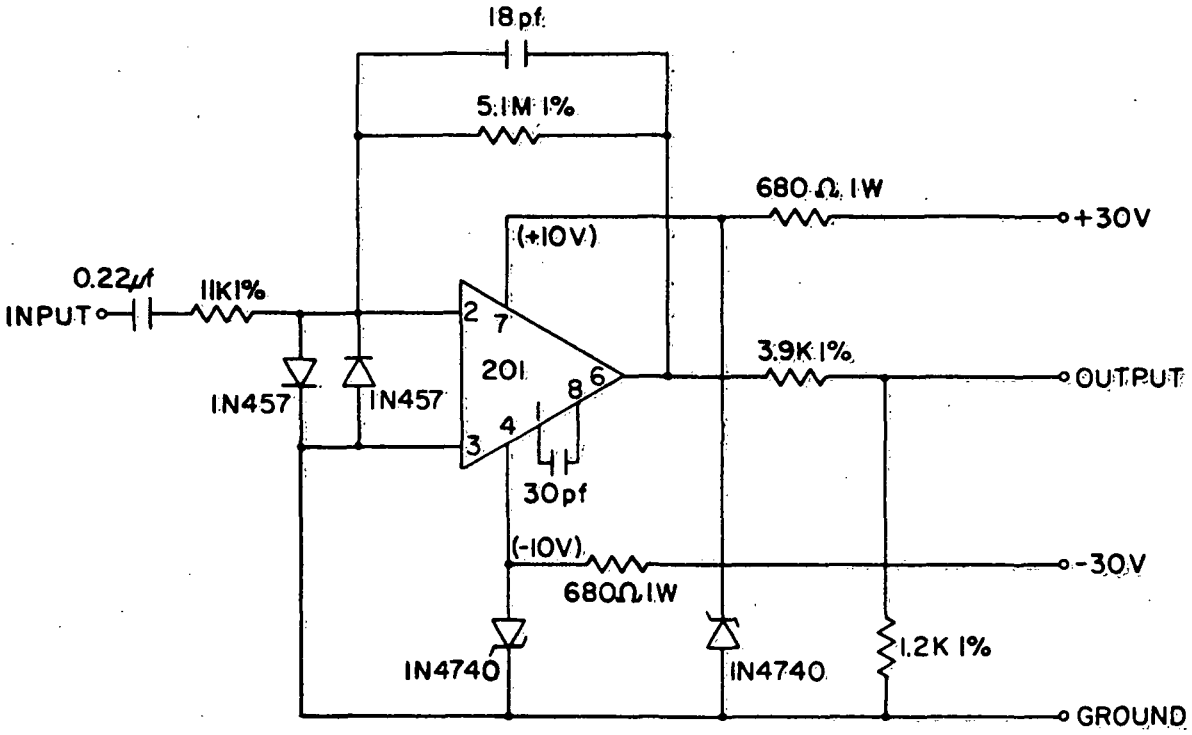

Figure 2.12. Schematic of the ac amplifier for the Energy Budget Campaign (KLAUS AND SMITH, 1978).

The fine structure data (output of ac amplifier) were assigned to IRIG channel 18 with a bandwidth of 1050 Hz. The logarithmic electrometer output was carried on channel 20 with a bandwidth of 1860 Hz. Table 2.1 lists the channel assignments for the other experiments of the Energy Budget Campaign.

2.3 System Calibration and Special Issues

2.3.1 Probe electrometer calibrations. The probe electrometer was tested to insure a logarithmic characteristic. To check the characteristic, the probes were placed in the constant voltage mode (4.05 V) and connected to ground through a variable resistance. This allowed manipulation of the current into the probe and monitoring of the log electrometer output voltage. The test results for the three payloads are shown in Table 2.2. As can be seen, the logarithmic characteristic is quite accurate.

2.3.2 Effects of voltage divider on electrometer output. In order to adjust the gain of the logarithmic electrometer, a voltage divider was introduced into the feedback (refer to Figure 2.11). The original analysis assumed that this voltage source was ideal; the question is the validity of this assumption. An idealized circuit equivalent is shown in Figure 2.13. The object is to calculate the Thevenin equivalent circuit for the portion on the left of the dashed line and to determine the effect of the voltage divider on the output characteristic. The details of the analysis are shown in the figure. It is evident that a linear term arises in the output characteristic which may adversely

Table 2.1 Telemetry channel assignments for the Energy Budget Campaign.

CH.	I	
	20	Boom probe, (logarithmic output)
	19	Microprocessor (EPS experiments)
	18	Boom probe, fine structure
	17	EPS 1
	16	EPS 2
	15	Receiver #1, modulation
	14	Receiver #2, modulation
	13	EPS 3
	12	EPS 4
	11	AGC #1
	10	AGC #2
	9	Magnetometer (transverse)
	8	Commutator
	7	Roll gyro
	6	Pitch gyro
	5	Yaw gyro

Table 2.2 Logarithmic electrometer calibrations for the Energy Budget Campaign

Input Current (A)	Output Voltage (V)	Voltage Gain (V/decade)
Flight 33.009		
4.05×10^{-10}	2.52	
		0.54
4.05×10^{-9}	3.06	
		0.56
4.05×10^{-8}	3.62	
		0.55
4.05×10^{-7}	4.17	
		0.61
4.05×10^{-6}	4.78	
		0.61
4.05×10^{-5}	5.39	
Flight 33.010		
4.05×10^{-10}	2.70	
		0.57
4.05×10^{-9}	3.27	
		0.55
4.05×10^{-8}	3.82	
		0.55
4.05×10^{-7}	4.37	
		0.55
4.05×10^{-6}	4.92	
1.50×10^{-5}	5.23	
Flight 33.011		
4.05×10^{-10}	2.49	
		0.62
4.05×10^{-9}	3.11	
		0.58
4.05×10^{-8}	3.69	
		0.56
4.05×10^{-7}	4.25	
		0.57
4.05×10^{-6}	4.82	
		0.62
4.05×10^{-5}	5.44	

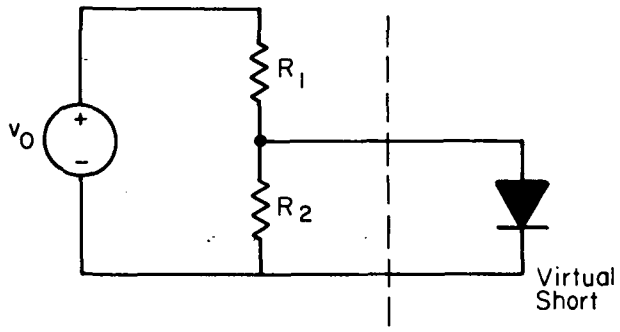

a)

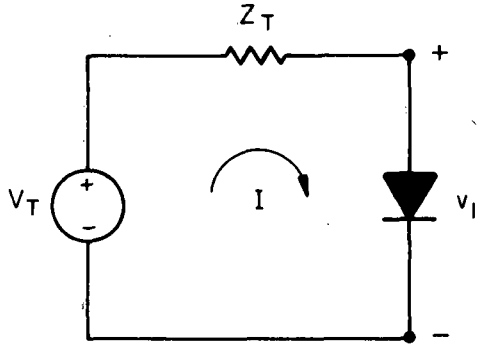

$$I = I_S \exp(v_i / mv_t) = I_S \exp\left[(V_T - IZ_T)/mv_t\right]$$

$$V_T = mv_T \ln(I/I_S) + IZ_T$$

$$v_o = \left(\frac{R_1 + R_2}{R_2}\, mv_T\right) \ln(I/I_S) + IR_1$$

b)

Figure 2.13. Effect of voltage divider on the logarithmic electrometer output.

affect the output, depending on the value of R_1. This fact should be taken into account in the data analysis.

2.3.3 Vehicle potential sensitivity. Another point of interest is the effect of vehicle potential variation on the experiment. Experience has shown that small variations in vehicle potential do occur during the rocket flight, thereby changing the ground reference of the experiments. The effects may be studied by observing the output of the logarithmic electrometer as expressed in equation 2.12,

$$V_1 = K \ln(I_{av}/I_s) + K(\Delta I/I_{av}). \tag{2.22}$$

Recalling that $I = PN_e$ where $P = \frac{Ae\bar{v}_e}{4}(1 + eV/kT_e)$,

$$V_1 = K \ln(PN_e/I_s) + K(\Delta N_e/N_e). \tag{2.23}$$

Changing vehicle potential is reflected in a change in P. It is obvious that the relative irregularity term is independent of P and therefore of small variations in vehicle potential. The background density term however is affected and must be dealt with in the analysis.

2.3.4 Calibration of background electron density. In the description of the fine structure experiment, various references have been made to the measurement of the background (ambient) electron density. This is the result of their interdependence in the measurement

technique. Therefore, in the interest of completeness, a few words will be mentioned concerning the calibration of the background density.

It was noted earlier that the major assumption concerning probe measurements of electron density was that of constant electron temperature over short intervals. This corresponds to a constant P in Equation 2.23. Since P does vary over larger intervals, a calibration factor is needed to obtain absolute measurements of electron density. A method of performing this calibration is based on the techniques of Faraday rotation and of differential absorption which have been described by FRANCE AND WILLIAMS [1976] and JACOBSEN AND FRIEDRICH [1979]. In this experiment, a CW linearly polarized radio wave is transmitted from the ground to a rocket-borne receiver with a dipole antenna. As the radio wave propagates through the ionosphere, the plane of polarization rotates as a function of electron density. This rotation is due to the different refractive indices of the two characteristic modes. Along with the rotation, a modification of the wave occurs as a result of the difference in absorption coefficients of the characteristic modes. This signal is then received on-board the rocket where the rotation and differential absorption may be monitored.

Both the differential absorption and Faraday rotation yield quite accurate absolute values of electron density; however, the resolution is on the order of 1 km. Therefore, to obtain high resolution absolute measurements of electron density, the experiment is used to calculate the proportionality constant P of the probe experiment.

2.3.5 Harmonic distortion due to logarithmic compression. The probe experiment uses logarithmic compression in the measurement of current. This distorts the spectrum of the fluctuations in probe current. The following analysis shows that the distortion is negligible in the case of our measurements of ionospheric irregularities.

The compression can be expressed mathematically by

$$y = \ln(1 + x), \tag{2.24}$$

where y represents the output of the system and x the ac component of the signal. Consider a sinusoidal signal $x = a \cos \omega t$. This is a fluctuation at frequency ω with peak amplitude a; the amplitude is expressed as a fraction of the dc (or steady) signal. The logarithmic compression will introduce harmonics at frequencies 2ω, 3ω ... This effect, taken over a range of fundamental frequencies, will distort the spectrum by increasing the relative importance of the higher frequencies.

For $x \ll 1$, series expansion gives

$$y = \ln(1 + x) = x - x^2/2 + x^3/3 - x^4/4 + \ldots \tag{2.25}$$

so that, using $x = a \cos \omega t$,

$$y = a\cos\omega t - (a^2/2)\cos^2\omega t + (a^3/3)\cos^3\omega t \qquad (2.26)$$

$$- (a^4/4)\cos^4\omega t + \ldots$$

Next, powers of cos ωt are expressed in terms of the harmonics using

$$\cos^2\omega t = 1/2 + (1/2)\cos 2\omega t,$$

$$\cos^3\omega t = (3/4)\cos\omega t + (1/4)\cos 3\omega t, \qquad (2.27)$$

$$\cos^4\omega t = 3/8 + (1/2)\cos 2\omega t + (1/8)\cos 4\omega t.$$

Substituting and collecting terms give

$$y = -[(1/4)a^2+(3/32)a^4+\ldots] + [a+(1/4)a^3+\ldots]\cos\omega t$$
$$-[(1/4)a^2+(1/8)a^4+\ldots]\cos 2\omega t + [(1/12)a^3+\ldots]\cos 3\omega t$$
$$-[(1/32)a^4 + \ldots]\cos 4\omega t. \qquad (2.28)$$

The ratio of the amplitude of the second harmonic to the amplitude of the fundamental is

$$A_2/A_1 = [(1/4)a^2+(1/8)a^4+\ldots]/[a+(1/4)a^3+\ldots]. \qquad (2.29)$$

If $a^2 \ll 1$, as is to be expected, then

$$A_2/A_1 \approx a/4. \qquad (2.30)$$

Similarly, the ratio of the amplitude of the third harmonic to the amplitude of the fundamental is

$$A_3/A_1 = (1/12)a^3/[a + (1/4)a^3 + \ldots] \approx a^2/12. \qquad (2.31)$$

These ratios lead to the conclusion that the spectral distortion becomes less serious as the amplitude becomes smaller. For the large amplitude fluctuations given by $\Delta N/N = 5\%$ (peak-to-peak) we have $a = 2.5 \times 10^{-2}$. Thus $A_2/A_1 \approx 6 \times 10^{-3}$ and $A_3/A_1 \approx 5 \times 10^{-5}$.

The distortion will also be more significant as the power law index becomes a large negative number. Taking the steepest spectral slope encountered in these observations (-7, in power) the ratio of $\Delta N/N$ at frequencies one octave apart would be $2^{-7/2} = 9 \times 10^{-2}$. Since this value is much greater than the value of A_2/A_1 calculated above for the large amplitude fluctuation we conclude that spectral distortion is negligible in these observations.

2.4 Modifications for Project Condor: the Equatorial Experiment

The fine structure experiment was modified for the equatorial flights 31.028 and 31.029 of Project Condor in order 1) to increase the experiment sensitivity at higher frequencies, and 2) to provide post-flight computation of the spectral index as a "quick look" feature as well as a check on the computer processing to follow.

The modified experiment includes the same sweep generator and logarithmic electrometer as that for the Energy Budget Campaign. The major modifications were implemented in the signal processing hardware after the electrometer.

The block diagram of the modified fine structure experiment as flown for Project Condor is illustrated in Figure 2.14. It is composed of the sweep generator and logarithmic electrometer used for the Energy Budget Campaign with an ogive-shaped nose-tip probe instead of the dual probe arrangement. The next portion consists of a pair of broadband amplifiers whose outputs will provide the data for the computer spectral analysis. Last, a pair of narrowband filter/amplifier combinations provide real-time samples of the irregularity spectrum.

The probe used for Project Condor is a nose-tip probe having the shape generated by spinning an ogive about its axis of symmetry. This shape was chosen to provide a constant surface area projection onto any plane about the probe thereby preserving the current-to-voltage characteristic of the probe. The sweep and timing circuits are described in detail in Section 2.2.2. Likewise, the logarithmic electrometer design and operation are outlined in Section 2.2.3 with one minor modification outlined in Section 2.5.2. The overall gain of the electrometer was adjusted and measured at 0.82 V/decade for the average current which for the fine structure equipment corresponds to a gain factor K of 0.356 V. The electrometer exhibited a flat small signal frequency response with a 3 dB upper cutoff frequency of 1.8 kHz at an average input current of 10^{-8} A. For average input currents above

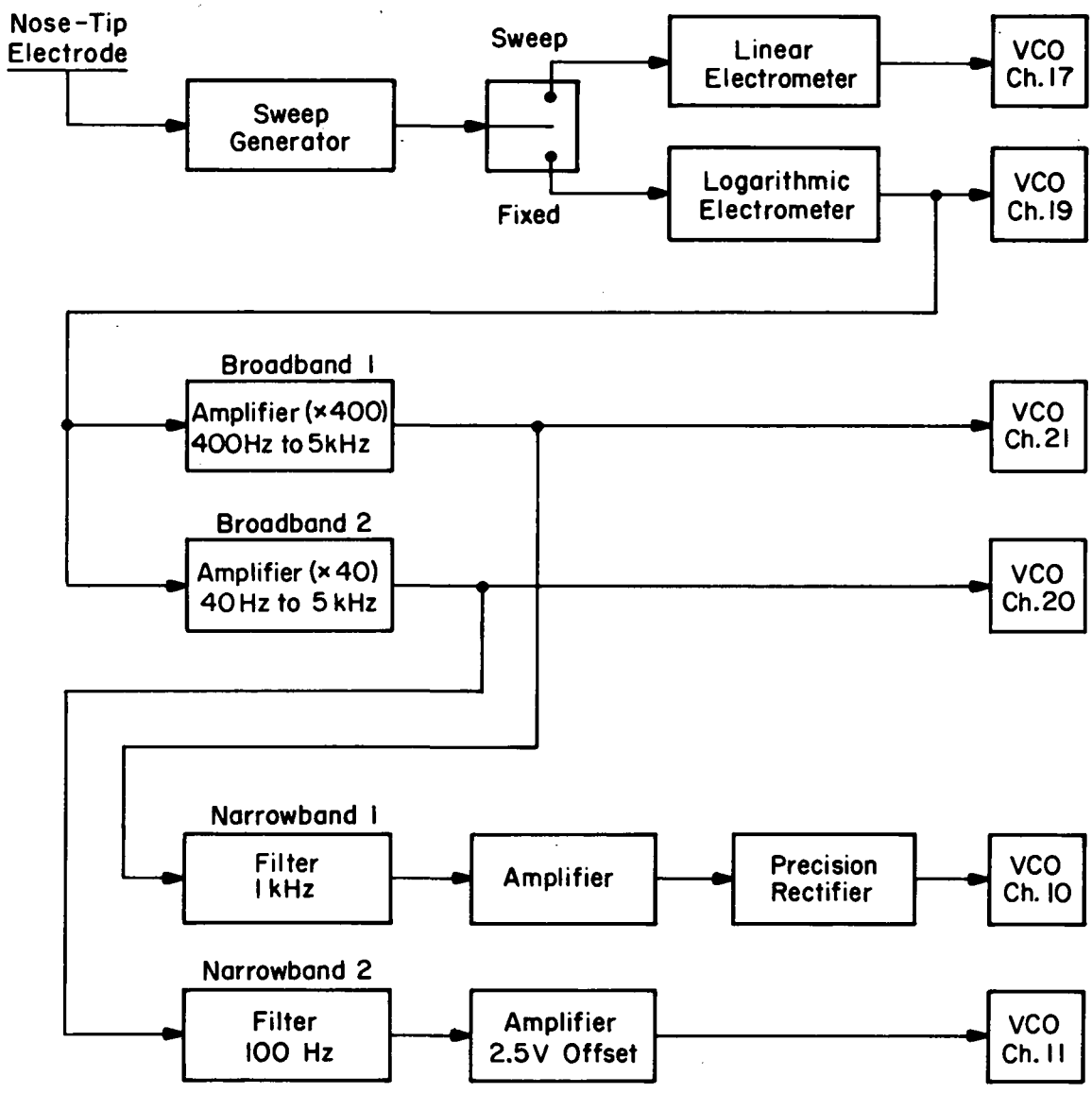

Figure 2.14. Block diagram of the modified electron density probe and fine structure experiment for Project Condor.

10^{-7} A the upper cutoff frequency was in excess of 7 kHz. The detailed calibrations of the electrometers used for Project Condor are included in the next section. The output of the electrometer serves as the input to the broadband amplifiers and is also assigned to telemetry channel 19 with a bandwidth of 7 kHz (for a modulation index of one).

At the output of the electrometer, the magnitude of the fine structure signal is quite small in comparison with the dc signal due to the average electron density. Since this small signal is the quantity of interest, the bias must be removed and the magnitude increased so as to provide the telemetry transmitter with a reasonable signal level. This is accomplished by two broadband ac amplifiers with differing gains and frequency bands of operation. The need for two separate amplifiers is a consequence of the signal contamination arising from the rocket spin. Asymmetries in electron density introduced by wake effects contribute to modulation of the probe current at the spin frequency of the rocket ($\approx$ 6 Hz) and at harmonics of this frequency. This contamination would drive a single high gain amplifier into saturation.

Alternatively the gain of the amplifier could be reduced or the lower cutoff frequency could be increased at the expense of signal-to-noise ratio and lower frequency information, respectively. Therefore, the adopted alternative is to divide the spectrum into two separate frequency bands, one covering the lower frequencies at low gain and the other covering the higher frequencies at high gain. This way a reasonable signal-to-noise ratio is obtained by the high gain stage

while the low-frequency information with the rocket spin is monitored by the low gain stage.

In FM/FM systems, the received noise spectrum has the form $N(f) \propto f^2$. As mentioned earlier, the anticipated fine structure spectrum will have the form $S(f) \propto f^{-n}$; therefore, at higher frequencies the noise spectral density may be quite large in comparison with the signal spectral density which results in a decreased signal-to-noise ratio. To reduce this degradation of signal-to-noise ratio at higher frequencies, pre-emphasis is incorporated into the broadband amplifiers.

In previous equatorial flights, a single broadband amplifier with a voltage gain of 100 and a 3 dB bandwidth ranging from 50 Hz to 3 kHz was used. With a voltage gain of 100, the amplifier provided a maximum signal excursion of 4.5 V (on a 0-5 V scale), the dominating frequency components being around 100 Hz. To prevent exceeding the dynamic range of the system a maximum gain of 40 dB at 100 Hz must be maintained. In addition to this requirement the higher frequency components require emphasis to increase the signal-to-noise ratio as the irregularity spectrum rolls off. Both requirements are achieved using a broadband amplifier with the lower frequency roll-off exhibited in Figure 2.15a. With a voltage gain of 400 and a 3 dB lower frequency cutoff at 400 Hz, the gain is reduced by 6 dB/octave at lower frequencies, which corresponds to a voltage gain of 100 at 100 Hz. Likewise the gain grows beyond 100 as frequency increases, finally reaching its maximum of 400. Therefore all frequencies above 100 Hz are emphasized, frequencies below

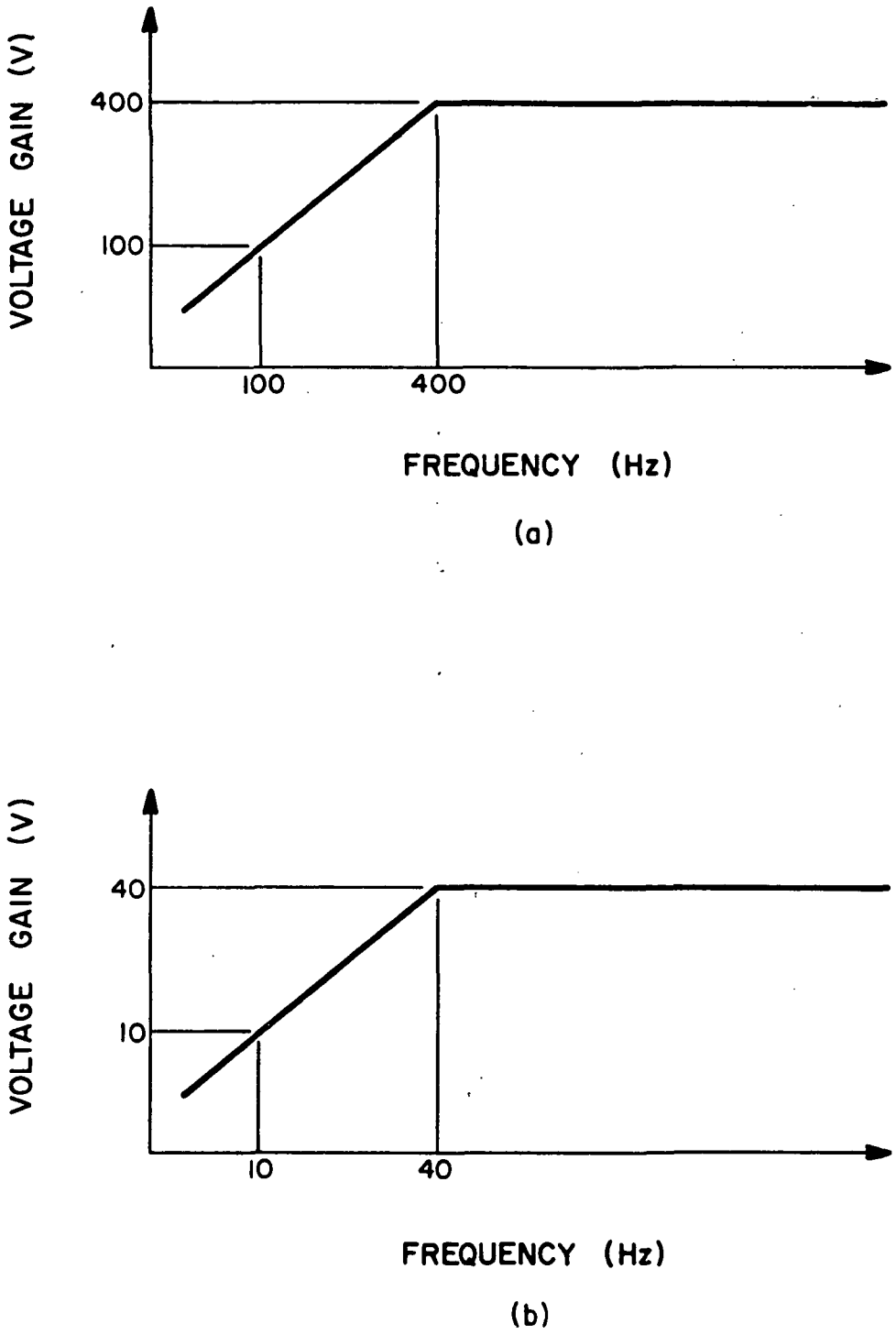

Figure 2.15. Pre-emphasis in broadband amplifiers.

100 Hz are de-emphasized and the maximum signal excursion requirement is met.

With this design for broadband amplifier 1, the rejection at the spin contamination is 24 dB relative to the response at 100 Hz providing ample protection from saturation. The useful bandwidth for this amplifier ranges from about 50 Hz to the upper frequency cutoff which was chosen to be 5 kHz. Unfortunately, information below 50 Hz is lost; hence broadband amplifier 2 is used to retain this information along with the spin contamination. Experience has shown that a voltage gain of 10 at the spin contamination frequency precludes the possibility of saturation. This requirement with the need for pre-emphasis results in the low frequency rolloff shown in Figure 2.15b. The upper frequency cutoff was again chosen as 5 kHz so that both broadband amplifiers overlap the same frequency spectrum to provide redundancy in case of an in-flight failure.

The schematic of the broadband amplifier section is illustrated in Figure 2.16. A voltage follower serves as the front end to prevent any interaction between the amplifiers and the logarithmic electrometer. The signal is then split between the two broadband amplifiers whose outputs are routed to the narrowband filter sections and to telemetry channels 20 and 21 with bandwidths of 9.3 kHz and 12.4 kHz, respectively (for a modulation index of one).

Broadband amplifier 1 has a dynamic range of 14% $\Delta N/N$ for irregularities containing 100 Hz components and, due to the pre-emphasis, this range decreases for increasing frequency until it reaches

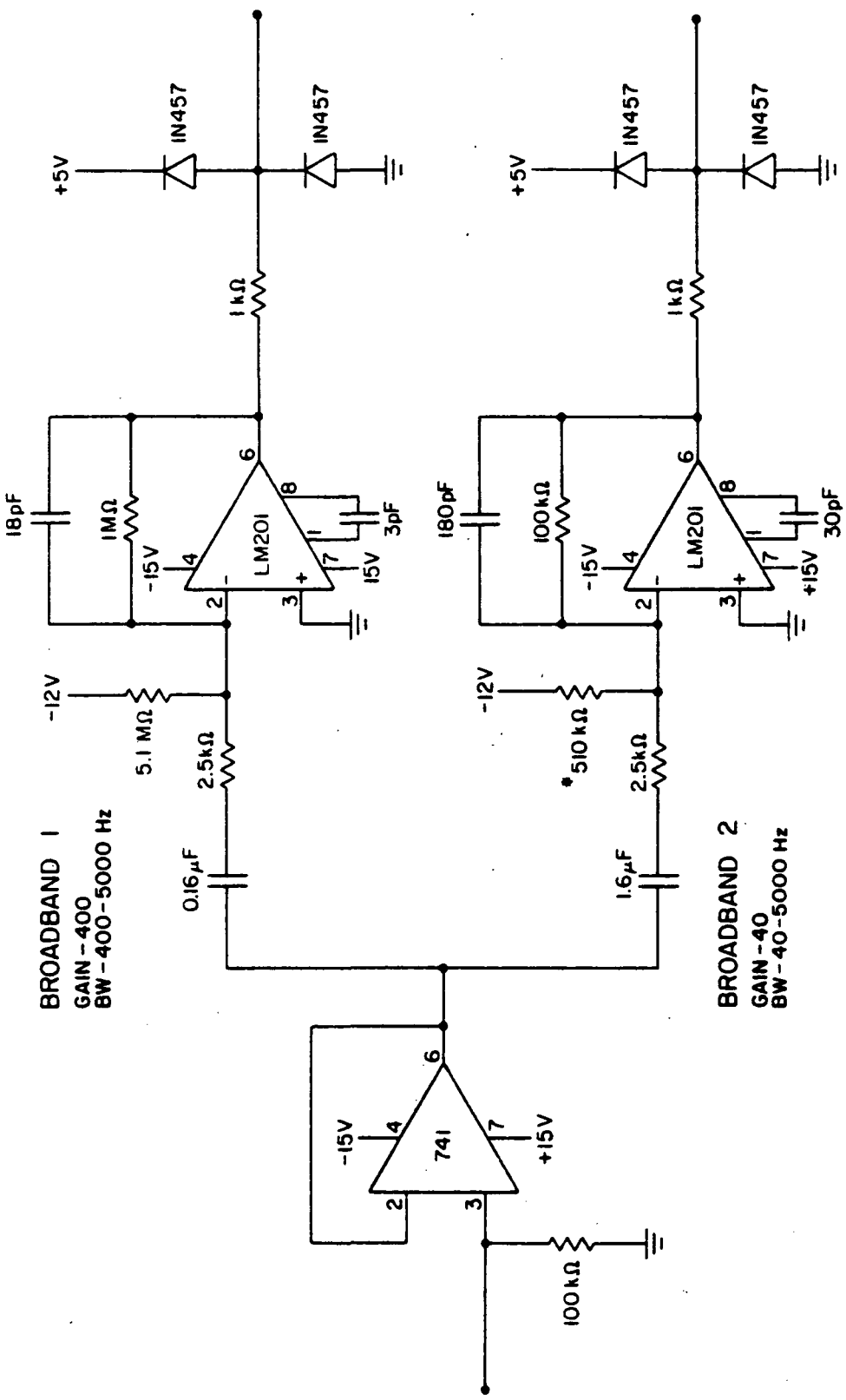

* This bias resistor is omitted in payloads 31.028 and 31.029. Instead, the 2.5V bias is provided by a 741 at the output of the LM201.

Figure 2.16. Schematic of broadband amplifiers.

its value of 4% for components above 400 Hz. Similarly, the dynamic range for broadband amplifier 2 is 140% $\Delta N/N$ for irregularities containing 10 Hz components steadily decreasing to 35% for components above 40 Hz. The details of these calculations are shown in Figure 2.17.

The narrowband branches are composed of a narrowband filter, a post-amplifier and, in the case of the 1 kHz branch, a rectifier/low-pass filter combination. The objective of the narrowband filters is to provide continuous samples of the irregularity spectrum at frequencies of 100 Hz and 1 kHz. These samples may then be envelope detected and a spectral slope could then be computed providing rapid evaluation of the data after the rocket flights, a back-up to the computer analysis of the spectral slope and redundancy in the event of an in-flight failure.

Ideally, an extremely narrow bandwidth filter is desirable in order to obtain an accurate estimate of the spectrum at a particular frequency. Unfortunately, the spectrum is highly variable as a function of altitude with very sharp changes in electron density which would cause a high Q filter to ring significantly. This ringing manifests itself in the envelope of the signal, thereby introducing error in the measurement. To minimize ringing a filter Q of 2, corresponding to a 50% bandwidth is chosen. KLAUS AND SMITH [1978] have shown that with the given spectral shape, an increase in the filter bandwidths within reason, will result in erroneous samples of the spectrum; however, the spectral index computed from the samples will remain very close to the

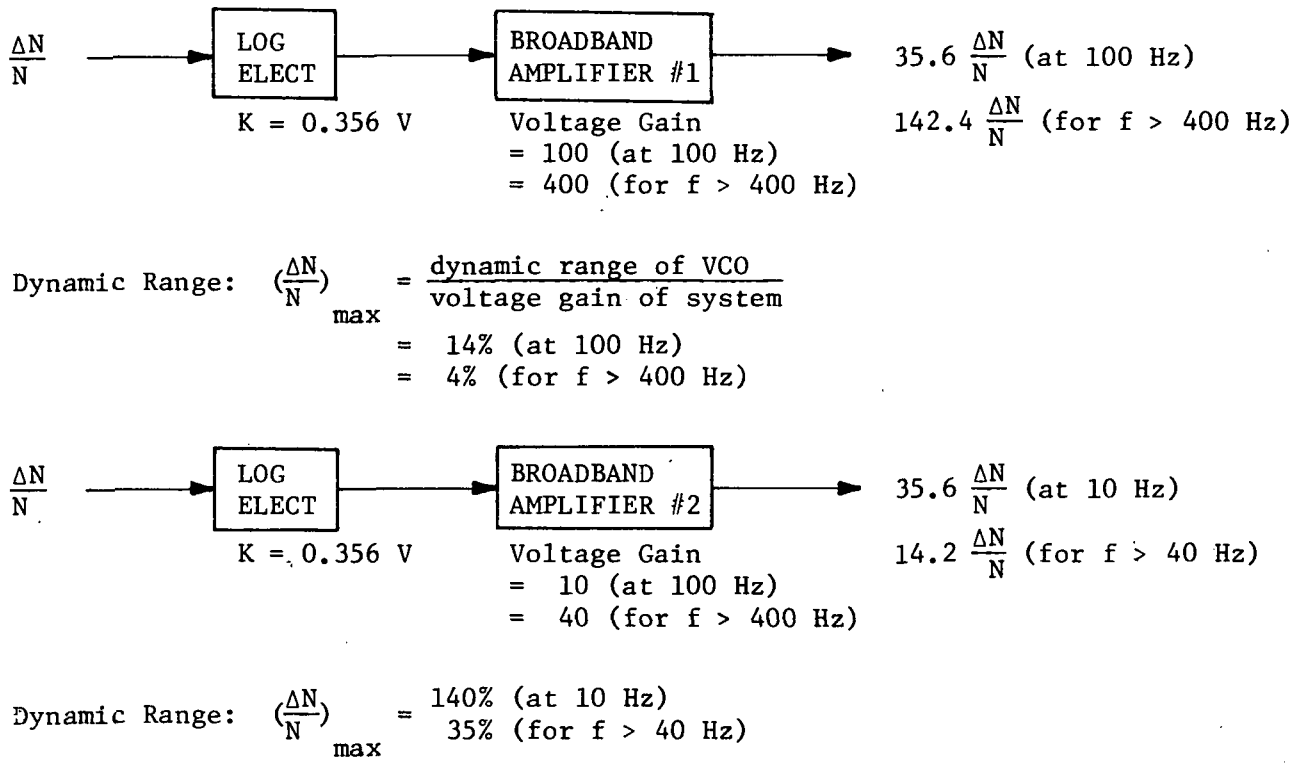

Figure 2.17 Dynamic range of broadband amplifiers.

actual index. Therefore, the 50% filter bandwidths prevent substantial ringing without adversely affecting the spectral index measurement.

The two telemetry channels available for the narrowband branches are IRIG Channels 10 and 11 with bandwidths of 81 Hz and 110 Hz, respectively (for a modulation index of five). This creates an interesting problem concerning channel assignments. Suppose an instantaneous increase in electron density irregularities occurs in the 100 Hz components. This would result in an instantaneous increase in the amplitude of the 100 Hz signal out of narrowband 2 which would be detected at the output of the rectifier on the order of 1/200 Hz = 5 ms (Figure 2.18). The information bandwidth of the narrowband 2 branch is 200 Hz. Similarly, 2 kHz is the maximum bandwidth of narrowband filter 1. Given the available channels and the desire to maximize the amount of information transmitted, any filtering beyond that of the channel is undesirable and therefore omitted. For this reason it is preferable to transmit the full-wave rectified signal and perform envelope detection on the ground. This method, however, presents a problem also. The channel distorts the waveform by bandlimiting the rectified signal which has infinite bandwidth. This distortion affects the envelope and is undesirable; consequently, the rectification and low-pass filtering are omitted in the narrowband 2 branch and the output is simply amplified and sent to channel 11. Since the information bandwidth is grossly large in comparison with the available channel bandwidths, the signal out of narrowband 1 (1 kHz) is full-wave rectified and low-pass filtered at approximately 85 Hz. This signal is then sent out on channel 10.

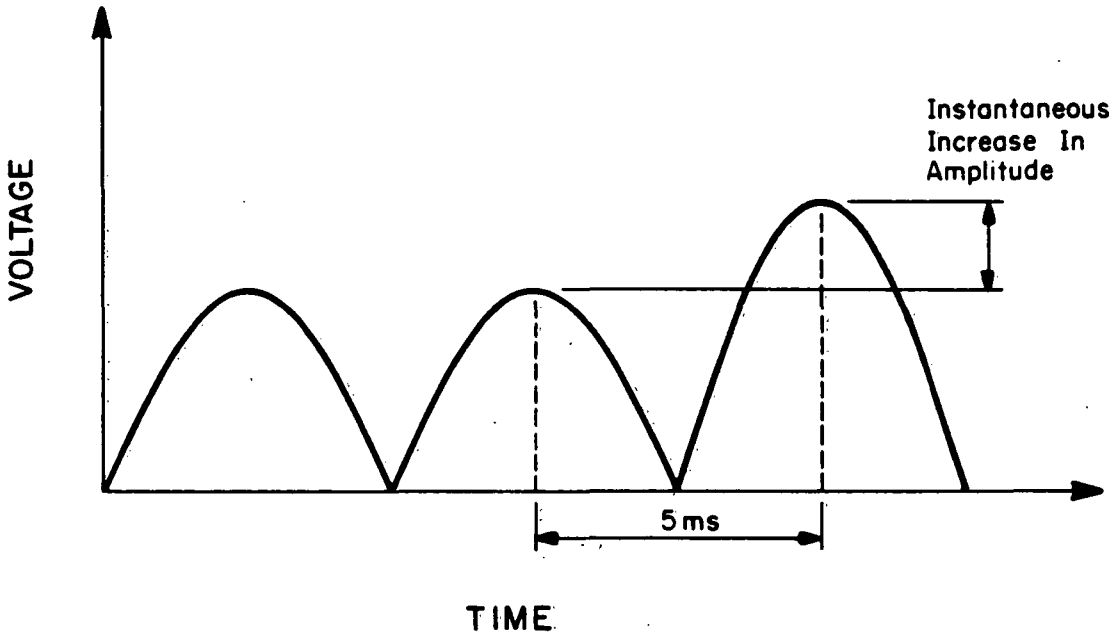

Figure 2.18. Full-wave rectified output of 100 Hz narrowband filter branch exhibiting the effect of an instantaneous increase in electron density.

The final issue concerning the narrowband branches is the gain of the post-amplifiers. The gain of the post amplifiers must be as large as possible without allowing saturation. Therefore, the optimum gain provides maximum signal excursion for the largest expected input voltage. The maximum signals expected in the frequency bands of interest are calculated from data obtained by KLAUS AND SMITH [1978] in their analysis of electrojet irregularities at the magnetic equator. The maximum normalized RMS amplitudes, $E_n(f)$, in the frequency bands of interest were found to be $E_n(100\ Hz) = 100 \times 10^{-6}$ V/Hz at 90 km and $E_n(1$ kHz$) = 3 \times 10^{-6}$ V/Hz at 110 km. Following is an analysis of the signal strengths at the output of the system.

For the 1 kHz branch, the maximum denormalized RMS amplitude is $E(1$ kHz$) = (3 \times 10^{-6}$ V/Hz$)$ (500 Hz) = 1.5 mV or 0.15%. The logarithmic electrometer produces an output of 3.5 mV for a 1% change in input current; thus an input of 0.15% produces 0.525 mV at the output. Broadband 1 boosts the signal magnitude by 400. The filter provides no loss or gain and the rectifier/low-pass filter combination provides an effective voltage gain of $1/\pi$ (The rectifier halves the peak-to-peak excursion of the signal, while the low-pass filter extracts the average value of the full-wave rectified signal, which for a sinusoid is $2/\pi$ times the peak amplitude). To prevent saturation, the maximum gain of the entire branch must not exceed 5V/2.1 mV(peak) = 2381. Therefore, the voltage gain of the post-amplifier in the 1 kHz branch must not exceed $2381/140(1/\pi) = 53$.

For the 100 Hz branch, the maximum denormalized RMS amplitude is $E(100\ Hz) = (100 \times 10^{-6}$ V/Hz$)$ (50 Hz) = 5 mV or 0.5%. The gain of the

electrometer (x0.35) combined with the gain of broadband 2 (x40) provides a total voltage gain of 14. Since this signal is not full wave rectified and filtered, the maximum voltage gain of the post-amplifier is bounded by (5V/7.1mV)/14 = 50.

To allow for the possibility of large signal strengths, the post-amplifier voltage gains are set at 10. This value should provide a reasonable increase in signal-to-noise ratio while reducing the risk of clipping the signals which would distort the spectrum. With this gain, the ranges of $\Delta N/N$ of the narrowband branches are 3.5% and 1.1% for the 100 Hz and 1 kHz branches, respectively (See Figure 2.19).

The circuit schematic of the narrowband filter branches is shown in Figure 2.20.

2.5 Equatorial Fine Structure Experiment Calibration and Special Issues

Following is an account of the calibration of the hardware used for equatorial flights 31.028 and 31.029 along with some special issues concerning the hardware implementation.

2.5.1 Calibration.

Table 2.3 contains the current-to-voltage measurements for the input current range 10^{-10} A to 10^{-4} A for the logarithmic electrometers. These measurements were performed using a 1V source and a set of calibrated resistors to provide the precise current levels. The output voltages during the beginning of the sweep mode are included

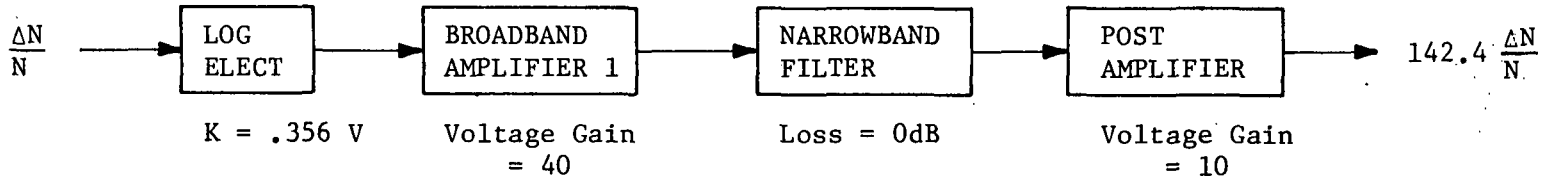

Dynamic Range: $(\frac{\Delta N}{N})_{max} = \frac{5\ V}{142.4\ V} = 3.5\%$

a.) 100 Hz narrowband branch

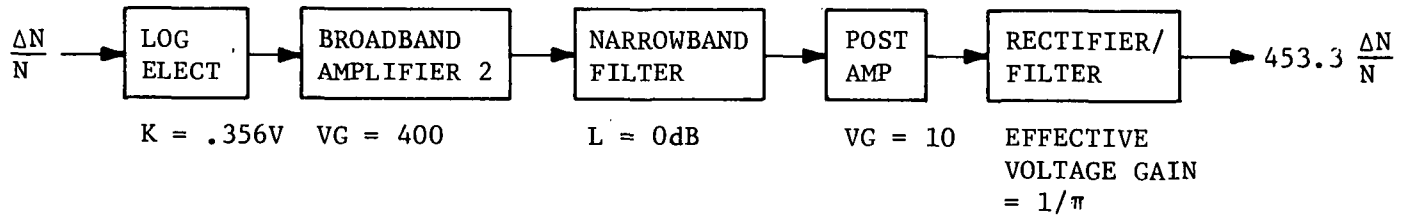

Dynamic Range: $(\frac{\Delta N}{N})_{max} = 1.1\%$

b.) 1 kHz narrowband branch

Figure 2.19 Dynamic range of narrowband filter branches.

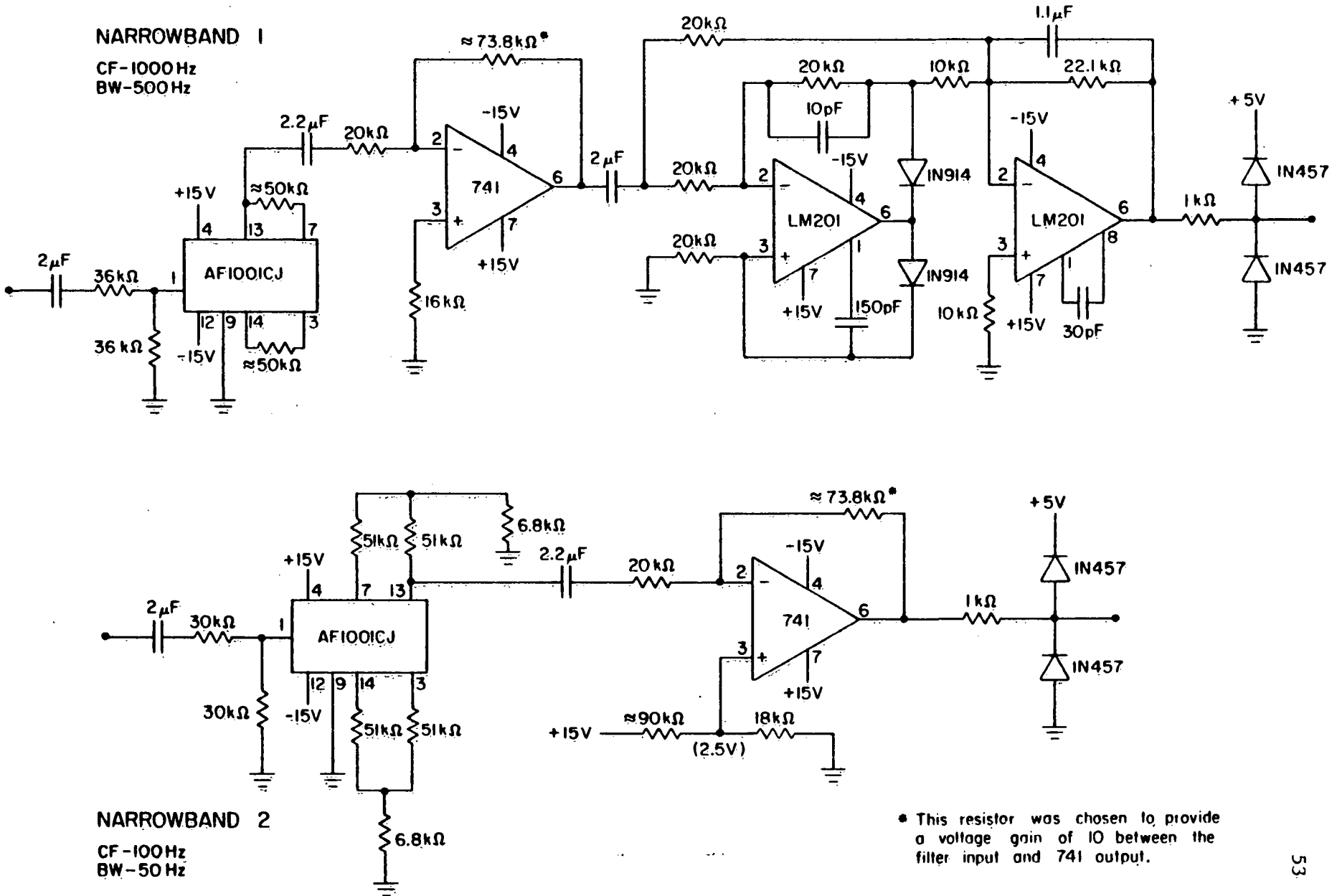

Figure 2.20. Schematic of narrowband filter branches.

Table 2.3 Logarithmic electrometer calibrations for Project Condor

Input Current (A)	Output Voltage (V)	Swept Output Voltage (V)	Voltage Gain (V/decade)
Flight 31.028			
10^{-10}	0.96	0.04	
10^{-9}	1.64	0.19	0.68
10^{-8}	2.38	0.71	0.74
10^{-7}	3.19	1.35	0.81
10^{-6}	4.01	2.06	0.82
10^{-5}	4.82	2.85	0.81
10^{-4}	5.95	3.63	1.13
Cal*	4.39	2.41	
Flight 31.029			
10^{-10}	0.98	0.00	
10^{9}	1.63	0.19	0.65
10^{-8}	2.38	0.68	0.75
10^{-7}	3.20	1.33	0.82
10^{-6}	4.03	2.00	0.83
10^{-5}	4.85	2.79	0.82
10^{-4}	6.00	3.59	1.15
Cal*	4.41	2.36	

*This measurement is the output voltage when the logarithmic electrometer is in the self-calibration mode.

for completeness.

Table 2.4 contains the frequency response of the logarithmic electrometers as a function of average input current. These measurements were made using the risetime-falltime method described by KLAUS AND SMITH [1978].

Table 2.5 displays the frequency response measurements for the broadband amplifiers. These measurements were performed by injecting a signal of known frequency and magnitude and monitoring the output signal magnitude. Similarly, Table 2.6 contains the frequency response measurements for the narrowband branches. The method of measurement was identical to that of the broadband amplifiers.

2.5.2 Special issues.

It should be mentioned that the calculations in Sections 2.3.2 through 2.3.5 are still valid for the equatorial experiment. In addition to those issues, one peculiar only to the equatorial experiment arose.

With the experiment fully assembled, a preliminary observation of the output of the fine structure experiment with the probe shielded disclosed high noise levels. The noise voltages of 100 mV (peak-to-peak) out of broadband 1 and 10 mV (peak-to-peak) out of broadband 2 were primarily due to a large noise level at the input to the fine structure board. The source was a 1 kΩ resistor located between the output of the logarithmic electrometer and the input of the fine structure experiment. The intent of this resistor was to provide a load

Table 2.4 Frequency response of logarithmic electrometers for Project Condor, 1983

Input Current (A)	-3dB Frequence Cutoff (Hz) Flight 31.028	Flight 31.029
10^{-9}	262	230
10^{-8}	1800	1800
10^{-7}	7300	9200
10^{-6}	14700	18300
10^{-5}	14100	24400
10^{-4}	13100	18300

Table 2.5 Frequency response of broadband amplifiers

Frequency (Hz)	Voltage Gain Flight 31.028	Flight 31.029
Broadband Amplifier 1		
40	34	33
100	82	80
200	156	150
400	265	260
500	300	295
1000	375	375
1500	400	395
2000	400	400
3000	375	375
4000	345	350
5000	315	320
6000	290	290
7000	265	265
8000	240	245
Broadband Amplifier 2		
4	1.7	2.0
10	8.0	8.5
20	16.0	17.5
30	22.0	24.5
40	27.0	28.3
50	30.0	32.0
60	32.0	33.5
70	33.5	35.5
80	35.0	36.5
90	35.0	37.0
100	36.0	38.0
200	39.5	41.0
400	41.0	42.5
500	41.0	42.5
1000	41.0	42.5
5000	38.5	40.0
10000	38.0	35.0

Table 2.6 Frequency response of narrowband filter branches

Frequency (Hz)	Voltage Gain Flight 31.028	Flight 31.029
Narrowband Branch 1		
100	0.5	0.6
500	3.4	3.4
600	4.4	4.6
700	5.8	6.0
800	7.8	8.0
900	9.6	9.8
1000	10.4	10.4
1100	9.6	9.4
1200	8.2	8.2
1300	7.0	7.2
1400	5.9	5.9
1500	5.2	5.2
2000	3.2	3.3
10000	0.5	0.5
Narrowband Branch 2		
10	0.4	0.4
20	1.0	0.9
30	1.7	1.5
40	2.4	2.2
50	3.2	2.9
60	4.4	4.0
70	5.8	5.3
80	8.0	7.4
90	9.8	9.2
100	10.4	10.2
200	3.1	2.9
300	1.8	1.8
400	1.3	1.2
500	1.0	1.0
600	0.9	0.8
700	0.7	0.7
800	0.6	0.6
900	0.5	0.5
1000	0.5	0.5

at the output of the electrometer in case of an accidental short to ground during prelaunch testing. The resistor, however, increased the output impedance of the electrometer, increasing the magnitude of the equivalent noise source at the input to the broadband amplifiers.

To correct the problem, the output of the electrometer is fed directly to the input of the fine structure experiment and the 1 kΩ resistor is placed between the output of the electrometer and the telemetry transmitter VCO. This arrangement reduces the noise levels out of the broadbands to 5 mV (peak-to-peak) and still provides the short-circuit protection to the electrometer. The modified electrometer circuit is shown in Figure 2.21.

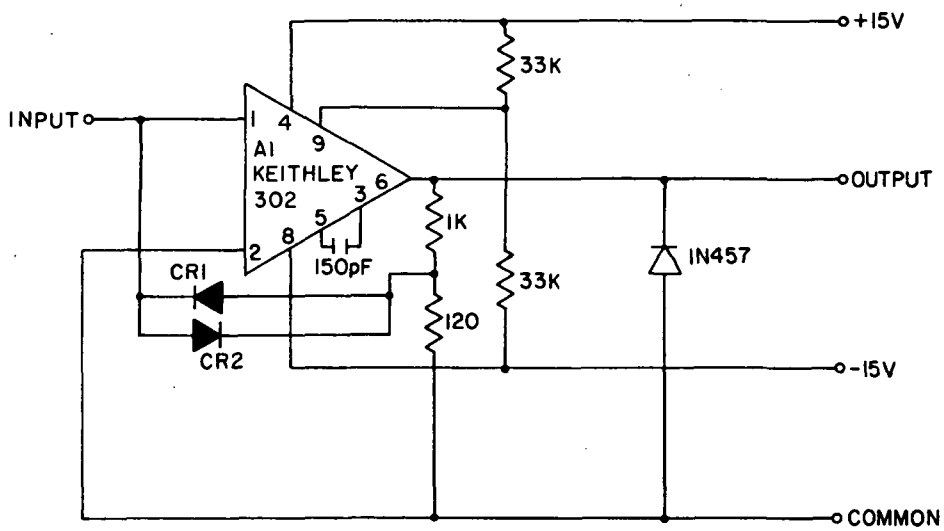

Figure 2.21. Schematic of modified logarithmic electrometer for Project Condor.

3. SPECTRAL ANALYSIS

3.1 Introduction

It is of interest at this point to investigate the method of extracting the desired information from the output of the fine structure experiment. The objective is to characterize the irregularities in the electron density as a function of altitude over a finite time interval. With this in mind, Fourier decomposition becomes an attractive approach, characterizing the fluctuations as a sum of periodic functions with differing frequencies and amplitudes.

As an example, assume a sinusoidal variation of relative electron density with altitude, expressed by

$$\Delta N/N\ (h) = A \sin 2\pi fh = A \sin(2\pi/\lambda)h, \tag{3.1}$$

where A is the magnitude of the density variation relative to the ambient density, h is the altitude, f is the spatial frequency, and λ is the spatial wavelength (scale size). A probe travelling upward with a velocity v encounters a variation with time of the form

$$\Delta N/N\ (t) = A \sin(2\pi v/\lambda)t = A \sin 2\pi f_o t, \tag{3.2}$$

where

$$f_o = v/\lambda.$$

This variation is converted in the circuit of the fine structure experiment to a voltage

$$V_{out}(t) = G\ A \sin 2\pi f_o t, \tag{3.3}$$

where G is the fine structure system gain. Fourier analysis of this voltage produces a spectrum consisting of a pair of delta functions at the frequencies f_o and $-f_o$

$$S(f) = \frac{G^2 A^2}{4} [\delta(f - f_o) + \delta(f + f_o)]. \tag{3.4}$$

The magnitude and scale size of the variation are then determined by the magnitude and frequency of the delta function and the probe velocity, v.

In the general case, the variation of relative electron density is modelled as a random process with a power spectral density of the form

$$S(f) = S_o f^{-n}\ ; \qquad f = v/\lambda, \tag{3.5}$$

where n is a positive rational number. The exponent (-n) is referred to as the spectral index and, along with the constant S_o, completely characterizes the spectral shape. (In the literature, n (not -n) is sometimes referred to as the spectral index). In this model, the spectral magnitude S_o and the spectral index -n, vary as a function of altitude reflecting the changes in amplitude distribution among the various scale sizes. The task at hand is therefore

(1) to compute a power spectral density from the acquired data as a function of altitude,

(2) to fit the computed spectra to the model spectrum $S(f) = S_o f^{-n}$ thereby obtaining the spectral magnitude and index as a function of altitude, and finally

(3) to correlate these data to electron density irregularity variations versus altitude.

In light of this, several questions come to mind. First of all, what is an appropriate estimator for the spectral density? Since the Fourier transform exists only for functions defined for all time, what are the effects of computing a transform for finite data? Another point to consider is the stationarity of the data. The random process of interest is characterized by a power spectral density which varies with time, henceforth, by definition the process is nonstationary. This presents a substantial obstacle to Fourier analysis which is based on the premise of stationary data. The answers to these questions lie in the concepts of spectral estimation.

3.2 Spectral Estimation

3.2.1 Background. Estimation of the power spectral density of a random process is primarily based on the computation of the discrete Fourier transform defined by

$$X(k) = \sum_{n=0}^{L-1} x(n) e^{-j \frac{2\pi}{M} nk}; \quad k = 0,\ldots,M-1; \tag{3.6}$$

where x(n); n = 0,...,L-1 are the L discrete data samples of the random process and X(k), k = 0,...,M - 1 are the M Fourier coefficients (Note that $M \geq L$). The inverse of this transform expresses the random process x(n) as a finite sum of complex exponentials weighted by the complex Fourier coefficients and is given by

$$x(n) = \frac{1}{M} \sum_{k=0}^{M-1} X(k) e^{j \frac{2\pi}{M} nk} \quad ; \; n=0,\ldots,L-1 \text{ and } M \geq L. \tag{3.7}$$

Since the major concern is how well this transform approximates the continuous Fourier transform, it is worthwhile investigating their relationship through a simple example.

Suppose the process under consideration is given by the sinusoid defined for all time in Figure 3.1(a), along with its Fourier representation (magnitude only). Next the data are sampled with the comb function illustrated in Figure 3.1(b). Since multiplication in the time domain transforms to convolution in the frequency domain, the result is the infinite, periodic extension of the original spectrum shown in Figure 3.1(c). Assuming that only a segment of the data is available for observation is equivalent to multiplying the sampled sinusoid by an observation window shown in Figure 3.1(d). This again transforms to convolution resulting in the spectrum of Figure 3.1(e). Already the effects of taking a finite data sample are evident. The next step is to discretize the spectrum facilitating computer analysis. This is

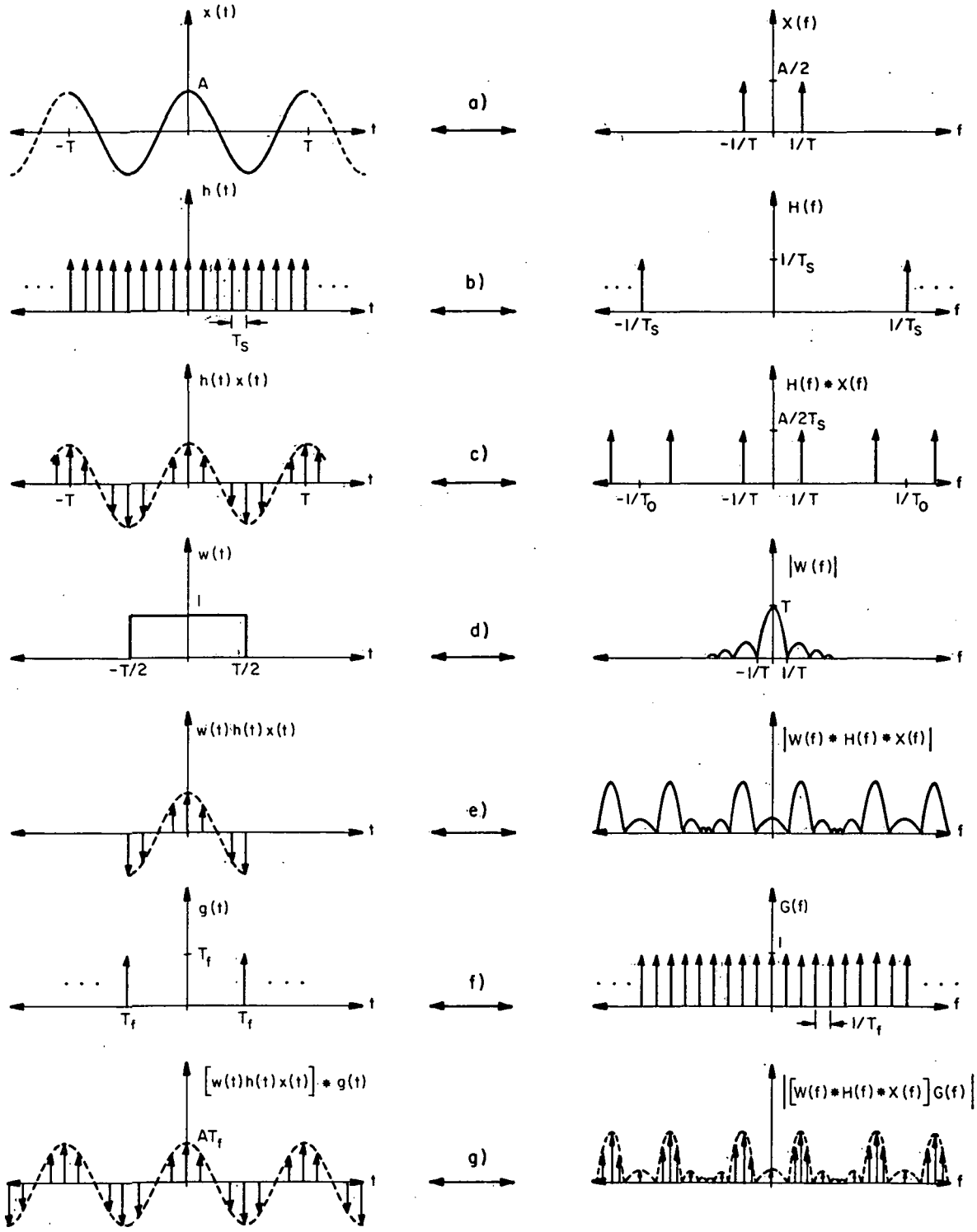

Figure 3.1. Graphical derivation of the Discrete Fourier Transform (adapted from BRIGHAM, 1974).

accomplished by multiplying the spectrum by a comb function shown in Figure 3.1(f). The final result is a periodic, discrete process represented by a periodic discrete Fourier representation (Figure 3.1(g)). Note, however, that both are completely defined by one period of their respective discrete waveforms and hence the convenience of using the discrete Fourier transform is realized. But most important of all, the discrete Fourier transform has very simply been shown to be a corrupted, periodic version of the continuous Fourier transform.

As we shall see, the form and degree of the corruption may be predicted and controlled, thereby lending the discrete Fourier transform (DFT) as a reasonable approximation of the continuous Fourier transform.

3.2.2 Estimator of spectral density. Calculation of the spectral density of a random process presupposes the availability of the sample function for all time. Since the data consist of a finite number of samples from the sample function, only an estimate of the spectral density may be obtained. A derivation of the estimator used in the analysis of electron density irregularities follows. The statistical performance of the estimator will then be investigated in the next section.

Suppose $x(n)$ is a set of samples from a continuous, stationary, and ergodic random process $x(t)$. Assume also that only L data points are available ($n = 0, 1, \ldots, L - 1$). The Wiener-Khinchin theorem relates $R_x(\tau)$, the autocorrelation function of the continuous random process $x(t)$, to the power spectral density function $S(f)$ via the Fourier transform relation

$$S(f) = \int_{-\infty}^{\infty} R_x(\tau)\, e^{-j2\pi f\tau} d\tau, \tag{3.8}$$

where

$$R_x(\tau) = E[x(t)\, \hat{x}(t + \tau)]. \tag{3.9}$$

The caret "^" denotes the complex conjugate of x(t). Ergodicity implies that expectations may be replaced with time averages allowing Equation 3.9 to be rewritten as

$$R_x(\tau) = \lim_{T\to\infty} \frac{1}{2T} \int_{-T}^{T} x(t)\, \hat{x}(t + \tau)\, dt. \tag{3.10}$$

From this equation and Equation 3.8, it may be shown that

$$S(f) = \lim_{T\to\infty} E\left\{ \frac{1}{2T} \left| \int_{-T}^{T} x(t)\, e^{-j2\pi ft} dt \right|^2 \right\}. \tag{3.11}$$

The expectation operator is required for convergence of the limit and must be taken into account as will be seen.

We would now like to extend this expression to account for discrete data. Sampling of the random process x(t) every T_s seconds generates a sequence of random variables $x(nT_s)$; n = ...-2, -1, 0, 1, 2....

Assuming that L of these samples are contained in the interval [-T, T], the integral in Equation 3.11 may be approximated by

$$\int_{-T}^{T} x(t)e^{-j2\pi ft}\,dt \rightarrow T_s \sum_{n=0}^{L-1} x(nT_s)e^{-j2\pi k\,\Delta f\,nT_s} . \qquad (3.12)$$

The factor T_s is a result of the rectangular approximation of the integral and is required to conserve area under the curve. Δf is the discretized frequency spacing which is a function of the sampling interval and the number of Fourier coefficients (= $1/MT_s$ where $M \geq L$). Therefore, the smallest possible frequency interval is $1/LT_s$.

Substituting this discrete version of the integral into Equation 3.11 yields

$$S(k\Delta f) = \lim_{L,M\rightarrow\infty} E\left\{\frac{1}{MT_s}\left| T_s \sum_{n=0}^{L-1} x(nT_s)e^{-j\frac{2\pi}{M}kn}\right|^2\right\} \qquad (3.13)$$

This expression within the absolute value operator is the previously defined discrete Fourier transform reducing the expression to

$$S(k) = \lim_{L,M\rightarrow\infty} E\left\{\frac{1}{MT_s}\,T_s^2\left|X(k)\right|^2\right\} . \qquad (3.14)$$

Obviously it is impossible to compute the limit when L (and M) is constrained to be finite. Likewise, the expectation of the function of the random variable X(k) cannot be computed since only one sample

function has been observed. Therefore, the spectral density estimate will be defined as above with the limiting and expectation operators deleted.

$$\tilde{S}(k) = \frac{T_s}{M} \left| X(k) \right|^2 \quad ; k = 0,\ldots,M-1. \tag{3.15}$$

With the limiting and expectation operators removed, the estimate $\tilde{S}(k)$ may be viewed as a random variable with an associated mean and variance. It would be desirable for the mean of the estimator to equal the actual spectrum and the variance to be as small as possible; however, this is not always the case. These statistics and how they may be manipulated will be discussed shortly. For the present it will be assumed that the estimator of Equation 3.15 is statistically acceptable.

It was mentioned earlier that the electron density irregularity sizes may be deduced from the magnitude and frequency distribution of the spectrum. The characteristics of the frequency distribution generated by the discrete Fourier transform are well documented; however, the characteristics of the magnitude generated by the transform as compared to the actual continuous spectrum are seldom mentioned. This omission is primarily due to the fact that in most practical cases of spectral estimation, only relative magnitude is of interest (i.e., looking for a sinusoid in a noise background). For the fine structure experiment, the absolute magnitude is of prime importance. With this in mind, we will investigate the estimator's performance in regard to

magnitude estimation.

Since the objective of this analysis is to estimate the spectrum of a noise process, the scaling property of the estimator on "white" noise will be computed as the general case. Assuming the noise process has a total power of σ^2, the autocorrelation and spectral density functions are given by

$$R_N(n) = \sigma^2 \quad \delta(n),$$

$$S_N(k) = \sigma^2 T_s.$$

The estimator to be used is again given by

$$\tilde{S}(k) = \frac{T_s}{M} \left| X(k) \right|^2 \quad ; \; k = 0,\ldots,M-1. \tag{3.16}$$

The question is whether or not the mean of the random process $\tilde{S}(k)$ accurately represents the white noise process with respect to magnitude. This will be answered by comparing the total power of the estimate with the total power of the original process.

The DFT of a sample function of the random process is

$$X(k) = \sum_{n=0}^{L-1} x(n)\, e^{-j \frac{2\pi}{M} nk} \quad ; \; k = 0,1,\ldots,M-1. \tag{3.17}$$

Since x(n) is a random process and X(k) is a function of a random process, it too is a random process with autocorrelation function

$$R_X(k,m) = E[X(k)\,\hat{X}(m)]$$

$$= E\left\{\sum_{n=0}^{L-1} x(n)e^{-j\frac{2\pi}{M}nk} \sum_{l=0}^{L-1} \hat{x}(l)e^{j\frac{2\pi}{M}lm}\right\}$$

$$= \sum_{n=0}^{L-1}\sum_{l=0}^{L-1} E\left\{x(n)\,\hat{x}(l)\right\} e^{-j\frac{2\pi}{M}nk} e^{j\frac{2\pi}{M}lm}$$

$$= \sum_{n=0}^{L-1}\sum_{n=0}^{L-1} \sigma^2\,\delta(n-l)\, e^{-j\frac{2\pi}{M}nk} e^{j\frac{2\pi}{M}lm}$$

$$= \sum_{n=0}^{L-1} \sigma^2\, e^{-j\frac{2\pi}{M}n(k-m)} . \qquad (3.18)$$

Letting $z = k - m$,

$$R_X(z) = \sum_{n=0}^{L-1} \sigma^2\, e^{-j\frac{2\pi}{M}z} . \qquad (3.19)$$

The expected value of the estimator is then given by

$$E\{\tilde{S}(k)\} = \frac{T_s}{M} E\{ |X(k)|^2 \}$$

$$= \frac{T_s}{M} R_X(0) = \frac{T_s}{M} \sum_{n=0}^{L-1} \sigma^2$$

$$= \frac{LT_s}{M} \sigma^2 . \qquad (3.20)$$

The total power in the estimate is

$$\tilde{P}_T = \sum_{k=0}^{M-1} E\{\tilde{S}(k)\} \Delta f; \qquad \Delta f = \frac{1}{MT_s}$$

$$= \sum_{k=0}^{M-1} \frac{LT_s}{M^2 T_s} \sigma^2$$

$$= \frac{L}{M} \sigma^2 . \qquad (3.21)$$

But the original process had a total power of σ^2. Therefore, to correct for the "gain" of the estimator, a corrected estimator of the form

$$S(k) = \left(\frac{M}{L}\right) \frac{T_s}{M} \left|X(k)\right|^2 = \frac{T_s}{L} \left|X(k)\right|^2; \quad k=0,\ldots,M-1 \tag{3.22}$$

will be used.

It was mentioned earlier that the spectrum of the output of the fine structure experiment may be corrupted by a sinusoid (and harmonics) due to the spin of the rocket. In order to provide additional information regarding this corruption for future flights, it is of interest to calculate the estimator gain for a sinusoidal component.

Let the discrete waveform be given by

$$x(n) = A \cos (2\pi f n T_s); \quad n = 0,1,\ldots,L-1. \tag{3.23}$$

The M-point DFT is

$$X(k) = \sum_{n=0}^{L-1} x(n) e^{-j \frac{2\pi nk}{M}} ; \qquad k = 0,1,\ldots,M-1. \tag{3.24}$$

For positive frequencies, this transform becomes

$$X_+(k) = \frac{A \sin\left[\frac{\pi L(k-fMT_s)}{M}\right]}{2 \sin\left[\frac{\pi(k-f\,MT_s)}{M}\right]} \; e^{-j\frac{\pi(k-fMT_s)\,(L-1)}{M}} \tag{3.25}$$

The spectral estimate for positive frequencies then becomes

$$\tilde{S}(k) = \frac{T_s}{L} \; |X_+(k)|^2$$

$$= \frac{T_s A^2}{4L} \; \frac{\sin^2\left[\frac{\pi L(k-fMT_s)}{M}\right]}{\sin^2\left[\frac{\pi(k-fMT_s)}{M}\right]} \; . \tag{3.26}$$

Assuming that an integral number of cycles of x(n) are present in the L samples, the estimate will be sampled at the peak (i.e., $k = fmT_s$) of the given function yielding

$$\tilde{S}(k) = \frac{A^2 T_s}{4L} (L^2) = LT_s \, (A^2/4) \tag{3.27}$$

The actual power contained in the positive frequencies of the actual spectrum of a sinusoid is $(A^2/4)$; therefore the estimator gain for a discrete frequency component is LT_s.

3.2.3 Statistical properties of the estimator.

In the preceding section a spectral estimator for a discrete noise process was derived without regard to its statistical performance. Recalling Equation 3.14, the expectation and limit operators were omitted for two practical reasons: 1) It is impossible to compute the expectation of a random process with only one available sample function; and 2) the limit cannot be computed since L (and M) is a given finite number. By doing this, a set of random variables, $\tilde{S}(k)$; $k = 0,\ldots,M-1$ was created with its associated statistical parameters. The intention is to reveal the consequences of the omission by computing the statistics of the estimator and to justify its use under the resulting limitations.

To begin, let $x(n)$ be a discrete white noise process with mean zero and variance σ_x^2. Given only L data points and allowing M to equal L (no zero padding) for ease of computation, the spectral estimator may be written as

$$\tilde{S}(k) = \frac{T_s}{L} \left| X(k) \right|^2$$

$$= \frac{T_s}{L} \left| \sum_{n=0}^{L-1} x(n)\, e^{-j\frac{2\pi}{L}nk} \right|^2 ; \quad k=0,\ldots,L-1. \qquad (3.28)$$

Separating the complex transform into real and imaginary parts yields

$$\tilde{S}(k) = \frac{T_s}{L} \left[\left\{ \sum_{n=0}^{L-1} x(n) \cos \frac{2\pi}{L} nk \right\}^2 + \left\{ \sum_{n=0}^{L-1} x(n) \sin \frac{2\pi}{L} nk \right\}^2 \right]$$

$$= \frac{T_s}{L} [A(k)^2 + B(k)^2], \qquad (3.29)$$

where $A(k) =$

$$\sum_{n=0}^{L-1} x(n) \cos \frac{2\pi}{L} nk \quad \text{and} \quad B(k) = \sum_{n=0}^{L-1} x(n) \sin \frac{2\pi}{L} nk \ .$$

Equation 3.29 indicates that the statistics of S(k) may be deduced from those of A(k) and B(k). The mean of A(k) is

$$E[A(k)] = \sum_{n=0}^{L-1} E[x(n)] \cos \left(\frac{2\pi}{L} nk\right) \qquad (3.30)$$

$$= 0$$

since the mean of the random process x(n) was originally assumed to be

zero. The same argument holds for B(k) also. The variance of A(k) is then given by

$$\mathrm{Var}[A(k)] = E[A(k)^2]$$

$$= \sum_{n=0}^{L-1} E[x(n)^2] \cos^2\left(\frac{2\pi}{L} nk\right)$$

$$= \sigma_x^2 \sum_{n=0}^{L-1} \cos^2\left(\frac{2\pi}{L} nk\right). \tag{3.31}$$

Likewise,

$$\mathrm{Var}[B(k)] = \sigma_x^2 \sum_{n=0}^{L-1} \sin^2\left(\frac{2\pi}{L} nk\right). \tag{3.32}$$

These may be simplified further with the aid of the following identities.

$$\sum_{n=0}^{L-1} \cos^2\left(\frac{2\pi}{L} nk\right) = \begin{cases} L/2 & k=0,1,\ldots,L/2-1 \text{ and } L/2+1,\ldots,L-1. \\ \text{for} & \\ L & k=0,L/2\ . \end{cases} \tag{3.33}$$

$$\sum_{n=0}^{L-1} \sin^2\left(\frac{2\pi}{L} nk\right) = \begin{cases} L/2 & k=0,\ldots,L/2-1 \text{ and } L/2+1,\ldots L-1\ . \\ \text{for} & \\ 0 & k=0,\ L/2\ . \end{cases}$$

Hence, the variances of A(k) and B(k) are

$$\text{Var}[A(k)] = \begin{cases} \sigma_x^2 \, L/2 & \\ \sigma_x^2 \, L & \end{cases} \quad \text{for} \quad \begin{matrix} k=0,\ldots,L/2-1 \text{ and } L/2+1,\ldots,L-1. \\ k=0,\ L/2. \end{matrix} \tag{3.34}$$

$$\text{Var}[B(k)] = \begin{cases} \sigma_x^2 \, L/2 & \\ \sigma_x^2 \, L & \end{cases} \quad \text{for} \quad \begin{matrix} k=0,\ldots,L/2-1 \text{ and } L/2+1,\ldots,L-1. \\ k=0,\ L/2. \end{matrix}$$

Proceeding one step further,

$$\text{Cov}[A(k)\ A(l)] = E[A(k)\ A(l)]$$

$$= \sum_{n=0}^{L-1} \sum_{m=0}^{L-1} E[x(n)\ x(m)]\cos(\tfrac{2\pi}{L} nk)\cos(\tfrac{2\pi}{L} ml)$$

$$= \sum_{n=0}^{L-1} \sum_{m=0}^{L-1} \sigma_x^2\, \delta(n-m)\cos(\tfrac{2\pi}{L} nk)\cos(\tfrac{2\pi}{L} ml)$$

since x(n) was assumed to be a white noise process. This reduces to

$$\text{Cov}[A(k)\ A(l)] = \sigma_x^2 \sum_{n=0}^{L-1} \cos(\tfrac{2\pi}{L} nk)\cos(\tfrac{2\pi}{L} ml)$$

$$= 0 \text{ for } k \neq l. \tag{3.35}$$

Similarly, the covariance of B(k) is zero for all k not equal to l.

Also

$$\text{Cov}[A(k)\ B(1)] = \sigma_x^2 \sum_{n=0}^{L-1} \cos\left(\frac{2\pi}{L} nk\right)\sin\left(\frac{2\pi}{L} nl\right)$$

$$= 0 \text{ for all } k! \qquad (3.36)$$

All the necessary statistical parameters of A(k) and B(k) are now available for the computation of the mean and variance of the spectral estimator, $\tilde{S}(k)$.

First, the assumption that A(k) and B(k) are gaussian random variables will be stated. A(k) and B(k) are linear sums of random variables; hence, by the Central Limit Theorem their distributions tend to the gaussian distribution in the limit as L goes to infinity. Therefore, for large L, the above mentioned assumption is reasonable. Since the variances of these guassian random variables are known, they may be normalized in the following fashion:

$$A_N(k) = \frac{A(k)}{\sqrt{\text{Var}[A(k)]}} \ ; \ B_N(k) = \frac{B(k)}{\sqrt{\text{Var}[B(k)]}} \ . \qquad (3.37)$$

By Equation 3.36, $A_N(k)$ and $B_N(k)$ are uncorrelated random variables and thus independent because they are normally distributed. With these facts, a new set of random variables may be created

$$A_N^2(k) = \frac{A^2(k)}{\text{Var}[A(k)]} \ ; \ B_N^2(k) = \frac{B^2(k)}{\text{Var}[B(k)]} \qquad (3.38)$$

where by definition $A_N^2(k)$ and $B_N^2(k)$ have a chi-squared distribution of order one (χ_1^2). Furthermore, allow

$$Z(k) = A_N^2(k) + B_N^2(k) \tag{3.39}$$

where Z(k) is a chi-squared random variable of order two (χ_2^2). Using Equation 3.39, the mean and variance of $\tilde{S}(k)$ may be derived.

For k = 0 and L/2, B(k) and therefore $B_N(k)$ is equal to zero. In this case, Z(k) is chi-squared of order one. It is well known that the mean and variance of a chi-squared random variable are given by

$$E[\chi_n^2] = n$$

and (3.40)

$$Var[\chi_n^2] = 2n$$

where n is the order of the chi-squared random variable. Substituting Equations 3.29 and 3.38 into 3.39 yields

$$\tilde{S}(k) = \frac{T_s \, Var[A(k)] \, Z(k)}{L} . \tag{3.41}$$

With the aid of Equation 3.40 and 3.34, the mean of $\tilde{S}(k)$ is

$$E[\tilde{S}(k)] = \frac{T_s}{L} Var[A(k)] \, E[Z(k)]$$

$$= T_s \sigma_x^2 \quad . \tag{3.42}$$

But this is nothing more than S(k), the discrete spectral density function of a white noise process. Therefore

$$E[\tilde{S}(k)] = S(k) \quad \text{for } k = 0 \text{ and } L/2. \tag{3.43}$$

The variance of $\tilde{S}(k)$ is computed from Equation 3.41 in a similar manner

$$\text{Var}[\tilde{S}(k)] = \frac{T_s^2 \, \text{Var}^2[A(k)] \, \text{Var}[Z(k)]}{L^2}$$

$$= 2 \sigma_x^4 T_s^2$$

$$= 2 S^2(k) \; ; \; k = 0 \text{ and } L/2. \tag{3.44}$$

For $k \neq 0$ or L/2, B(k) is not zero and therefore Z(k) is distributed as χ_2^2. Combined with the fact that Var[A(k)] = Var[B(k)] for this range of k, substitution of Equations 3.29, 3.34 and 3.38 into 3.39 again results in Equation 3.41. Again invoking the properties of chi-squared random variables (Eq. 3.40), we obtain the mean of $\tilde{S}(k)$

$$E[\tilde{S}(k)] = \frac{T_s}{L} \text{Var}[A(k)] \, E[Z(k)]$$

$$= \left(\frac{T_s}{L}\right)\left(\frac{L\sigma_x^2}{2}\right)(2)$$

$$= \sigma_x^2 T_s$$

$$= S(k);\ k = 0,\ldots,L/2-1 \text{ and } L/2+1,\ldots,L-1; \tag{3.45}$$

and the variance of $\tilde{S}(k)$

$$\begin{aligned} \mathrm{Var}[\tilde{S}(k)] &= \frac{T_s^2}{L^2}\,\mathrm{Var}^2[A(k)]\,\mathrm{Var}[Z(k)] \\ &= \frac{T_s^2}{L^2}\quad\frac{L^2\,\sigma_x^4}{4} \quad (4) \\ &= \sigma_x^4\,T_s^2 \end{aligned}$$

$$= S^2(k)\ ;\quad \begin{matrix} k = 0,\ldots,L/2-1 \\ \text{and} \\ L/2+1,\ldots,L-1. \end{matrix} \tag{3.46}$$

At this point, a summary of all that has been observed is in order. First, it has been shown that, for a given k, the spectral estimator, $\tilde{S}(k)$ is a random variable with mean S(k) and variance proportional to $S^2(k)$. Therefore the mean of the estimator is the actual spectrum as it should be. Unfortunately, the variance of the estimator is proportional to the square of the parameter to be estimated. A desirable characteristic of estimators is the asymptotic decrease in the variance as the sample size L increases. Obviously this is not the case here as the variance is totally independent of the sample size; estimators of this nature are deemed inconsistent. This problem will be addressed later when methods of reducing the variance are investigated. Second, certain assumptions were made which must be

considered for practical applications: a) A(k) and B(k) are gaussian random variables; b) the estimated noise process is "white"; and c) L, the number of data points available, and M, the order of the discrete Fourier transform are equal. Assumption a) is quite reasonable as long as the number of data points is sufficiently large as is the case in the fine structure experiment. Assumption b) was required to obtain simple mathematical expressions, however the extension to a monotonically decreasing noise spectrum is heuristically satisfying. The final assumption is valid since, in practice, the number of data points, L, is increased to M by attaching M-L zeros. This technique of zero-padding assures that the number of apparent data points equals the order of the discrete Fourier transform.

3.2.4 Windows.

Throughout the previous discussion, the finite extent of the available data samples has inevitably led to compromises in the computation of the spectral estimate. The most significant of these is spectral leakage which is easily understood with the concept of windows.

In the example of Section 3.2.1, a heuristic explanation was given for the distortion introduced into the Fourier transform by the truncation of the given data sample. A useful means of evaluating this distortion mechanism becomes evident with the following observation. Assuming a set of data samples, x(n),

$$\sum_{n=0}^{L-1} x(n)e^{-j\frac{2\pi}{M}nk} = \sum_{n=-\infty}^{\infty} w(n)x(n)e^{-j\frac{2\pi}{M}nk} \qquad (3.47)$$

where $w(n) = \begin{cases} 1 & \text{for } n = 0,1,\ldots,L-1, \\ 0 & \text{for all other } n \end{cases}$

and x(n) is defined for all n.

From Equation 3.47, we see that the discrete Fourier transform may be expressed in the form of the infinite extent discrete Fourier transform with a modified set of data samples. The modified data have the form

$$\bar{x}(n) = w(n)x(n) \tag{3.48}$$

where x(n) and w(n) are defined as in 3.47. The effect of this weighting function may be studied more easily in the frequency domain. Taking the Fourier transform of Equation 3.48 yields

$$\bar{X}(k) = W(k) * X(k) \tag{3.49}$$

where the '*' operator denotes convolution. Substituting this into the expression for the spectral estimator (3.22) we obtain

$$\begin{aligned} \tilde{S}(k) &= \frac{T_s}{L} \left| W(k) * X(k) \right|^2 \\ &= \frac{T_s}{L} \left[\left| W(k) \right|^2 * \left| X(k) \right|^2 \right] . \end{aligned} \tag{3.50}$$

Here we see that the spectral estimate is actually the spectrum of

the original data samples convolved with the spectrum of the window w(n). From this knowledge, the distortion introduced into the spectral estimate may be predicted by studying the properties of the spectrum of the window w(n).

In the calculation of the DFT, it has been shown that an "implied" window is inherently applied to the data sample x(n). The window w(n) defined in 3.47 and commonly referred to as the rectangle or box function has a spectrum of the form

$$|W(k)|^2 = \frac{\sin^2(\frac{kL}{2})}{\sin^2(\frac{k}{2})} \tag{3.51}$$

which is shown in Figure 3.2. Since this function is convolved with the actual spectrum to obtain the desired spectrum, we see that the estimate at a particular frequency is the weighted sum of all frequencies present in the actual spectrum! This leakage of adjacent frequencies into the frequency of interest is called spectral leakage and is responsible for the bias in the spectral estimate. This phenomenon is easily understood with the aid of an example. Suppose the data samples consist of a sampling of a sinusoid of frequency ω_o. The one-sided spectrum of a sinusoid existing for all values of time is a delta function located at frequency ω_o. Computation of the DFT on a finite sample of the sinusoid results in a spectrum consisting of the convolution of the delta function with W(k) (see Figure 3.3). The spectral estimate therefore has nonzero values for frequencies not equal to ω_o; the sinusoid at ω_o has leaked into other frequencies. This leakage can also be explained

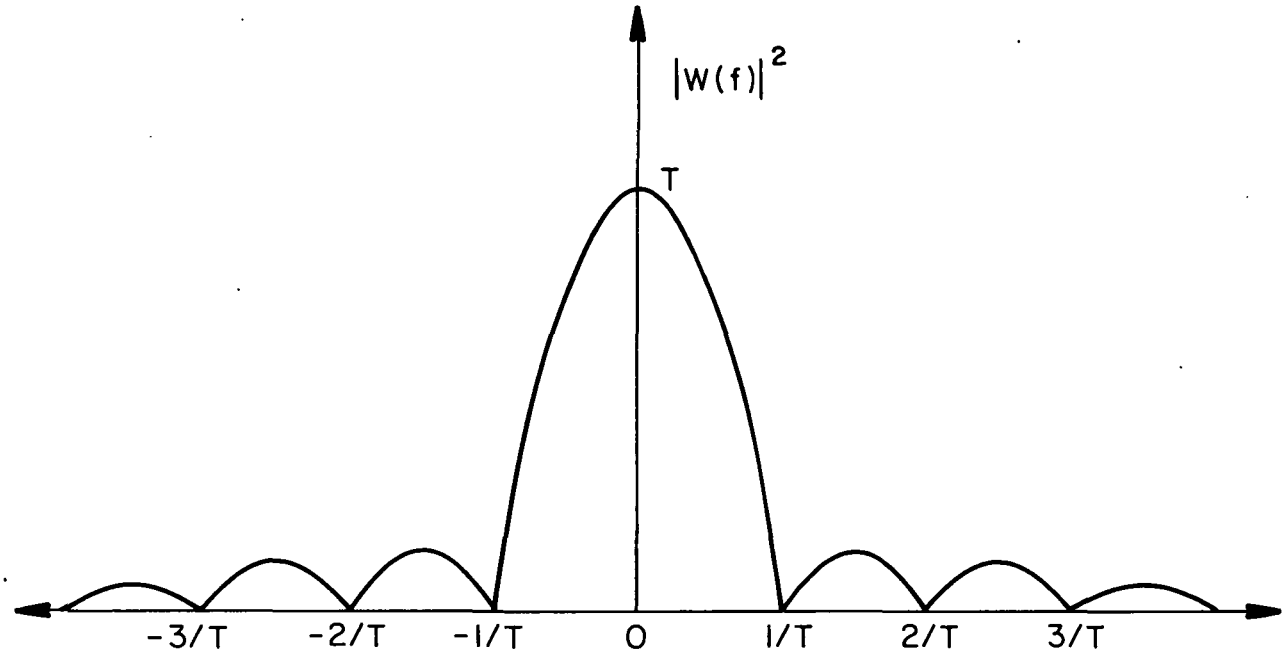

Figure 3.2. Spectral representation of the rectangular window function.

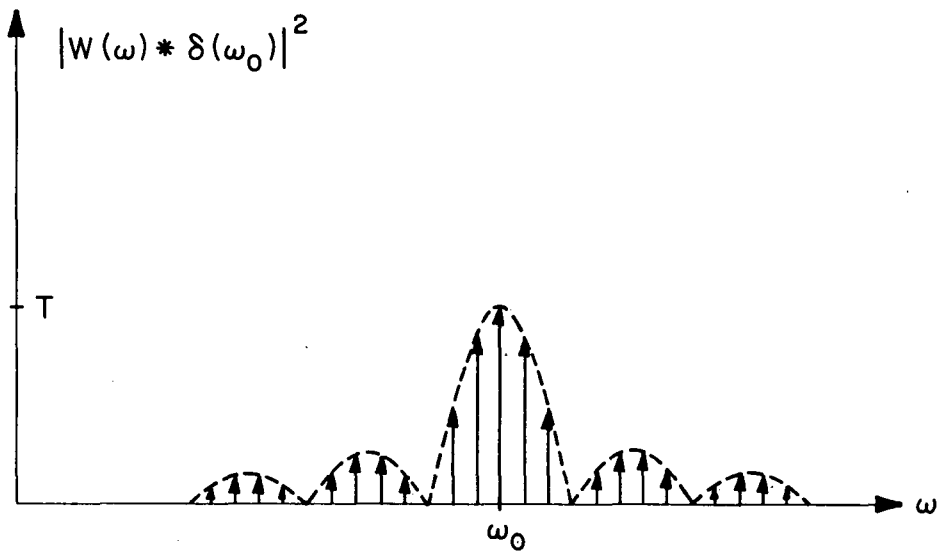

Figure 3.3. Computation of the DFT on a sinusoid of finite extent.

by taking a look at what happens in the time domain. Figure 3.4 shows a sinusoid that has been arbitrarily truncated by the data window w(n). Remembering that computation of the DFT on a finite data sample is equivalent to performing the infinite-extent Fourier transform on a periodic extension of x(n), we see that a discontinuity exists between segments. The discontinuities contribute to frequency components other than ω_0 and therefore leakage has occurred.

It is advantageous to control spectral leakage by judicious choice of the data window w(n). At first glance, any reduction in the discontinuity would improve on leakage therefore most data windows used today transition smoothly to zero at the boundaries, thereby forcing continuity between segments of the periodic extension. However as in all engineering problems, this reduction of discontinuities does not come free. In order to understand the tradeoffs involved in window design it is necessary to discuss some relevant parameters of windows.

Obviously, the ideal window would be represented in the frquency domain by a delta function. Convolution with the actual spectrum would thereby reproduce the actual spectrum. For this reason, window design in the frequency domain is focused around two objectives: 1) to minimize the main lobe width, and 2) to minimize the sidelobe levels relative to the main lobe. Unfortunately, these are conflicting requirements and therefore must be traded off with one another depending on the specific application. If one chooses to allow large sidelobes for the sake of a narrow main lobe, spectral leakage will occur to a degree proportional to the relative sidelobe level. On the other hand,

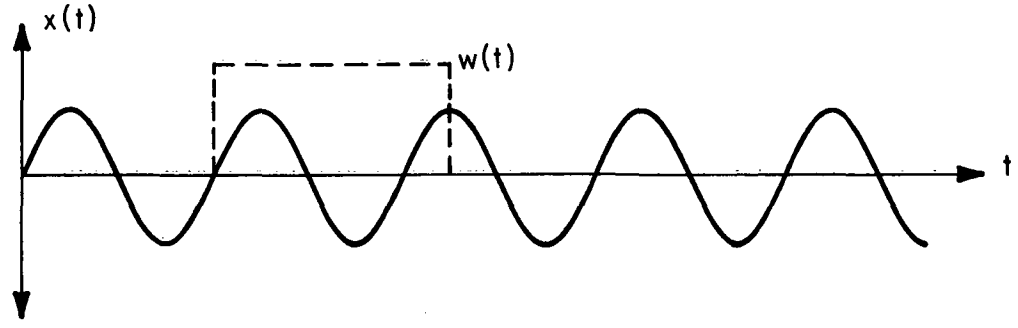

a)

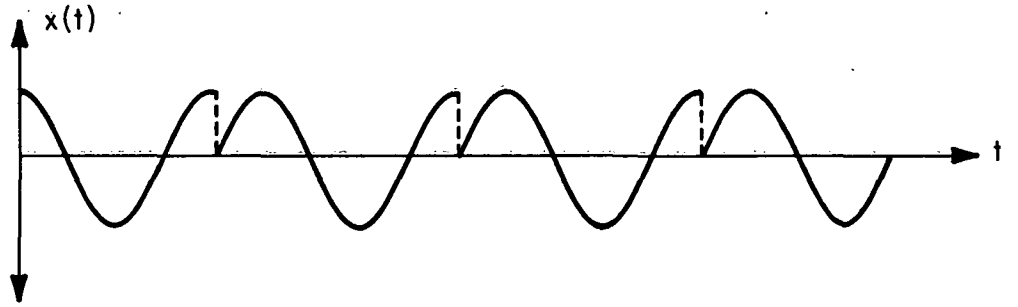

b)

Figure 3.4. Time domain perspective of DFT computation on a sinusoid arbitrarily truncated by a rectangular window.

lower sidelobes and a wide main lobe reduce spectral leakage but also reduce the ability to resolve between two closely spaced frequencies. HARRIS [1978] provides a detailed explanation of the many available window designs along with their associated tradeoffs.

Two other important window parameters have to do with spectral scaling. Suppose x(n) is a white noise process with variance (total power) σ_x^2 and a window w(n) is applied to the L samples of x(n). Following the analysis in Section 3.2.2, the effects of a window on the mean of the spectral estimate may be determined by first computing the autocorrelation function of $\overline{X}(k)$, the discrete Fourier transform of the modified data sample, w(n)x(n).

$$R_{\overline{X}}(k,1) = E\left[\overline{X}(k)\,\hat{\overline{X}}(1)\right]$$

$$= E\left\{\sum_{n=0}^{L-1} w(n)\,x(n)\,e^{\frac{-j2\pi kn}{M}} \sum_{m=0}^{L-1} w(m)\,x(m)\,e^{\frac{j2\pi 1m}{M}}\right\}$$

$$= \sum_{n=0}^{L-1}\sum_{m=0}^{L-1} w(n)\,w(m)\,\sigma_x^2\,\delta(n-m)e^{\frac{-j2\pi kn}{M}}\,e^{\frac{j2\pi 1m}{M}}$$

$$= \sigma_x^2 \sum_{n=0}^{L-1} w^2(n)e^{\frac{-j2\pi n(k-1)}{M}}$$

$$R_{\bar{X}}(k) = \sigma_x^2 \sum_{n=0}^{L-1} w^2(n)\, e^{\frac{-j2\pi kn}{M}} \quad . \tag{3.52}$$

The mean of the "windowed" spectral estimate is then given by

$$E\,[\tilde{S}(k)] = \frac{T_s}{L} E\left[|X(k)|^2\right] = \frac{T_s}{L} R_X(0)$$

$$= T_s \sigma_x^2 \left[\frac{\sum_{n=0}^{L-1} w^2(n)}{L}\right] . \tag{3.53}$$

It is evident that the mean of the spectral estimate has been biased by the term in parentheses which is the sum of the squared window terms normalized to the window length L. This term is referred to as the incoherent power gain (IPG). For a rectangular window, IPG = 1 as it should since the spectral estimate computed in Section 3.2.2 took into account this "implied" data window.

Finally, a window's effect on a sinusoid or the coherent power gain (CPG) will be addressed. Given a sinusoid of the form $x(n) = A \cos(2\pi fnT_s)$; $n=0,1,\ldots,L-1$ and following the same calculations as in Section 3.2.2, the spectral estimate is

$$\tilde{S}(k) = \frac{T_s}{L} |X(k) * W(k)|^2$$

$$= \frac{T_s}{L} \left|\frac{LA}{2} \delta(k-s) * W(k)\right|^2 \tag{3.54}$$

where s is the normalized discrete frequency corresponding to f (i.e., s is one point in the set of k = 0,1,...,M-1).

$$\tilde{S}(k) = \frac{T_s}{L} \cdot \frac{L^2A^2}{4} \cdot \left|W(k-s)\right|^2$$

$$\tilde{S}(s) = T_sL(A^2/4)\ \left|W(o)\right|^2$$

$$= T_sL \left[\sum_{n=0}^{L-1} w(n)\right]^2 \left[\frac{A^2}{4}\right]. \qquad (3.55)$$

Since $(A^2/4)$ is the spectral magnitude for the positive frequency component of a sinusoid of amplitude A, the coherent power gain is

$$CPG = T_sL \left[\sum_{n=0}^{L-1} w(n)\right]^2 . \qquad (3.56)$$

Because the spectrum of electron density irregularities is noise-like, the IPG is of primary importance concerning spectral scaling due to the use of windows. Therefore, this factor is accounted for in the spectral computations.

3.2.5 Variance reduction.

In Section 3.2.3, the spectral estimator $\tilde{S}(k)$ was determined to be a random variable with a mean equal to the actual spectrum S(k) and a variance proportional to $S^2(k)$. Obviously the large variance of the estimator is undesirable; so the question arises as to how it may be

reduced. WELCH [1967] has suggested a method based on averaging modified spectral estimates.

This method is implemented by dividing a data segment of N samples into K segments of L samples each. The spectral estimates $\tilde{S}_i(k)$ are then computed for each segment respectively and averaged to derive the overall estimate

$$\tilde{S}(k) = \frac{1}{K} \sum_{i=1}^{K} \tilde{S}_i(k); \quad k=0,\ldots,M-1 \ . \tag{3.57}$$

The computation of each spectral estimate $\tilde{S}_i(k)$ is performed according to the methods mentioned previously; namely a window is applied to the data segment of length L and the estimate is computed using Equation 3.22.

If the K segments are non-overlapping, then the estimates $\tilde{S}_i(k)$ are independent random variables which are identically distributed. The mean and variance of a random variable created by summing K independent, identically distributed random variables are related to the mean and variance of the individual random variables as follows:

$$E\,[S(k)] = E\left[\frac{1}{K} \sum_{i=1}^{K} \tilde{S}_i(k)\right] = E\,[\tilde{S}_i(k)] \tag{3.58}$$

and

$$\text{Var}\,[\tilde{S}(k)] = \text{Var}\left[\frac{1}{K} \sum_{i=1}^{K} \tilde{S}_i(k)\right] = \frac{1}{K}\,\text{Var}\,[\tilde{S}_i(k)] \ . \tag{3.59}$$

Therefore, by segmenting the N samples, we have reduced the variance of the estimate by a factor of 1/K without introducing any bias.

Unfortunately, the reduction in variance comes at the expense of spectral resolution. It has been shown earlier that the spectral resolution of the estimate depends on the length of the data segment and the type of window used in the computation. By segmenting the data, the computational length has been reduced from N to L which corresponds to a widening of the spectral window in the frequency domain. Thus, the averaged estimate is the result of a convolution of the actual spectrum with a broader spectral window which results in a loss of spectral resolution.

To optimize the tradeoff, we wish to choose a value of L and therefore K that reduces the variance to an acceptable level while maintaining the required resolution bandwidth. Both of these requirements may be eased a little by overlapping the data segments. For a given L, the number of segments used in the average could be increased and vice versa. However, estimates computed from overlapping segments result in random variables which are no longer independent. The actual reduction in the variance diminishes as the correlation between overlapped segments increases. WELCH [1967] and KAY AND MARPLE [1981] have shown that the variance of the averaged estimate assuming a Gaussian white noise process is

$$\text{Var}\left[\tilde{S}(k)\right] = \frac{\text{Var}\left[\tilde{S}_i(k)\right]}{K}\left[1 + 2\sum_{r=1}^{K-1}\frac{K-r}{K}\,c(r)\right], \qquad (3.60)$$

where c(r) is the correlation coefficient and r is the number of overlapping data samples. c(r) is given by

$$c(r) = \frac{\left[\sum_{n=0}^{rL-1} w(n)\, w(n+(1-r)L)\right]^2}{\left[\sum_{n=0}^{L-1} w^2(n)\right]^2} . \qquad (3.61)$$

For a given segment length L determined by the required spectral resolution, the number of segments K may be increased by providing more overlap between the segments. At what point however, does the increasing correlation begin to seriously degrade the variance reduction? KAY AND MARPLE [1981] have shown that for most "good" windows, fifty percent overlap results in essentially independent segment estimates.

3.2.6 Stationarity.

The final issue to be addressed concerning spectral estimation of fine structure data is the stationarity of the measured time series. The estimation techniques described up to now are based on the assumption that the data are statistically stationary (i.e., the mean and autocorrelation functions are independent of time). If these parameters vary with time, the spectral estimate will be far from an accurate representation of the actual spectrum. To our dismay, the spectrum does

indeed change with time as the frequency distribution of the electron density irregularities changes. How do we obtain a reliable estimate?

The same problem is encountered in the spectral estimation of speech, another inherently nonstationary random process. The solution is to choose a time interval over which the data may reasonably be assumed to be stationary. In other words, the spectrum changes over some finite time interval; therefore we choose a smaller time interval over which to perform the analysis. The key is then to determine the rate at which the spectrum changes.

The proposed method to test the fine structure data for stationarity is built in Welch's technique of averaging spectral estimates. To begin, a data sequence of length N is chosen and assumed to be stationary. The sample is then divided into K segments of L samples, each according to variance and spectral resolution requirements. The K spectral estimates are computed and may be compared to one another prior to averaging to determine whether or not the spectrum is changing over the chosen time interval of N data points.

Considering the large variance of the individual estimates, it may be difficult to discern any variations in the spectrum. This may be alleviated by performing a linear fit to the computed spectra (on a logarithmic scale) and comparing spectral indices.

3.3 Software Implementation

The electron-density irregularities are analyzed using program SPECTRA, a FORTRAN alogrithm which computes the spectral density of the

irregularities (see Appendix). A flowchart of program SPECTRA is shown in Figure 3.5.

The main program is the center of control which allows user-interaction and accesses the subroutines (shown in rectangular boxes with quotations) subject to the operator's wishes. Details concerning the experiment and analysis are entered here in two ways. First are the experiment parameters (see Appendix) such as the total experiment gain; tape channel number; discriminator-digitizer calibrations; the upper frequency 3 dB points of the logarithmic electrometer, amplifiers and telemetry channel; and the number of the broadband amplifier output being analyzed. In addition to those parameters describing the experiment are several which detail the plotting parameters which are unlikely to be changed during the analysis. All experiment parameters are manually entered directly into the software and cannot be modified during program execution.

Secondly, parameters detailing the analysis of the data are interactively entered by the user during program execution. These include the launch time; starting time of the data to be analyzed; the number of data samples to be analyzed; the number of segments used to partition the data; the individual segment lengths; the type of data window; the FFT block length; the type of plot, if any; plotting of individual peridograms and an optional least-squares line fitting to the spectra. The operator is given the option to change any of these parameters prior to execution of the subroutines and immediately following.

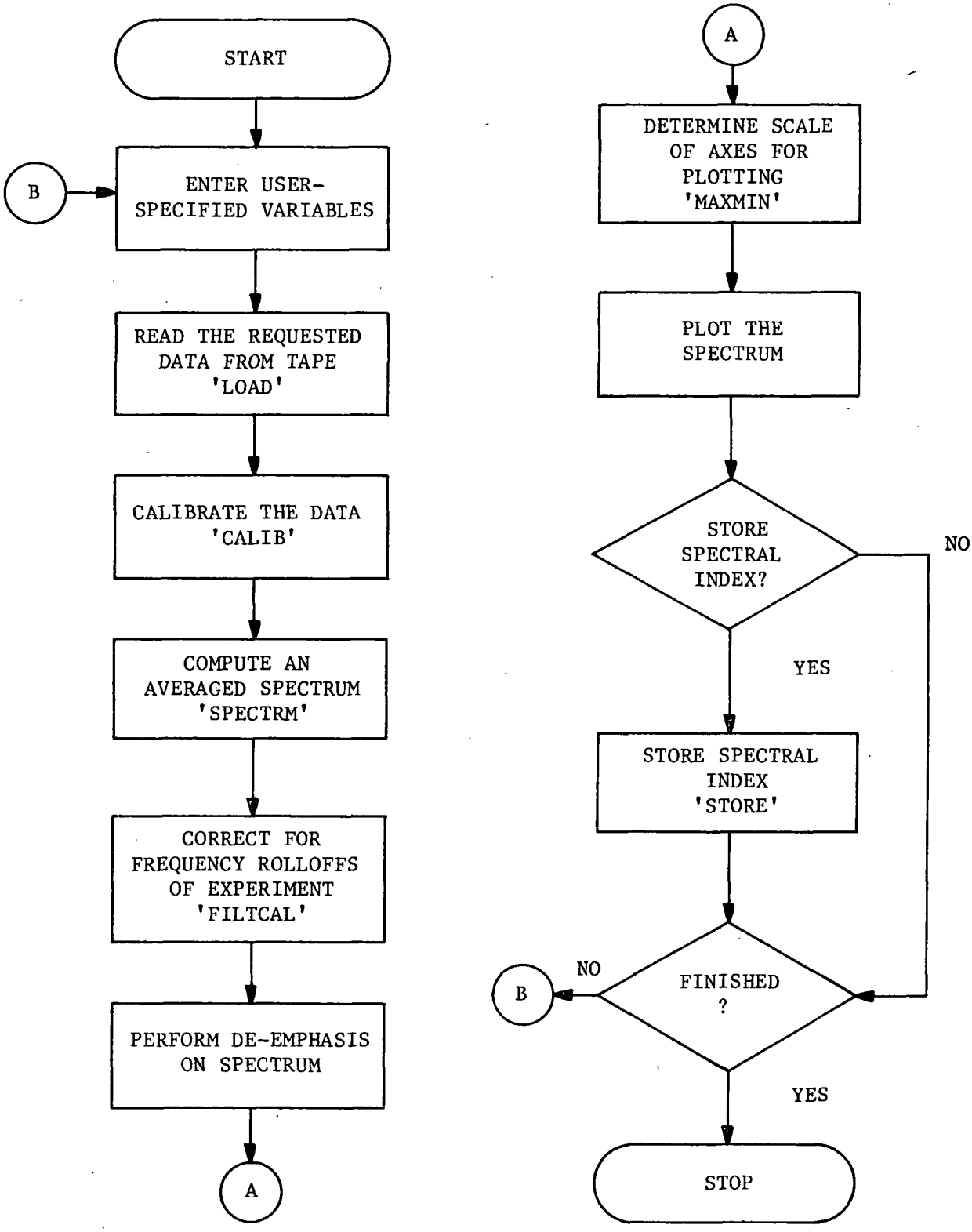

Figure 3.5. Flowchart of program SPECTRA.

Following the interactive portion, the main program calls subroutine LOAD which retrieves the data as specified by the operator. This routine is tailored specifically for use with a magnetic tape formatted for a Control Data Corporation Cyber 175 computer and therefore must be modified for use with another computer system incompatible with the Cyber 175. LOAD reads the number of data samples requested, starting with the first sample after the desired time from launch and stores them in an array for future processing. LOAD also determines the sampling rate of the digitized data by reading the time code stored on the tape.

Subroutine CALIB performs the necessary calibrations to the data array so that the samples resemble the output of the fine structure experiment (namely the output of the AC amplifier in the case of the Energy Budget Campaign and the broadband amplifiers in the case of Project Condor). First the data are corrected for nonlinearities in the discriminator which is used to demodulate the FM signal on the original analog tape, and are reduced by the inherent gain in the digitizer. The discriminator and digitizer combination are calibrated prior to digitization of the analog tape by injecting known signals into the discriminator and monitoring the output of the digitizer. These values are stored in an array BANDCAL which is entered manually under experiment parameters in the main program. A piecewise linear fit to these values then serves as the calibration curve correcting for digitizer gain and discriminator nonlinearities.

Secondly, the data are reduced by the gain of the experiment itself so it is representative not of the output signal of the experiment but of the actual value of $\Delta N/N$ sensed by the probe.

Subroutine SPECTRM performs the heart of the analysis and is shown in Figure 3.6. After initializing all variables and arrays, the subroutine reads a specified data segment from the data array and immediately computes and subtracts the mean from the segment samples. This prevents large dc components from arising in the spectrum which might contaminate it. Next the data are weighted with a window function by subroutine WINDOW. Presently, six weighting functions are available in WINDOW: rectangular, Bartlett, Hanning, Hamming, Blackman and Blackman-Harris (4-term) windows. The subroutine may easily be modified to include other window functions also. The details of the application and effects of the window functions are described in Section 3.2.4.

A periodogram (or spectral estimate) is computed from the data segment using the estimator described in Section 3.2.2. Implementation of the FFT is accomplished via an algorithm (FFTRC) from a software library provided by IMSL, Inc. Since this algorithm only computes the Fourier coefficients for positive frequencies, all are multiplied by a factor of two so that the resulting spectrum represents the total power in the irregularities.

At this point, a running average of the periodograms is computed as described in Section 3.2.5. Plotting of the individual periodograms may then be performed or bypassed according to the operator's wishes. If individual periodogram plotting is desired, subroutines FILTCAL, DEEMPH,

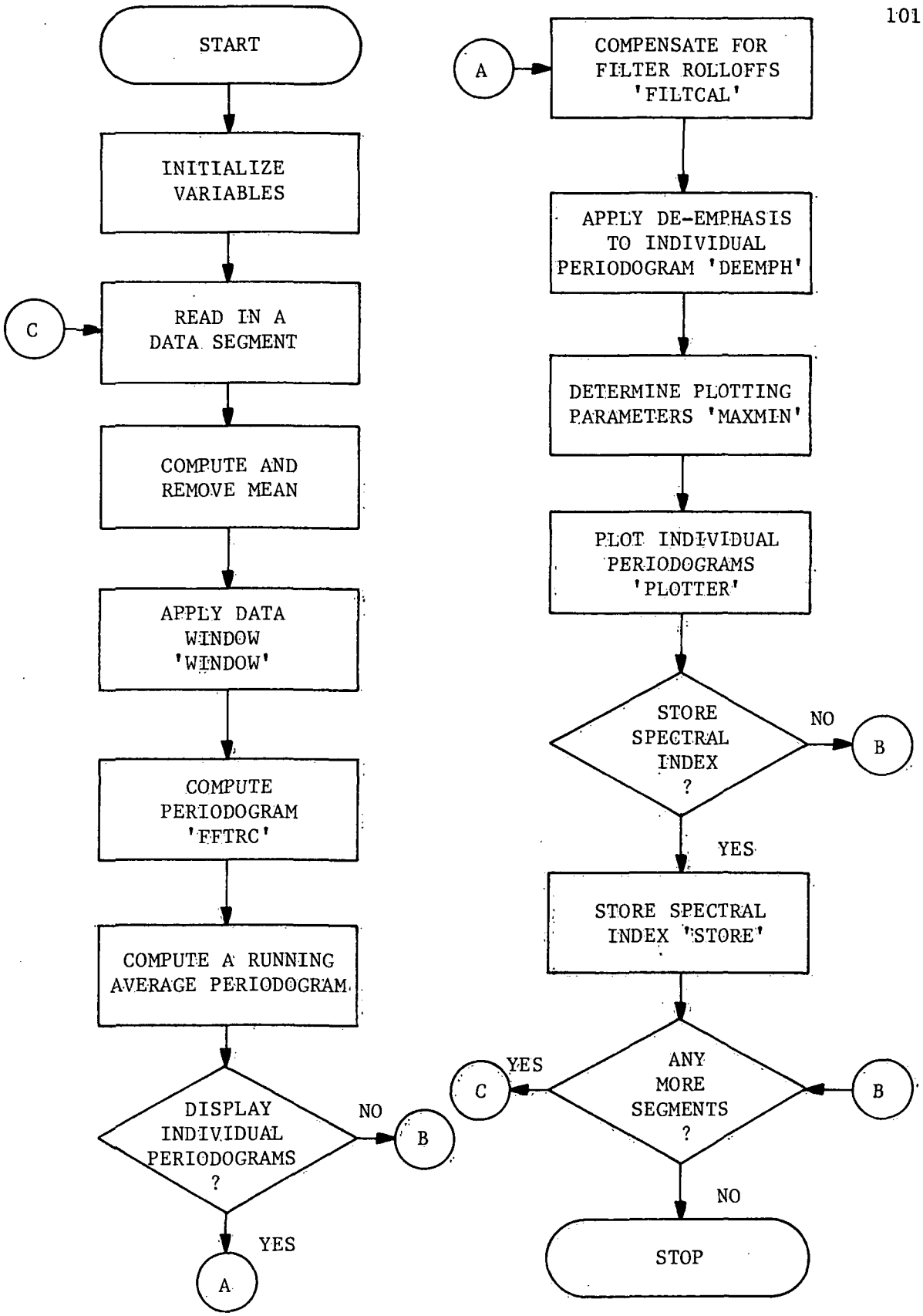

Figure 3.6. Flowchart of subroutine SPECTRM.

MAXMIN, PLOTTER and STORE are accessed by subroutine SPECTRM. These subroutines will be described later as they are used by the main program. If individual periodogram plotting is bypassed, these subroutines are not accessed. In either case, spectral estimates are computed sequentially for all data segments and the running average is returned to the main program at the end of SPECTRM execution.

The main program then calls subroutine FILTCAL which corrects the averaged spectrum for the upper frequency rolloff of the logarithmic electrometer, telemetry filter and the AC amplifier (or broadband amplifiers). The telemetry filter is modelled as an ideal three-pole low-pass filter [ZIMMERMAN and SMITH, 1980]. The logarithmic electrometer is modelled as a single-pole low-pass filter as is the ac amplifier (or broadband amplifiers).

For data derived from Project Condor, de-emphasis of the spectrum is accomplished with subroutine DEEMPH. The de-emphasis filter is modelled as the inverse of a single-pole high pass filter with the characteristics shown in Fig. 2.16 for the particular broadband amplifier output being analyzed. If de-emphasis is not required such as the case of the Energy Budget Campaign, DEEMPH may be bypassed by setting the variable BBAND = 0 in the experiment parameters section of the main program.

Subroutine MAXMIN determines the scale of the plotting axes by determining the maximum values of the spectral magnitude and frequency. In the case of logarithmic plotting, MAXMIN calls subroutine LIMITS which rounds the maximum values to the next largest power of ten.

Subroutine PLOTTER allows plotting of the spectrum in linear or logarithmic coordinates along with the capability of least-squares line fitting in logarithmic coordinates to determine spectral indices. A flowchart of PLOTTER is shown in Figure 3.7. This subroutine requires the Graphics Compatibility System software library for the Control Data Corporation Cyber 175 series and must be modified for use with another graphics software package.

Subroutine STORE allows the option to store the spectral indices of spectra in the following format: average time of the data segment, the spectral index, the spectral magnitude.

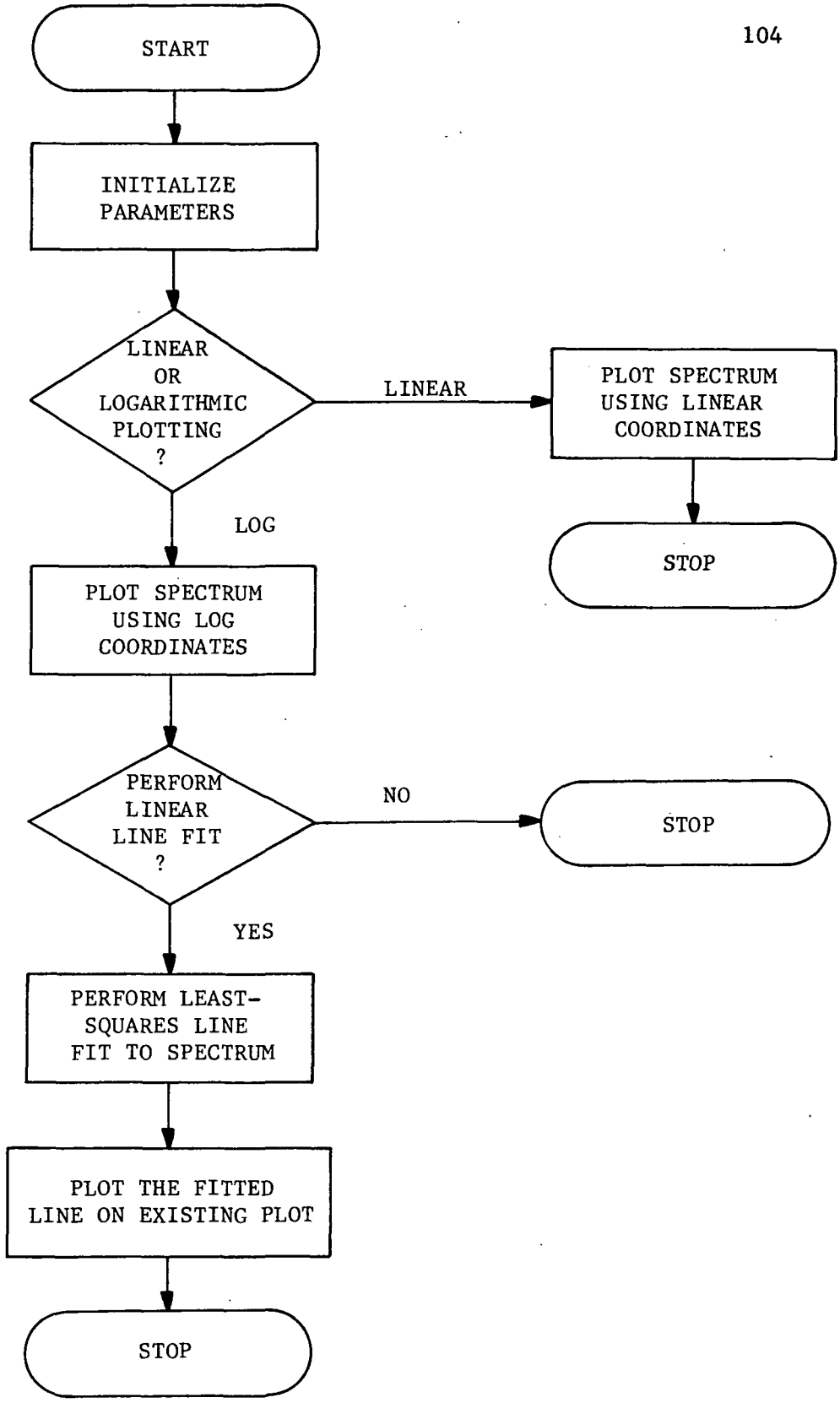

Figure 3.7. Flowchart of subroutine PLOTTER.

4. PRELIMINARY RESULTS FROM THE ENERGY BUDGET CAMPAIGN

The Energy Budget Campaign of November and December of 1980 included the launch of three Taurus Orion rockets from Kiruna, Sweden into the night time auroral ionosphere. The geographic coordinates of the launch site are 67.9° N, 21.1° E. The rockets carried probes for measuring electron density irregularities in the D and E regions of the ionosphere. High quality data were obtained from only one rocket, Taurus Orion 33.011. The results from a preliminary analysis follow.

4.1 Data Processing

The FM/FM telemetry signal from 33.011 contained the output of the fine-structure experiment on channel 20. The FM signal was recorded on analog tape and later digitized onto another tape at a rate of 5000 samples per second. With the useful bandwidth of the system bounded by the spin frequency harmonics on the lower end and the sampling theorem on the higher, the spectra of the irregularities are obtained over the frequency range from 4 Hz to 2.5 kHz. The spectra were computed with Program SPECTRA described in Section 3.3. An FFT was performed on sequences of 2048 consecutive data samples, representing an interval of 0.41 seconds. Windowing and spectral averaging were not used in the preliminary analysis. The rocket velocity in the upper mesosphere was about 1.3 km/s so the range of irregularity spatial wavelengths is 0.5 m to 300 m.

4.2 Observations

Strong fluctuations in electron concentration were observed at altitudes between 80 and 110 km. Between 78 and 80 km the signal appears to be below the noise level of the experiment. Spectra are shown in Figure 4.1 for the altitude range from 81 to 97 km. Above 89 km the spectra in the frequency range 50 Hz to 2 kHz show a slightly negative slope, as seen in the spectrum from 97 km, Figure 4.1(f). (The large spectral components at lower frequencies are due to the rocket spin frequency and its harmonics.) The irregularities above 89 km are due to a plasma instability mechanism and show characteristics previously observed at these altitudes both in the auroral zone and at the equator [THRANE AND GRANDAL, 1981; ROYRVIK AND SMITH, 1984].

At altitudes below 89 km, as shown in Figure 4.1(a) to (e), the spectra have a slope of -5/3 (the solid line) for low frequencies. Above some frequency, indicated by the vertical dashed line, the slope is steeper (about -3). The frequency at which the change of slope occurs decreases as the altitude increases. The conversion from frequency to wave number is made using the rocket velocity of 1.3 km/s. The amplitude of the irregularities at low frequencies (i.e., low wave numbers) is similar to that observed by THRANE AND GRANDAL [1981].

4.3 Discussion

The change in spectral index observed in the spectra of electron-concentration irregularities in the auroral mesosphere, from -5/3 at low wave numbers to about -3 at higher wave numbers, is similar to

ORIGINAL PAGE IS
OF POOR QUALITY

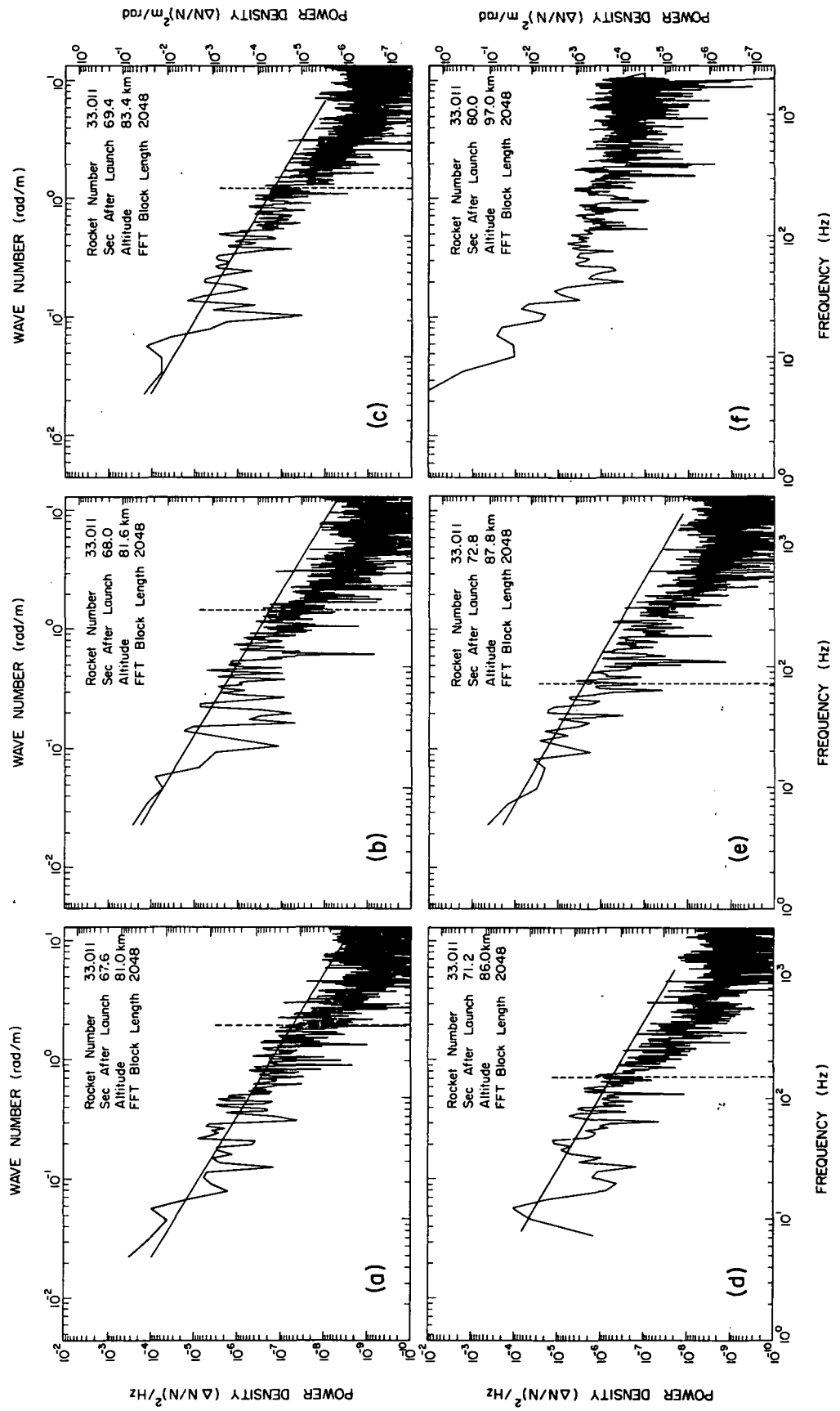

Figure 4.1. Spectra of electron density fine structure in the auroral ionosphere.

observations of irregularities in the equatorial mesosphere which were generated by neutral atmosphere turbulence [ROYRVIK AND SMITH, 1984]. There are, however, some important differences that must be considered.

We will consider the possibility that the change in the slope of the spectra represents the inner scale of three-dimensional turbulence [TATARSKII, 1971]. The wave number of the inner scale of turbulence, from the data of the previous section, is plotted in Figure 4.2 as a function of altitude. This figure also contains one point derived from probe observations at the geomagnetic equator during Project Condor launches and estimated limits of the inner scale based on Jicamarca radar observations. It can be seen that the inner scale of turbulence observed at high latitude is much larger than the upper limit estimated for the equatorial region.

Using the equation

$$\eta \tilde{\propto} (\gamma^3/\varepsilon)^{1/4} \qquad (4.1)$$

relating the inner scale of turbulence (η) to the energy dissipation rate (ε) and the kinematic viscosity (γ), we may consider the implications for γ and ε. If values for the kinematic viscosity are adopted from the US Standard Atmosphere 1976 we calculate that an energy dissipation rate of 8 W/kg is required to give the observed inner scale of turbulence at 81 km. This value of ε is larger, by at least an order of magnitude, than accepted values [RASTOGI AND BOWHILL, 1976]. Therefore it does not seem likely that the small inner scale of

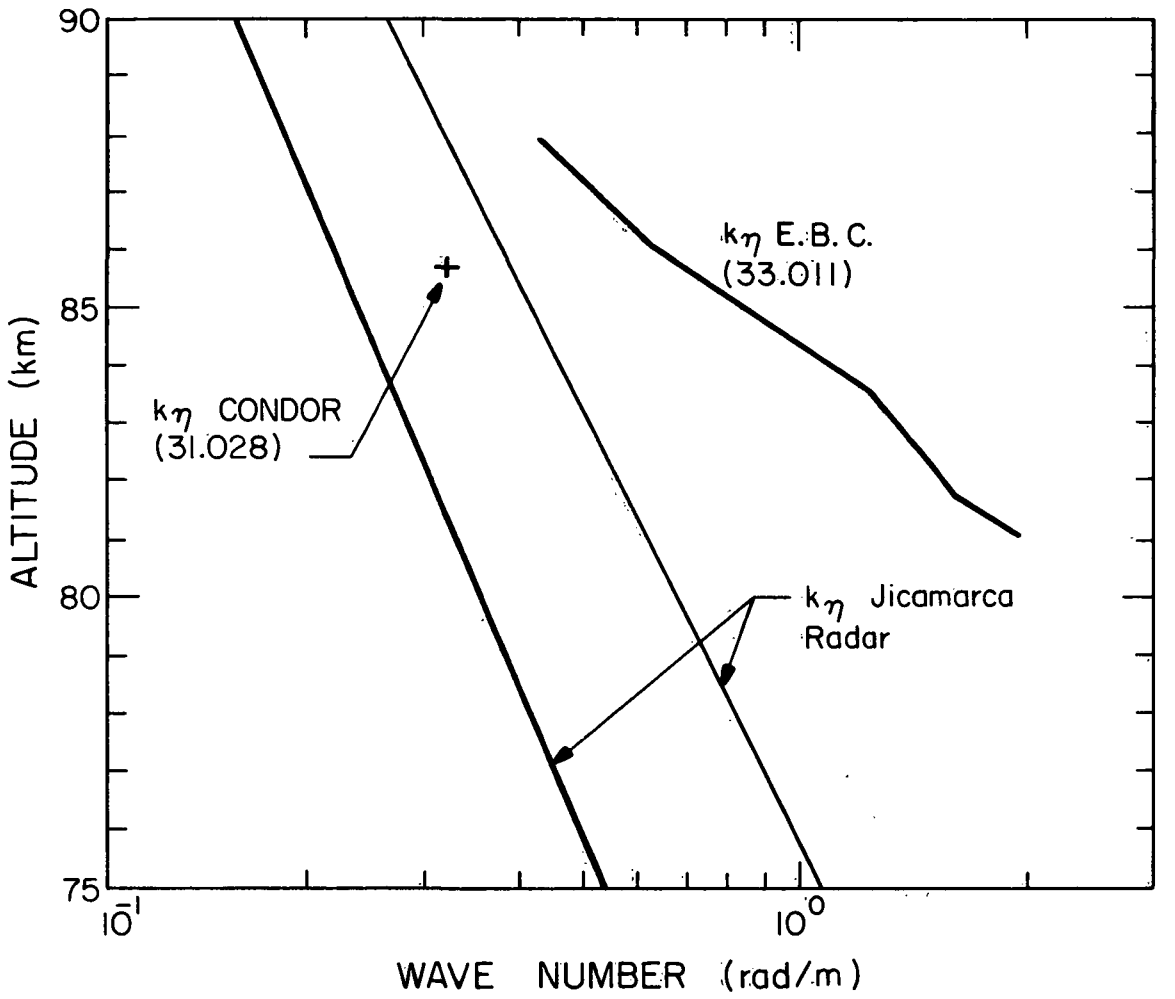

Figure 4.2. Wave number of the inner scale of turbulence versus altitude (ROYRVIK, unpublished).

turbulence observed in the auroral zone can be due only to a large energy dissipation rate.

The values of the kinematic viscosity given in the US Standard Atmosphere 1976 are calculated from a complicated formula involving the gas density and temperature. The right combination of decrease in temperature and increase in density might possibly account for the small inner scale; it requires at least a factor of two change from accepted values.

It is also possible that equations for calculating the inner scale of turbulence may be of limited accuracy at the altitudes considered here. The same equations have, however, yielded agreement with experimental results from the equatorial mesosphere.

An unexplained feature of these observations is the value of the spectral index at large wave numbers, possibly the dissipation subrange. The index here is about -3 although a previous experiment (at the equator) has shown a slope closer to -7 [ROYRVIK AND SMITH, 1984]. In addition, theoretical estimates predict an exponential decay (with wave number) of the irregularities in the dissipative subrange [TATARSKII, 1971].

It is interesting to note that a slope of about -3 has also been observed in velocity spectra from the stratosphere in the range of wavelength from 40 m to 2 km [DEWAN ET AL., 1984]. The wavelengths observed in the stratosphere are several orders of magnitude larger than reasonable estimates of the inner scale of turbulence (about 10 cm). They are also equal to, or larger than reasonable values for the outer

scale of isotropic turbulence (10 to 100 m) and thus are likely to be two-dimensional in nature. On the other hand, the range of wavelength (0.5 to 300 m) observed in the rocket experiments in the mesosphere, includes what is a reasonable estimate of the inner scale (about 10 m) at these altitudes. The range of wavelength over which the observed spectra have a slope of -3 must therefore coincide, in the mesospheric observations, with the dissipative range of turbulence. The observations presented here and those of DEWAN ET AL. [1984] represent different regimes present in the atmosphere and it is difficult to see how the similarity in spectral slope can be anything more than a coincidence.

ROYRVIK AND SMITH [1984] observed at the equator a single layer of irregularities approximately 1 km in vertical extent. The data have been interpreted to indicate that the layer resulted from mixing of the refractive index profile by shear-layer turbulence. In contrast with this equatorial observation, the data from the Energy Budget Campaign show a fairly broad region of irregularities of uniform amplitude from 80 km up to 89 km; above 89 km the turbulent irregularities are masked by the larger irregularities due to plasma instabilities in the electrojet. The broadness of this region indicates that the turbulence is not generated by a shear layer. It may be due to convective instabilities resulting from the breaking of gravity waves travelling upward in the mesosphere. BALSLEY ET AL. [1983] have, indeed, suggested that breaking gravity waves may be the dominant turbulent mechanism

contributing to radio-wave scattering at lower VHF frequencies in the high latitude winter-time mesosphere.

THRANE AND GRANDAL [1981] have reported data from an experiment carried on a rocket launched at night in the auroral zone during moderately disturbed conditions. They observed spectral indices of -5/3 for their range of sensitivity (2 to 100 m) in the altitude range from 65 to 95 km. They did not observe the inner scale of turbulence in their spectra of ion-concentration irregularities even though we would expect that, at 90 km, the value would be several tens of meters. On the basis of these data it may be necessary to consider the possibility, noted earlier, that mechanisms other than turbulence may sometimes contribute to the shape of the irregularity spectra. At altitudes above 95 km they observed an almost flat spectrum, as in our observations, and indicate a plasma instability as the generating mechanism.

5. PRELIMINARY RESULTS FROM PROJECT CONDOR

5.1 Introduction

Project Condor, conducted near Lima, Peru in February and March of 1983 included the simultaneous observation of electron density irregularities in the equatorial ionosphere using both rocket and radar experiments. The electrojet and spread F have been the major topics of other investigations (see, for example, the comprehensive review of ionospheric irregularities by FEJER AND KELLEY, 1980). The principal concerns here are the electron density irregularities in the mesosphere and in the upper E-region. Electrojet observations for which there are no simultaneous radar data (because of the limited number of range gates) are also presented.

Details of the two rocket launches are given in Table 5.1. The launch coordinates are: 12.50°S; 76.80°W. It is interesting to note that the flight of 27 February took place under geomagnetically quiet conditions (indicated by the Dst and Kp values), whereas that of 12 March had disturbed conditions. Though there are differences in the data from the two days, a connection with magnetic activity has not been established.

On the first day radar data were obtained from 1015 LST to 1155 LST, and include both mesopheric and upper E-region echoes. Mesospheric echoes were absent from the radar data of the second day, taken during the period 1203 to 1226 LST, although the upper E-region echoes were again observed. The radar data were taken at Jicamarca (11.95°S;

Table 5.1 Nike Orion rocket launches in Project Condor, 1983

Rocket number	31.028	31.029
Launch date	February 27	March 12
Launch time (UT)	1633	1709
Launch time (LST)	1133	1209
Apogee (km)	206.0	204.7
Apogee (s)	227.3	227.0
Apogee velocity (m/s)	232	244
Velocity azimuth (deg)	260	269
Spin rate (Hz)	7.3	6.9
Dst (nT)	14	-60
Kp	1	6
Solar zenith angle (deg)	12.3	9.4

76.87°W) with the beam pointed perpendicular to the magnetic field. The whole antenna was used for transmitting. The east and west quarter sections were used separately for receiving in an attempt to obtain drift velocities in the east-west direction. The radar experiment has been described in ROYRVIK AND SMITH [1984].

5.2 Data Processing

The probe data have been processed using both analog and digital methods. The analog form of presentation is used to show the intensity of the irregularities as a function of time. This allows rapid identification of features and altitude ranges of interest. Digital data processing is preferred when spectral characteristics are to be determined.

Analog processing consists of narrow-band filtering of the probe fine structure signal, followed by rectification (with low-pass filtering), so that the magnitude of $\Delta N/N$ is presented. This technique has been used, without rectification, by PRAKASH ET AL. [1972] and, with rectification, by SMITH AND KLAUS [1978].

The arrangement used here is shown in Figure 5.1. The fine structure signal from one or other of the broadband amplifiers appears at the output of the discriminator (which is provided with tape-speed compensation). Compensation for the low-frequency attenuation of the broadband amplifiers is applied using an op-amp circuit for which the voltage gain is 1 at high frequencies and 10 at low frequencies. The effect of the low-frequency compensation is to move the low frequency

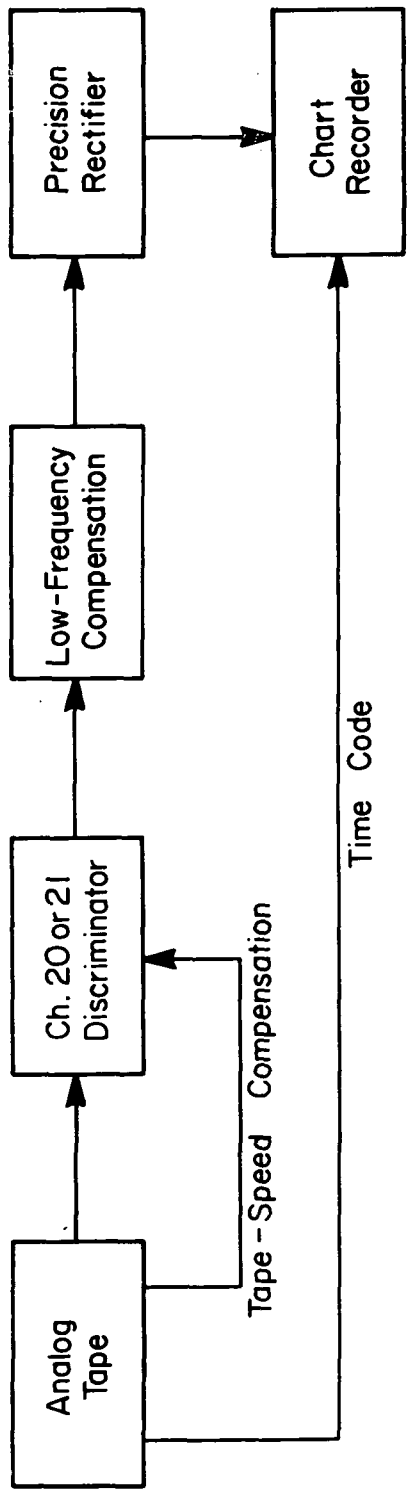

Figure 5.1. Block diagram of analog processing of fine structure data.

cutoff from 40 and 400 Hz to 4 and 40 Hz, respectively, in the two broadband amplifiers. The precision rectifier and two-channel chart recorder are identical to those used by SMITH AND KLAUS [1978]. The time code is also recorded on the chart.

Digital processing begins with digitization of the fine structure data. During the flight, the fine structure signal is stored on an analog tape as an FM signal. The recorded signal is then demodulated with an FM discriminator and digitized at a rate of 5000 samples/s. A reference sinusoid originally stored on the analog tape synchronizes the digitizer, thereby preventing tape speed fluctuations from contaminating the data.

The spectra are obtained using Program SPECTRA (see Section 3.3). A 2048-point FFT was performed on data samples from an interval of 0.41 seconds. Windowing and spectral averaging were not used in the preliminary analysis. De-emphasis of the fine structure signal is implemented in the software along with upper frequency cutoff compensation to correct for the rolloff of the logarithmic electrometer and the telemetry channel. The range of irregularity size is, for a rocket velocity of 1 km/s, 0.4 m (2.5 kHz) to 250 m (4 Hz).

5.3 Observations

The profiles of probe current (measured at constant voltage) for the two flights are shown, up to an altitude of 130 km, in Figure 5.2. The calibration factor, (electron density)/(probe current), is about 5 x 10^9 cm^{-3}/A. An accurate value, which may show some variation with

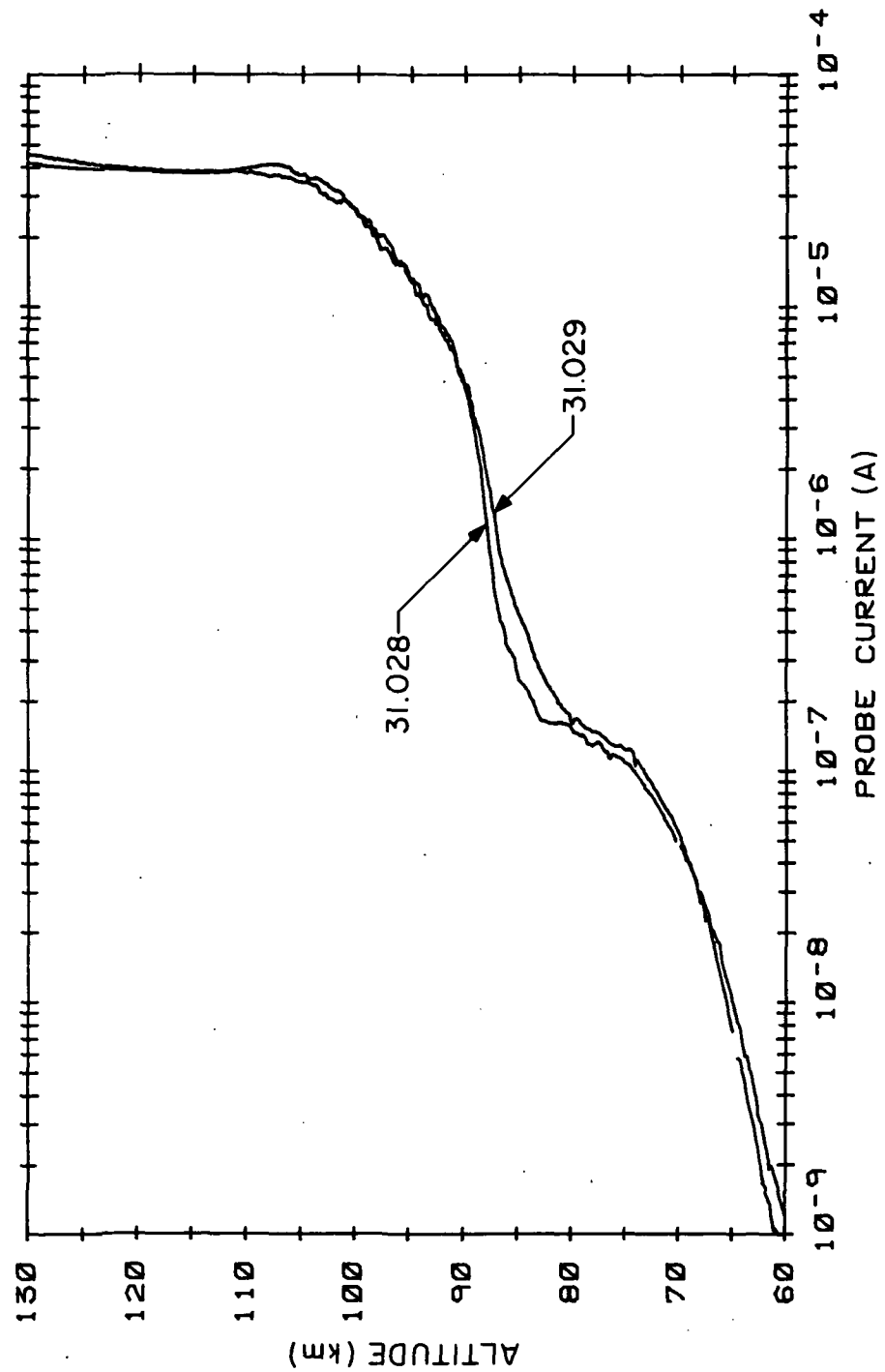

Figure 5.2. Profiles of probe current from Nike Orions 31.028 and 31.029.

altitude, will be established by the propagation experiments using the reflection heights of the ordinary and extraordinary waves in the upper E region, differential-phase measurements in the lower E region and differential-absorption measurements in the D region (see Section 2.3.4).

The main features of the profiles are similar to those obtained at midlatitudes: the D layer (up to about 82 km), the E layer (peaking at about 110 km), and a relatively constant electron density in the upper E region. Only in the altitude range from 80 to 88 km is there any substantial difference between the two profiles. The difference in solar zenith angles (see Table 5.1) is not sufficient to explain this.

The components of the probe current signal at the spin frequency (about 7 Hz) and its harmonics have been eliminated from the profiles of Figure 5.2 by averaging the measured current (digitized at 1 kHz) over a time interval equal to the spin period.

The burn-out of the two-stage Nike Orion rocket occurs at T + 41 s, which, for these flights is an altitude of 45 km. Except for the period from T + 19.5 s to T + 27 s, which is the in-flight calibration, the output of the probe experiment shows a high level of noise during the launch phase. The noise is attributed to vibration of the payload. It decreases after burnout, becoming insignificant at an altitude of about 80 km (T + 63 s). It is interesting to note that the spectrum of this noise has a spectral index which is close to the -5/3 power law that characterizes neutral atmospheric turbulence. We attribute this

signal to vibration of the payload by rocket-generated turbulence rather than to electron density irregularities of the ambient ionosphere.

The system noise in the probable absence of payload vibration and electron density irregularities is illustrated by the spectrum shown in Figure 5.3. This is at T + 66.7 s from Nike Orion 31.028 at an altitude of 87 km. The rocket has a total velocity of 1.51 km/s at this time and the flight elevation is 82.2 deg. The spin-related components of probe current (mentioned previously) appear at frequencies below 70 Hz. The lowest noise level, occurring near 600 Hz, shows a value of about 10^{-11} (in units of $(\Delta N/N)^2/Hz$).

The main features of the electron density irregularities of the daytime equatorial lower ionosphere are shown in Figure 5.4 which result from processing the data by the analog method (see KLAUS AND SMITH, 1978). Some of the spikes in the data, such as those near 81 km in both flights, appear to be artifacts of the instrumentation; they will be ignored. The features to note in Figure 5.4 are

(a) The layer of mesopheric irregularities near 85 km (only on 31.028);

(b) The Type 2 irregularities of the lower part of the electrojet, between 90 and 105 km;

(c) The Type 1 irregularities of the upper part of the electrojet, between 103 and 108 km (better developed on 31.029);

(d) A continuum of irregularities of small amplitude above 100 km.

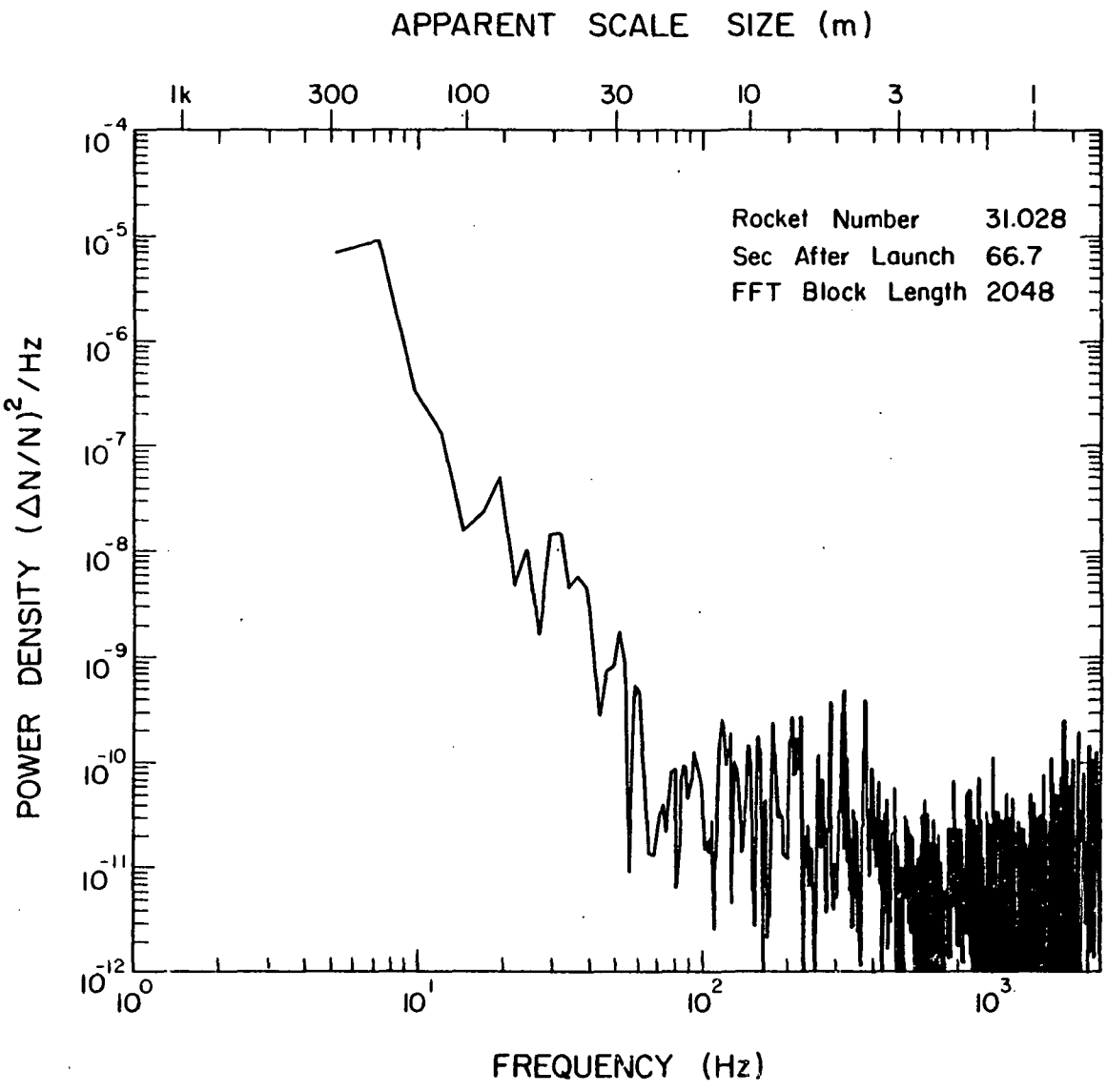

Figure 5.3. Spectrum of system noise from Nike Orion 31.028 at an altitude of 87 km.

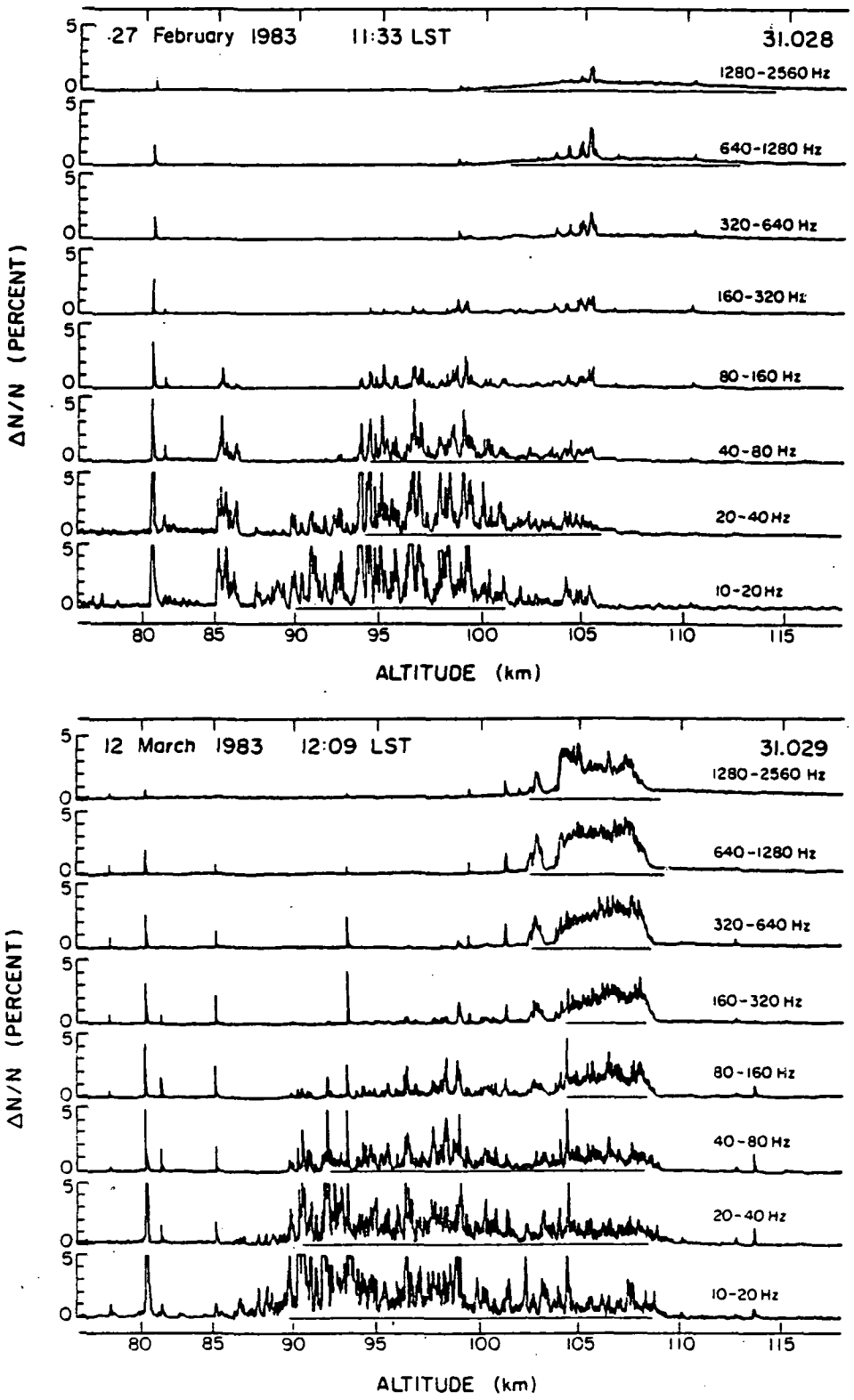

Figure 5.4. Irregularities in specific frequency bands as a function of altitude.

In the following sections we will discuss the characteristics of each of these four features and compare them with radar and other rocket observations.

5.4 Discussion

5.4.1 Mesospheric irregularities. At the time that the layer of mesospheric irregularities was observed on the rocket experiment (31.028) the radar at Jicamarca also recorded echoes, although at a slightly lower altitude (near 82 km). The radar data lead to a scattering cross section per unit volume of 2×10^{-18} m^{-1} [ROYRVIK AND SMITH, 1984].

The irregularity spectrum from the fine structure experiment is shown in Figure 5.5. The scales are expressed in rad/m rather than Hz, based on a rocket velocity of 1.52 km/s. (The scales are otherwise identical to those of other spectra included here.) Comparison with the noise spectrum of Figure 5.3 shows this to be a very strong signal.

Slopes corresponding to power laws of -5/3 and -7 are indicated on the spectrum shown in Figure 5.5. The extrapolation of the -7 slope to a wave number of 2 rad/m (corresponding to the radar wavelength of 3 m) gives an estimated power of 3×10^{-10} $(\Delta N/N)^2$ m/rad. This leads to a scattering cross-section per unit volume of 4×10^{-18} m^{-1}, in satisfactory agreement with that obtained from the radar data [ROYRVIK AND SMITH, 1984].

The spectrum includes a range of wave numbers where the slope is -5/3, indicating turbulence in the neutral atmosphere. The wave number

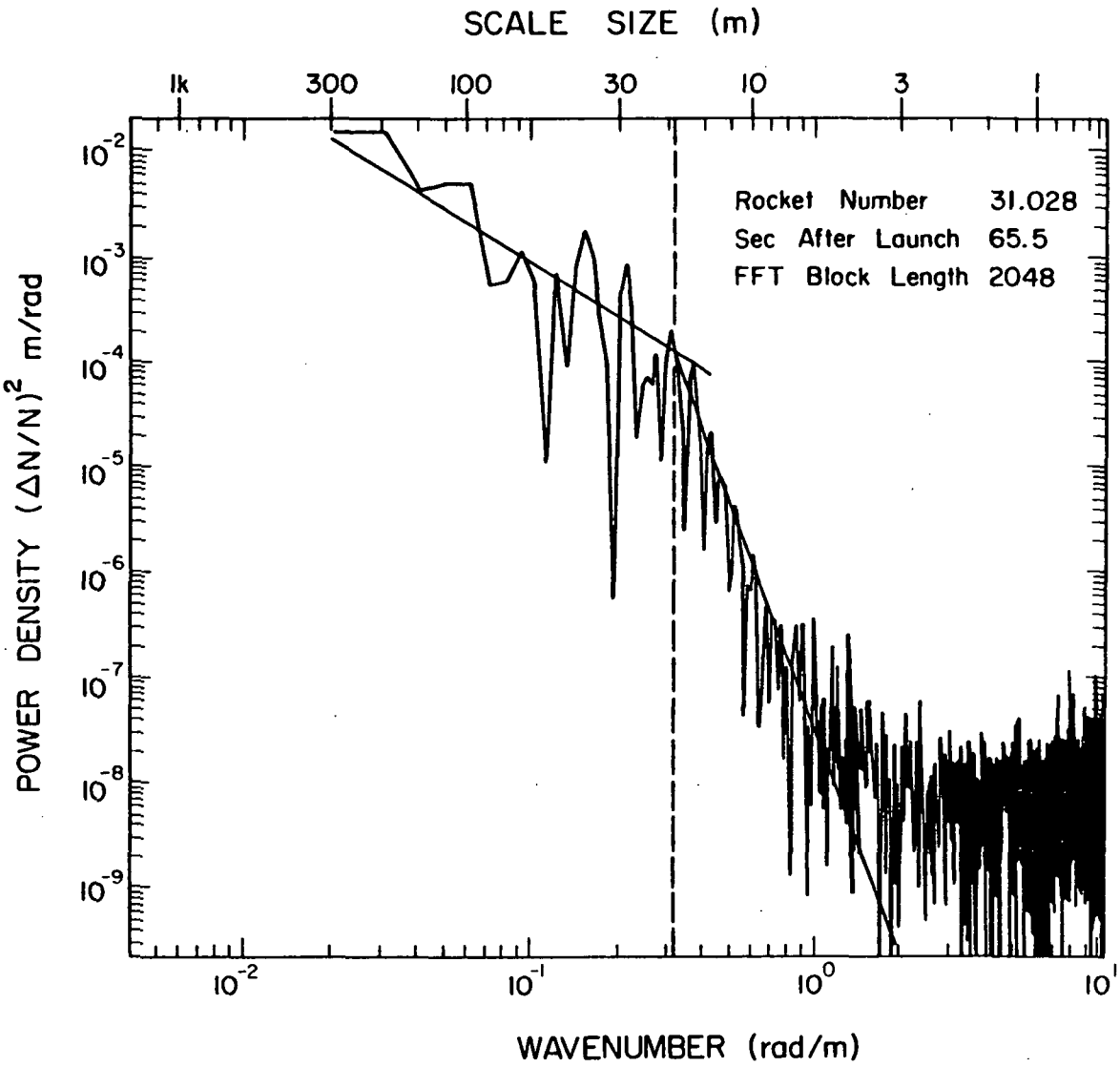

Figure 5.5. Spectrum of mesospheric irregularities at an altitude of 85.5 km.

at the intersection of the -5/3 and -7 slopes is interpreted as the inner scale of turbulence. The value, 0.3 rad/m (frequency: 75 Hz; scale size: 20m), agrees with estimates of RASTOGI AND BOWHILL [1976]. The comparison of rocket and radar data is discussed in detail in ROYRVIK AND SMITH [1984].

A feature of the data which is not discussed in ROYRVIK AND SMITH (1984] is the double-peaked nature of the irregularities in the layer. This is most clearly seen in Figure 5.4 in the frequency bands 20-40 Hz and 40-80 Hz. If the turbulence originates in a shear layer which has become unstable, it follows that the electron density gradient in the center of the turbulent layer will be small, whereas there will be steep gradients at the upper and lower boundaries [PELTIER ET AL., 1978]. An analogous effect has been noted by SMITH AND MILLER [1980] in sporadic-E layers associated with unstable wind shears. Since the irregularities are related to the local gradient of refractive index, the strongest irregularities may be expected to occur at the boundaries of the turbulent layer.

The steepening of the electron density gradients at the upper and lower boundaries, and the corresponding decrease of gradient within the layer can be seen in Figure 5.6. This is an expanded section of the profiles of Figure 5.2. The boundaries of the layer, at 85.2 and 86.5 km, are indicated on the profile for 31.028. The corresponding section of the other profile (31.029) is relatively smooth within this region, consistent with the absence of echoes in the radar data or of irregularities in the rocket data.

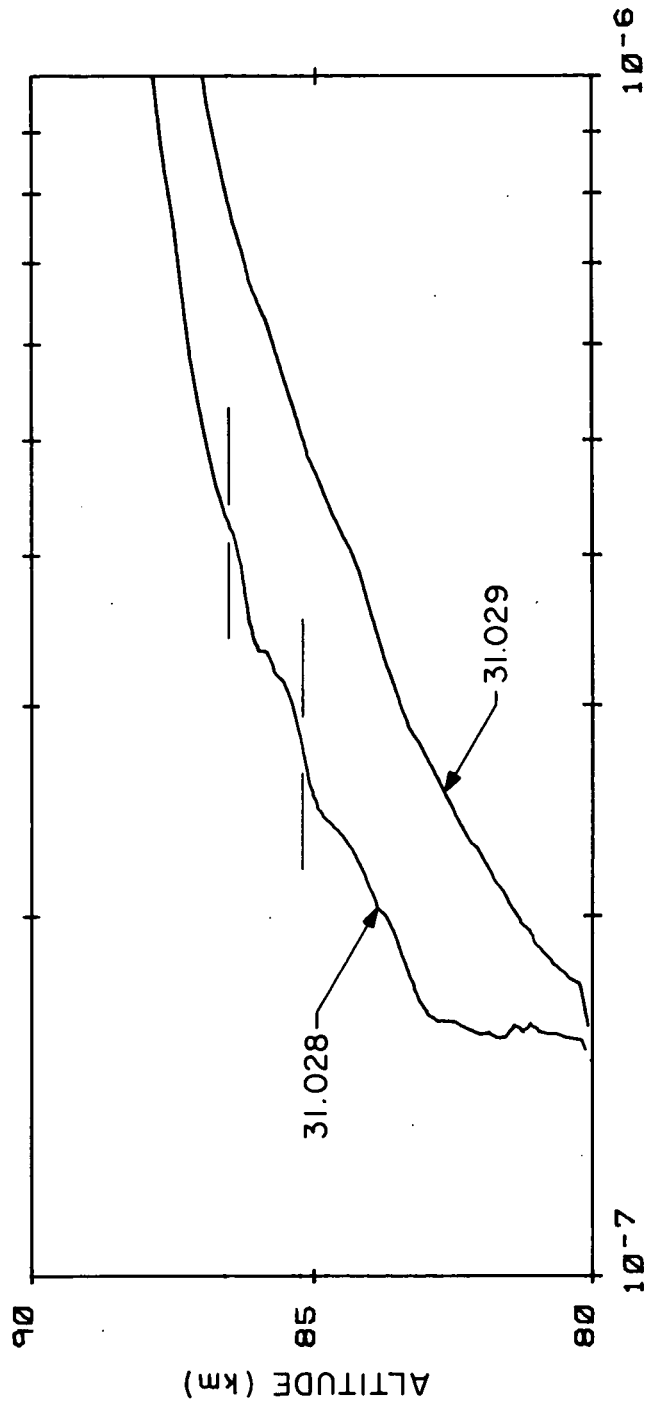

Figure 5.6. Enlarged section of probe current profiles showing steepened gradients in layer of mesospheric irregularities.

PRAKASH ET AL. [1980], in reviewing the results of many rocket flights at the equatorial site at Thumba, India, identify irregularities due to neutral turbulence. For medium-scale irregularities (30 to 300 m), which they have observed in the altitude range 70 to 81 km, the average spectral index is -2.7 ± 0.4. Small-scale irregularities (1 to 15 m), observed in the altitude range 61 to 70 km, showed a more variable spectral index with an average value of -1.6 ± 0.7 (i.e., about -5/3). We have attributed these apparent small-scale irregularities to payload vibration and the apparent medium-scale irregularities to spin-related components of probe current (see Figure 5.3 and the related discussion).

5.4.2 Electrojet irregularities. The spectrum shown in Figure 5.7 is obtained from Nike Orion 31.028 at an altitude of 96 km. The rocket velocity is 1.45 km/s and the elevation angle is 81.5 deg. This is in the lower part of the electrojet and these are the Type 2 irregularities of the equatorial electrojet. They are generated by the gradient-drift instability and have been extensively studied by ground-based radio experiments.

The altitude range of the Type 2 irregularities is, from Figure 5.4, about 90 to 105 km. They have larger-scale components than can be represented in Figure 5.4. These are visible in the profile of probe current, Figure 5.2. They are shown again in Figure 5.8 with expanded scales and with a separation introduced by multiplying the probe current of 31.029 by the factor of 1.5. The large-scale irregularities are

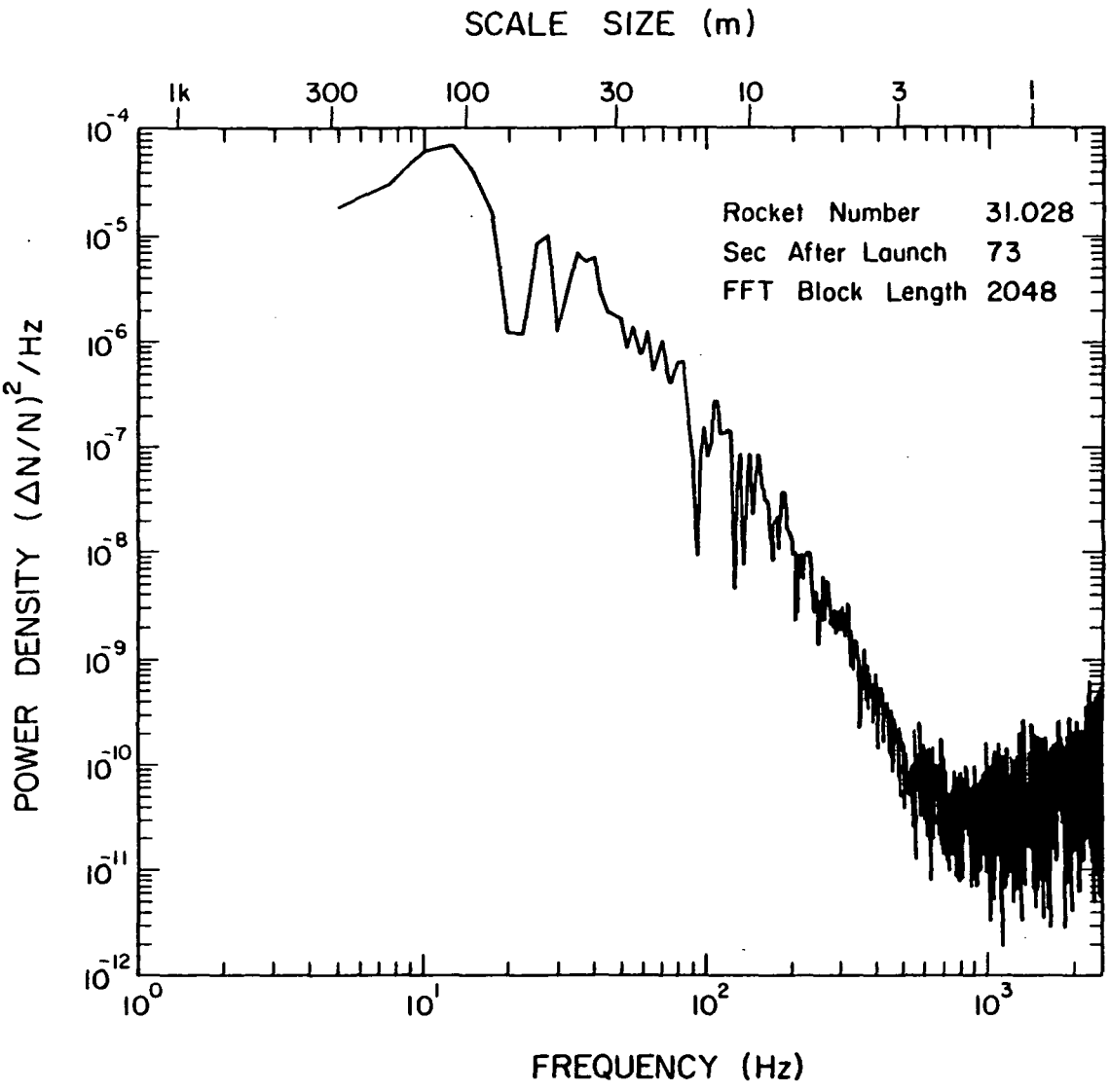

Figure 5.7. Spectrum of electrojet irregularities at an an altitude of 96 km.

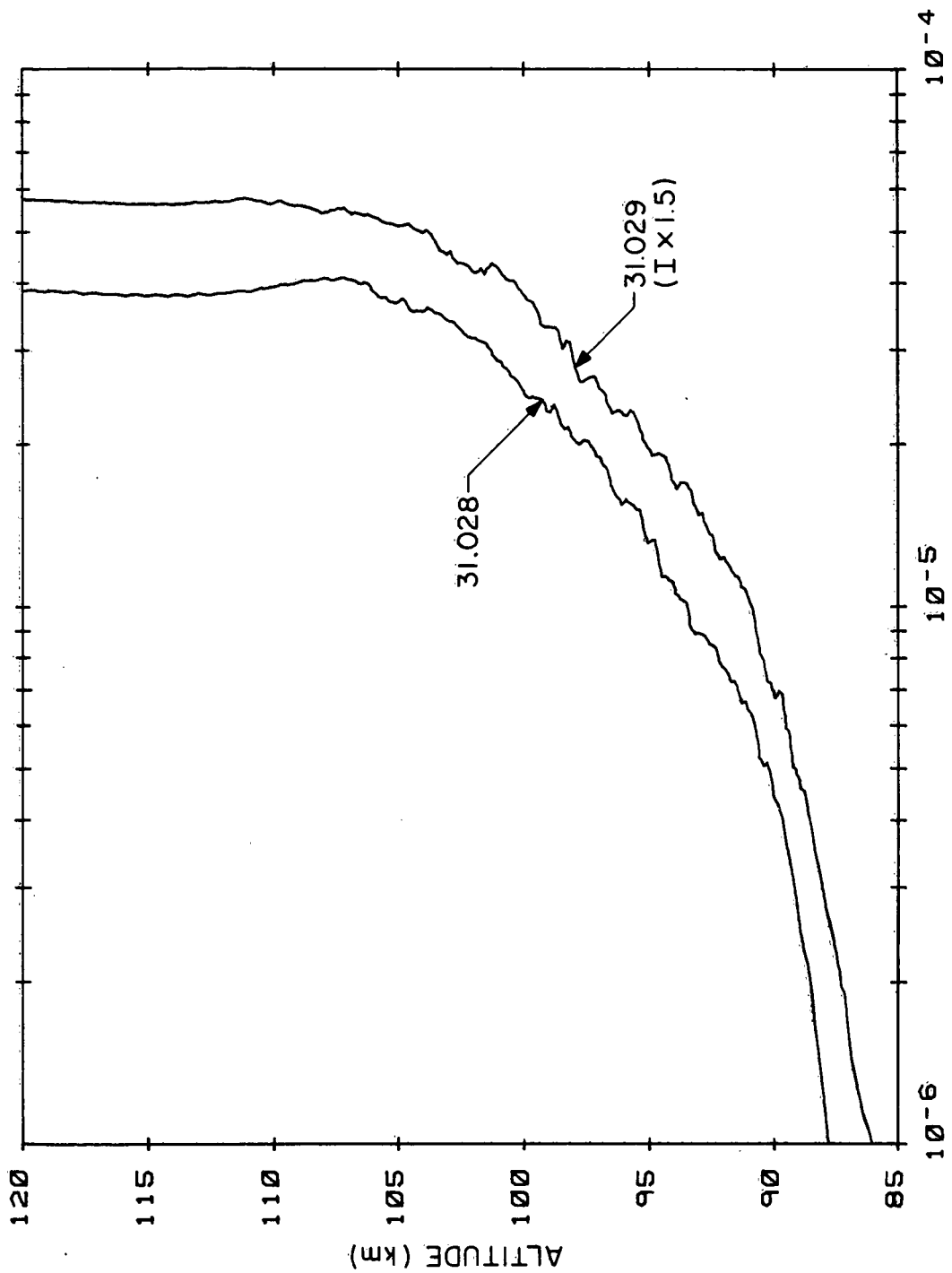

Figure 5.8 Enlarged section of probe current profiles showing large-scale irregularities in the electrojet.

responsible for a strong scintillation of the signal which was observed in the 5 MHz radiowave propagation experiment. This aspect of the data will not be discussed.

The spectral index of the spectrum shown in Figure 5.7 is about -3 for frequencies below 200 Hz (scale size > 7 m). At higher frequencies (until obscured by system noise) the magnitude appears to increase. PRAKASH ET AL. [1980], in daytime flights, find the spectral index to be -2.0 ± 0.7 for the medium-scale irregularities (30 to 300 m) and to be between -4 and -2 for the small-scale irregularities (1 to 15 m). Our observations are not substantially different from these.

Type 1 irregularities are seen in both flights in the upper part of the electrojet (in the altitude range 103 to 108 km). As seen in Figure 5.4 they are more pronounced in the second flight (31.029) than in the first (31.028). There is considerable structure within the few kilometer thickness of the region. This is seen most clearly at the higher frequencies (>160 Hz). The sharply defined upper and lower boundaries (on 31.029) can be noted, as well as the separate peak at 103 km. The mechanism producing the Type 1 irregularities has been generally considered to be the two-stream instability.

The spectrum observed on Nike Orion 31.029 at 106.5 km is shown in Figure 5.9. The rocket velocity is 1.38 km/s and the elevation angle is 79.7 deg. Except at low frequencies (spin-related components) the slope is close to zero. PRAKASH ET AL. [1980] also report a flat spectrum for the Type 1 irregularities.

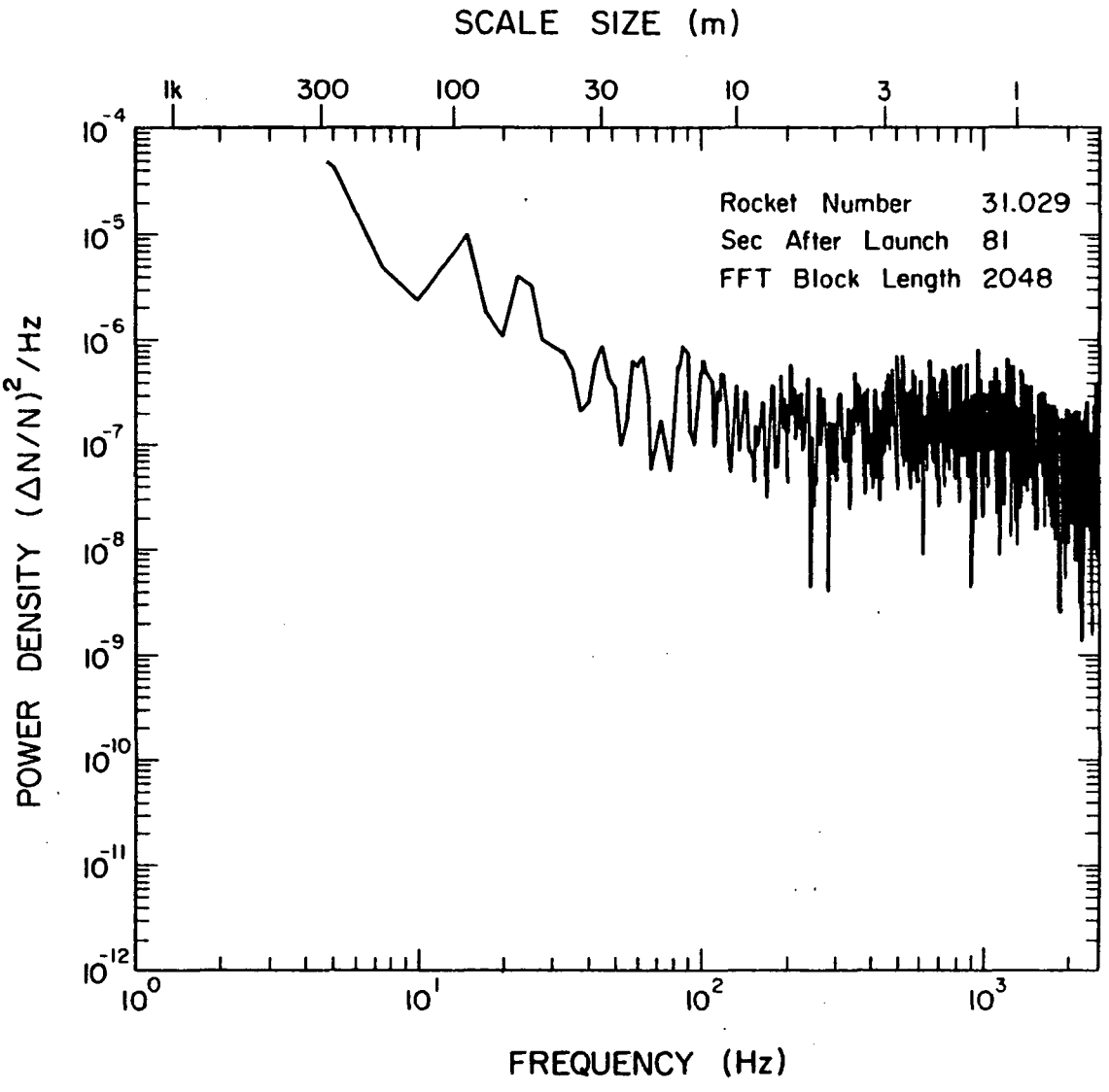

Figure 5.9. Spectrum of Type 1 irregularitites in the electrojet at an altitude of 106.5 km.

The irregularities seen in the rocket data are several orders of magnitude stronger than can be deduced from echoes obtained from a vertically directed radar, even during very strong scattering conditions [IERKIK, 1980]. The scattering cross section per unit volume (at 3 m wavelength) is calculated from the rocket data to be 7×10^{-9} m^{-1}. This is comparable with estimates by IERKIK [1980] for strong Type 1 irregularities observed in the horizontal direction.

5.4.3 Upper E-region irregularities. The upper boundary of the electrojet is seen in Figure 5.4 to be sharply defined. Above the electrojet, however, there are electron density irregularities of much smaller amplitude which can be detected to an altitude of about 170 km. The altitude profile of these irregularities in the frequency band 240 to 480 Hz is shown in Figure 5.10. This frequency range is chosen so that, with the changing rocket velocity, the 3 m wavelength components (to which the radar is sensitive) are included.

The radar at Jicamarca, on both occasions, recorded echoes between 140 and 170 km, but not between 110 and 140 km. Spectra from the rocket experiment, such as the one at 132 km from Nike Orion 31.028 shown in Figure 5.11, indicate a small positive slope of 0.4 ± 0.2 throughout the region (The velocity is 1.20 km/s and the elevation angle is 79.5 deg) .

In order to reconcile the rocket and radar data, it is suggested that the irregularities are plane waves which are aligned almost vertically at the lowest altitudes but more obliquely at increasing

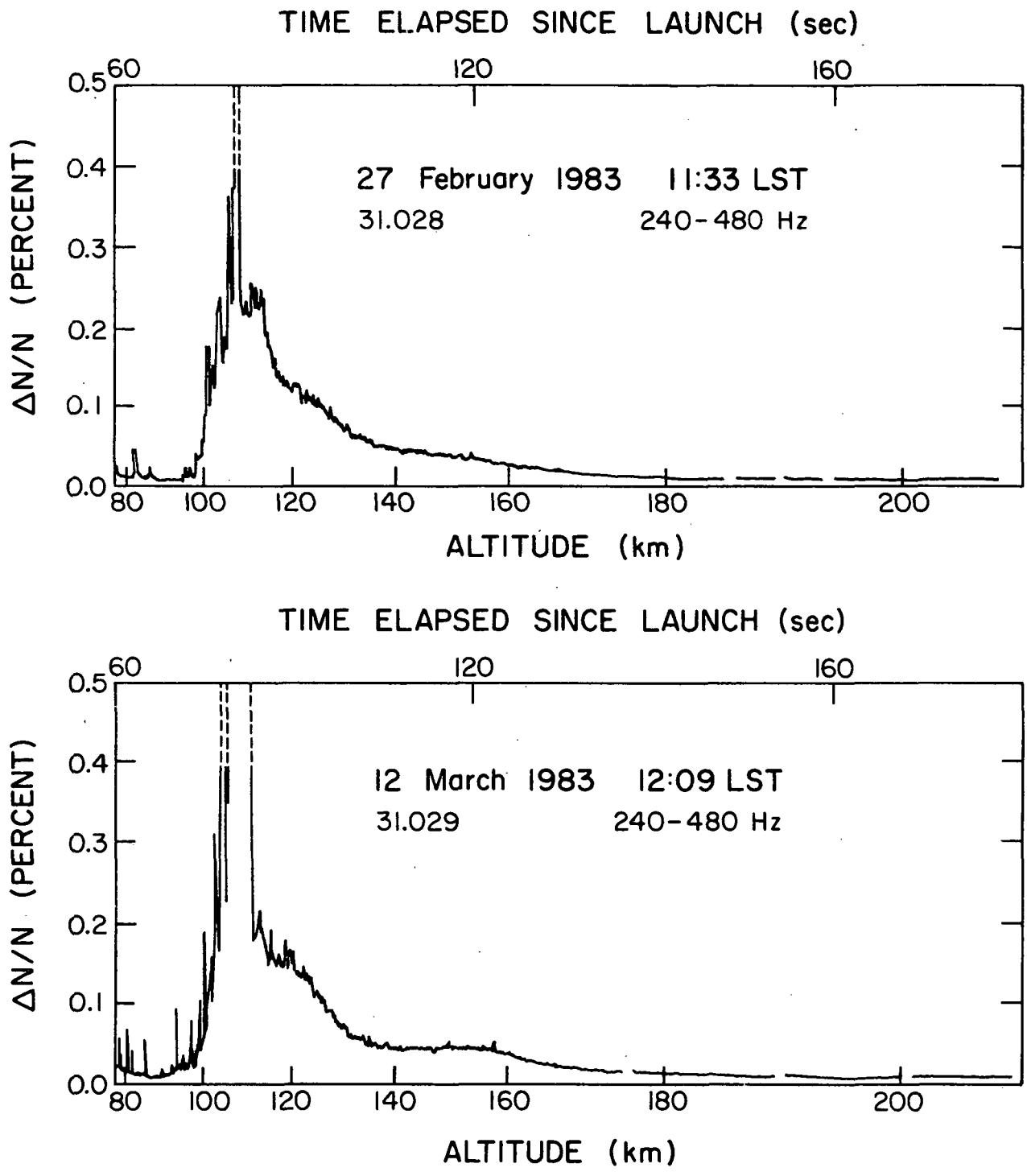

Figure 5.10. Irregularity amplitude in frequency band 240 - 480 Hz as a function of altitude.

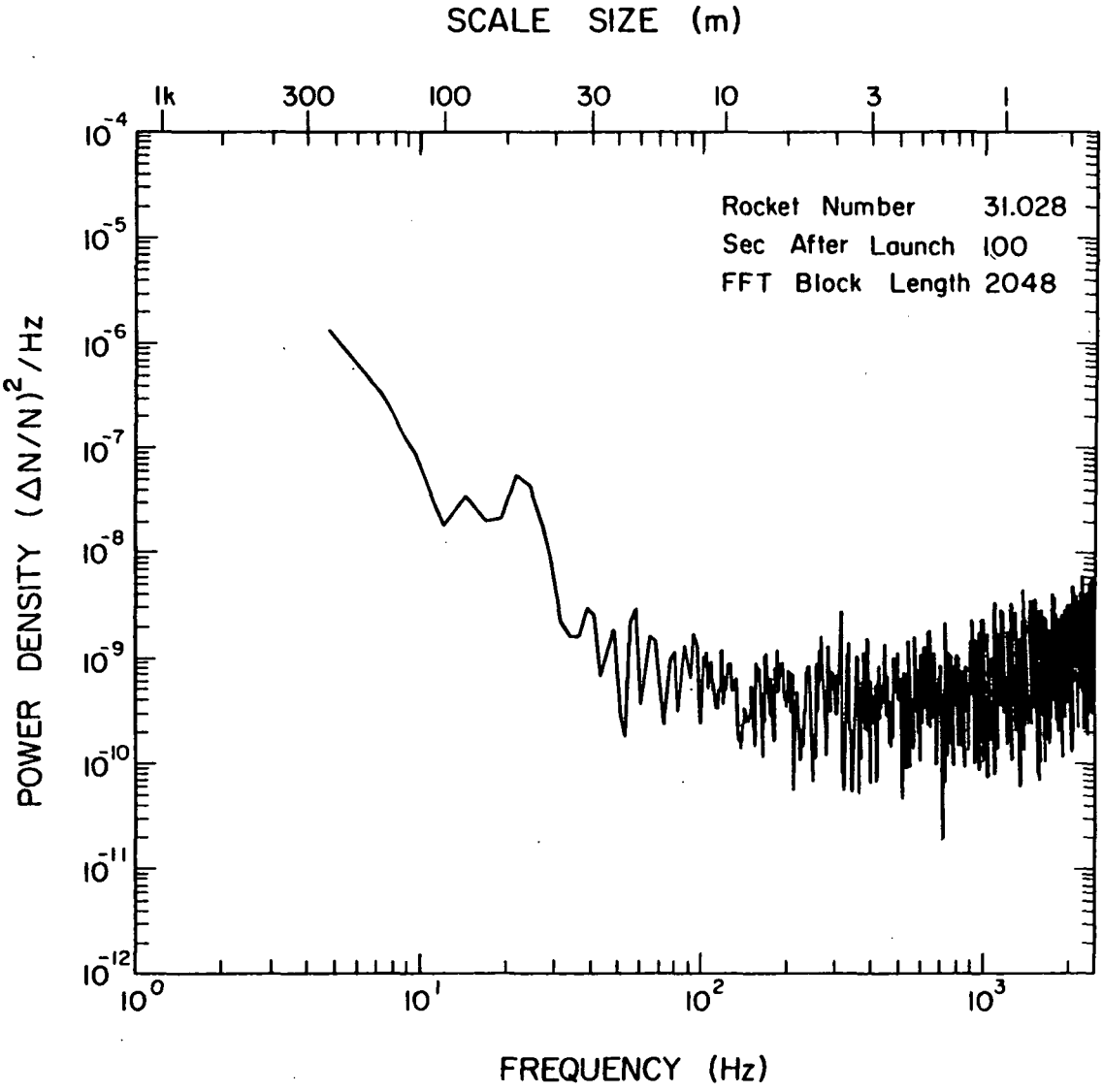

Figure 5.11. Spectrum of irregularities at an altitude of 131 km in the upper E region.

altitudes. It is also suggested that this idea could be tested with further experiments using the Jicamarca radar.

The irregularities of the upper E region have been reported previously by SMITH AND KLAUS [1978] and by PRAKASH ET AL. [1980]. The amplitudes are comparable when correction is made for the different bandwidths used.

No satisfactory explanation for the occurrence of the upper E-region irregularities has yet been given although the similarity of the spectrum to that of the Type 1 irregularities may be noted.

6. CONCLUSIONS AND SUGGESTIONS FOR FUTURE WORK

6.1 Conclusions

Electron density irregularity measurements were performed by the Aeronomy Laboratory of the University of Illinois in the auroral and equatorial ionosphere during the Energy Budget Campaign in 1980 and Project Condor in 1983. The measurements were obtained by monitoring the current drawn through a rocket-borne probe held at constant potential and amplifying the resulting signal for transmission to a ground-based telemetry station. The fine structure signal was then calibrated and spectral estimates were computed for specific altitudes using an interactive FORTRAN algorithm developed specifically for analysis of the fine structure experiment. Preliminary spectra were obtained for Taurus Orion 33.011 in the auroral ionosphere and Nike Orions 31.028 and 31.029 in the equatorial ionosphere. The conclusions drawn from each follow.

6.1.1 Energy Budget Campaign. On the basis of the spectra presented here, and those from THRANE AND GRANDAL [1981], it may be premature to conclude that the mesospheric irregularities are due to three-dimensional neutral atmosphere turbulence of the Kolmogorov type. In the absence of any other plausible nonturbulent mechanism, however, the similarities between the observed and theoretical spectra (-5/3 slope at small wave numbers, the steeper slope at larger wave numbers and the changing break point as a function of altitude) strongly suggest that some kind of turbulence is responsible for the electron density irregularities. The differences between auroral and equatorial

mesospheric spectra (in the apparent inner scale value and in the spectral slope at large wave numbers) may or may not be significant. Not enough is known about temporal and latitudinal variations of energy dissipation rate and kinematic viscosity to decide if the wave number of the observed break in the spectral slope can be reconciled with turbulence theory. The -7 and -3 spectral indices may result from attempts to fit straight lines to a curve that is actually the exponential function of wave number predicted by simple turbulence theory. In this case the discrepancy between the -7 and -3 slopes is unimportant. If, on the other hand, subsequent observations should confirm the power law, then the different slopes become important and must be explained. Further experimental data and theoretical studies are needed to resolve these problems.

6.1.2 Project Condor. It has not been possible to detect irregularities in the ambient electron density at altitudes much below 80 km because of instrumental noise apparently generated by vibration of the payload. Previous reports of irregularities at low altitudes must be reconsidered before they can be taken as evidence of neutral atmosphere turbulence.

At altitudes above 80 km it is possible to see evidence of neutral atmosphere turbulence. In the region from 80 km to the lower limit of the electrojet (near 90 km), in two rocket flights, only one layer of turbulence was found. The radar and rocket data from the layer are in satisfactory agreement and support isotropic neutral turbulence.

The Type 2 irregularities of the equatorial electrojet are seen on both rocket flights in the altitude range of 90 to 105 km. These are dominated by large-scale components, are about equal in intensity on the two occasions and are considered to be generated by the gradient-drift instability.

The Type 1 irregularities of the electrojet have different intensities on the two flights; those on the second flight (31.029) being much greater in amplitude and extending over a greater altitude range (103 to 108 km). The irregularities originate in the two-stream instability.

The rocket data from both flights show irregularities in the upper E region continuously from the electrojet (near 110 km) up to an altitude of about 170 km. They have the same flat spectrum as the Type 1 irregularities but amplitudes that are smaller by several orders of magnitude. There are radar echoes from 140 to 170 km on both occasions but none between the electrojet and 140 km. This is possibly related to the anisotropic nature of the irregularities. The properties have not yet been well enough defined to allow an identification of the mechanism generating the upper E-region irregularities.

6.2 Suggestions for Future Work

In the near term, the capabilities of Program SPECTRA should be exploited to further refine the analysis in order to maximize the amount of information extracted from the data. Also further qualification of the data may be achieved by reducing dependence on assumptions.

Preliminary analyses were performed on the data in Chapters 4 and 5 to obtain initial results from the rocket flights and to serve as a baseline for more detailed analyses. For example, the software's capability for data "windowing" may be utilized to decrease the leakage of the spin harmonics into higher frequencies of the spectra. Determination of an optimum window function could thereby increase the accuracy with which large scale size irregularities are computed. Likewise, data segmenting and spectral averaging may be performed for variance reduction in the spectral estimate. Decreasing the variance of the estimate might allow more accurate computations of spectral indices as well as better defined transitions in spectral slope. Data segmenting and spectral averaging may however be more important in the context of stationarity tests.

As was mentioned in Section 3.2.6, Fourier analysis rests on the premise that the data are stationary (i.e., the spectrum is time-invariant). A spectral estimate of nonstationary data is suspect and highly unreliable. The fine structure spectrum, however, does change with time and therefore, extreme care must be taken when performing spectral analysis. Experimentation with data segmenting and observation of the resulting individual periodograms may help to determine the rate at which the spectrum is changing thereby indicating an upper bound on data segment length over which Fourier analysis is valid. In addition, further information regarding the irregularity structure in the ionosphere may be obtained.

In the long term, it may prove worthwhile to investigate the more advanced spectral estimation techniques which are described in the literature under maximum entropy spectral estimation, autoregressive-moving average (ARMA) modelling, etc. These modern techniques produce estimates which are unbiased, consistent and of equal or better quality than the classical estimators. In addition, they are more amenable to dealing with nonstationary random data.

REFERENCES

Balsley, B. B., W. L. Ecklund, and D. C. Fritts [1983], VHF echoes from the high-latitude mesosphere and lower thermosphere observations and interpretations, J. Atmos. Sci., 40, 2451.

Brigham, E. O. [1974], The Fourier Transform, Prentice Hall, Inc., Englewood Cliffs, NJ.

Dewan, E. M., N. Grossband, A. F. Quesada, and R. I. Good [1984], Spectral analysis of 10 m resolution scalar velocity profiles in the stratosphere, Geophys. Res. Lett., 11, 80-83.

Durkin, C., and L. G. Smith [1981], A rocket-borne Langmuir probe for high resolution measurement of the ionospheric electron temperature profile, Aeronomy Report No. 95, Aeron Lab., Dept. Elec. Eng., Univ. of Ill., Urbana-Champaign.

Fejer, B. G., and M. C. Kelley [1980], Ionospheric irregularities, Rev. Geophys. Space Phys., 18, 401-454.

France, L. A., and E. R. Williams [1976], An improved Faraday rotation experiment for rocket measurements of lower ionosphere electron concentrations, J. Atmos. Terr. Phys., 38, 957-964.

Harris, F. J. [1978], On the use of windows for harmonic analysis with the discrete Fourier transform, Proc. IEEE, 66, 51-83.

Hirao, K., and K. Oyama [1972], Profiles of electron temperature in the ionosphere observed with electron temperature probe on a rocket, Space Research XII, 1335-1339.

Ierkic, H. M. [1980], Ph.D. Thesis, Cornell University.

Jacobsen, T. A., and M. Friedrich [1979], Electron density measurements in the lower D-region, J. Atmos. Terr. Phys., 41, 1195-1200.

Kay, S. M., and S. L. Marple, Jr. [1981], Spectrum analysis--a modern perspective, Proc. IEEE, 69, 1380-1419.

Klaus, D. E., and L. G. Smith [1978], Rocket observations of electron-density irregularities in the equatorial ionosphere below 200 km, Aeronomy Report No. 80, Aeron. Lab., Dept. Elec. Eng., Univ. of Ill., Urbana-Champaign.

Peltier, W. R., J. Halle, and T. L. Clark [1978], Geophys., Astrophys., Fluid Dynamics, 10, 53.

Prakash, S., B. H. Subbaraya, and S. P. Gupta [1972], Rocket measurements of ionization irregularities in the equatorial ionosphere at Thumba and identification of plasma instabilities, Ind. J. Radio Space Phys., 1, 72-80.

Prakash, S., S. P. Gupta, B. H. Subbaraya, and R. Pandey [1980], A review of the electron density irregularities in the equatorial D and E region, Low Latitude Aeronomic Process, edited by A. P. Mitra, Pergamon, 3.

Rastogi, P. K., and S. A. Bowhill [1976], Scattering of radio waves from the mesosphere - 2. Evidence for intermittent mesospheric turbulence, J. Atmos. Terr. Phys., 38, 449.

Royrvik, O., and L. G. Smith [1984], Comparison of mesospheric VHF radar echoes and rocket probe electron-concentration measurements. J. Geophys. Res., 89, 9014-9022.

Smith, L. G. [1964], COSPAR Information Bulletin No. 17 (edited by K. Maeda), 37.

Smith, L. G. [1967], Langmuir probes for measurements in the ionosphere, Revised version of Tech. Manual Series, COSPAR Bulletin No. 17 (edited by K. Maeda).

Smith, L. G. [1969], Langmuir probes in the ionosphere, Small Rocket Inst. Techniques, (edited by K. Maeda), North Holland, Amsterdam.

Smith, L. G., and D. E. Klaus [1978], Rocket observations of electron density irregularities in the equatorial E-region, Space Res., 18, 261.

Smith, L. G., and K. L. Miller [1980], J. Atmos. Terr. Phys., 42, 45.

Tatarskii, V. I. [1971], The effects of turbulent atmosphere on wave propagation, Translated from Russian, Israel Program for Scientific Translations Ltd., U.S. Dept. of Commerce, NTIS, Springfield, Virginia.

Thrane, E. V., and B. Grandal [1981], Observations of fine scale structure in the mesosphere and lower thermosphere, J. Atmos. Terr. Phys., 43, 179.

Welch, P. D. [1967], The use of the fast Fourier transform for the estimation of power spectra: a method based on time averaging over short, modified periodograms, IEEE Trans. Aud. and Elec., 2, 70-73.

Zimmerman, R. K., Jr., and L. G. Smith [1980], Rocket measurements of electron temperature in the E-region, Aeronomy Report No. 92, Aeron. Lab., Dept. Elec. Eng., Univ. of Ill., Urbana-Champaign.

ORIGINAL PAGE IS
OF POOR QUALITY

APPENDIX

PROGRAM SPECTRA AND RELATED SUBROUTINES

```
PROGRAM SPECTRA IS AN INTER-ACTIVE ROUTINE WHICH ALLOWS THE
COMPUTATION OF POWER SPECTRA TO BE USED IN THE CALCULATION
OF FINE STRUCTURE IRREGULARITIES.  THE FINE STRUCTURE DATA
FILE TO BE ANALYZED IS ENTERED THROUGH DEVICE 3.  THE USER
IS THEN PROMPTED TO PROVIDE INFORMATION REGARDING THE DATA
AND THE ANALYSIS.  A LINEAR FIT MAY ALSO BE PERFORMED ON
THE DATA AND THE SPECTRAL INDEX CALCULATED.  THE USER MAY
STORE VALUES OF THE SPECTRAL INDEX AND MAGNITUDE IN ARRAY
INDEX.  PROGRAM SPINDEX MAY THEN BE USED TO PLOT THE
SPECTRAL INDEX AND MAGNITUDE AS A FUNCTION OF ALTITUDE.
   PRIOR TO EXECUTION OF SPECTRA, THE USER MUST PROVIDE
CERTAIN PARAMETERS.  THESE PARAMETERS ARE
        1) GAIN --  THIS IS THE GAIN OF THE EXPERIMENT.
        2) CHANNEL --  THIS REFERS TO THE CHANNEL NUMBER
                       OF THE REQUIRED DATA AS STORED ON
                       A CDC FORMAT TAPE.
        3) MINMAG --  THIS IS THE LOWER BOUNDARY ON THE
                      PLOTTING AXIS.
        4) BANDCAL --  THIS IS THE ARRAY WHICH CONTAINS
                       THE DATA CALIBRATIONS AS DETERMINED
                       FROM PROGRAM CWALCAL.
        5) LOLIMIT --  LOLIMIT IS THE LOWER BOUND ON THE
                       FREQUENCY OF DATA POINTS TO BE INCLUDED
                       IN THE LEAST SQUARES FIT.
        6) HILIMIT --  HILIMIT IS THE UPPER BOUND ON THE
                       FREQUENCY OF DATA POINTS TO BE INCLUDED
                       IN THE LEAST SQUARES FIT.
        7) FC  --  THIS IS THE UPPER 3DB FREQUENCY OF THE
                   TELEMETRY LOW PASS FILTER.
        8) FAC --  THIS IS THE UPPER 3DB FREQUENCY OF THE
                   AC AMPLIFIER.
        9) FLE --  THIS IS THE UPPER 3DB FREQUENCY OF THE
                   LOGARITHMIC ELECTROMETER.
       10) BBAND --  THIS IS THE NUMBER OF THE BROADBAND
                     AMPLIFIER OUTPUT BEING PROCESSED.  (TO
                     BYPASS DEEMPH, SET BBAND .EQ. 0)
THESE VALUES ARE ENTERED UNDER THE TITLE "EXPERIMENT
PARAMETERS" IN THE PROGRAM.  (WRITTEN BY BRUCE TOMEI, 1983).


      PROGRAM SPECTRA (INPUT,OUTPUT,DATA11,INDEX,TAPE1=INPUT,
     *                 TAPE2=OUTPUT,TAPE3=DATA11,TAPE4=INDEX)
      INTEGER N,K,M,OVLP,WINDOW,DISPLAY,OPTION,CHANNEL,IHRS,IMIN,S,
     *        NUMBER,FIT1,FIT2,REPEAT,M2,BBAND
      REAL DATA(4096),MAG(2049),MAGAVE(2049),FREQ(2049),X(4096),
     *     BANDCAL(5),MAXMAG,MAXFREQ,LTIME,STIME,SMPTIME,SECS,GAIN,
     *     MINMAG,KREAL,SLOPE,YINT,HILIMIT,LOLIMIT,FC,FAC,FLE
      COMPLEX Z(2049)
      EXTERNAL CABS
      DATA Z,DATA,MAG,MAGAVE,X,FREQ/2049*((0.0,0.0)),4096*(0.0),
     *     2049*(0.0),2049*(0.0),4096*(0.0),2049*(0.0)/

ENTER USER-SPECIFIED VARIABLES

      PRINT*,"ENTER THE LAUNCH TIME.  (HH MM SEC.)"
      READ*,IHRS,IMIN,SECS
      LTIME=FLOAT(IHRS*3600+IMIN*60)+SECS
10    PRINT*,"ENTER THE DESIRED STARTING TIME.  (SECONDS AFTER LAUNCH)"
      READ*,STIME
      IF(REPEAT .EQ. 1)GOTO 50
```

```
      PRINT*,"ENTER THE NUMBER OF DATA POINTS."
      READ*,N
      PRINT*,"ENTER THE SEGMENT LENGTH (MUST BE AN EVEN INTEGER)"
      READ*,L
      PRINT*,"        NUMBER OF SEGMENTS          OVERLAP"
      S=N/L
      PRINT4,S,0
      IF(S .EQ. 1) GOTO 40
      DO 100 I=2,L
        KREAL=FLOAT(N-(I-1))/FLOAT(L-(I-1))
        IF(KREAL-AINT(KREAL))10P,20
 20     K=IFIX(KREAL)
        PRINT4,K,I-1
  4     FORMAT(13X,I4,19X,I4)
100   CONTINUE
 40   PRINT*,"ENTER THE NUMBER OF SEGMENTS DESIRED"
      READ*,K
      OVLP=(L*K-N)/(K-1)
      PRINT*,"ENTER THE DESIRED WINDOW.     1-RECTANGULAR"
      PRINT*,"                              2-BARTLETT"
      PRINT*,"                              3-HANNING"
      PRINT*,"                              4-HAMMING"
      PRINT*,"                              5-BLACKMAN"
      PRINT*,"                              6-BLACKMAN-HARRIS"
      READ*,WINDOW
      PRINT*,"ENTER THE FFT BLOCK LENGTH  (MUST BE A POWER OF 2)"
      READ*,M
      M2=M/2+1
      PRINT*,"ENTER THE DESIRED PLOT.       1-LINEAR"
      PRINT*,"                              2-LOGARITHMIC"
      PRINT*,"                              3-NO PLOT"
      READ*,OPTION
      FIT2=2
      DISPLAY=2
      FIT1=1
      IF(OPTION .EQ. 3)GOTO 70
      IF(K .EQ. 1)GOTO 30
      PRINT*,"DO YOU WISH TO PLOT INDIVIDUAL PERIODOGRAMS?    1-YES"
      PRINT*,"                                                2-NO"
      READ*,DISPLAY
      IF(DISPLAY .EQ. 2)GOTO 30
      PRINT*,"HOW MANY INDIVIDUAL PLOTS?"
      READ*,NUMBER
      PRINT*,"PERFORM LINEAR FIT TO INDIVIDUAL PERIODOGRAMS?    1--YES"
      PRINT*,"                                                  2--NO"
      READ*,FIT2
 30   PRINT*,"PERFORM LINEAR FIT TO AVERAGED PERIODOGRAM?   1--YES"
      PRINT*,"                                              2--NO"
      READ*,FIT1
 70   PRINT*,"ANY CHANGES?              1-YES"
      PRINT*,"                          2-NO"
      READ*,S
      IF(S .EQ. 1)GOTO 10

   EXPERIMENT PARAMETERS

      GAIN=24.7
      CHANNEL=2
      MINMAG=0.0000000001
      BANDCAL(1)=1256.94
      BANDCAL(2)=1142.81
```

ORIGINAL PAGE IS
OF POOR QUALITY

```
      BANDCAL(3)=2038.60
      BANDCAL(4)=2938.65
      BANDCAL(5)=3836.41
      LOLIMIT=100.0
      HILIMIT=1000.0
      FC=1050.0
      FAC=2000.0
      FLE=2500.0
      BBAND=0

    BEGIN PROCESSING

50    REWIND 3
      CALL LOAD(DATA,N,CHANNEL,LTIME,STIME,SMPTIME)
      CALL CALIB(DATA,N,BANDCAL,GAIN)
      CALL SPECTRM(DATA,MAG,MAGAVE,FREQ,X,Z,N,K,M,M2,L,OVLP,WINDOWNO,
     *             SMPTIME,OPTION,DISPLAY,NUMBER,MINMAG,FIT,
     *             LOLIMIT,HILIMIT,FC,FAC,FLE,BBAND,LTIME,STIME)
      CALL FILTCAL(MAGAVE,FREQ,M2,FC,FAC,FLE)
      CALL DEEMPH(MAGAVE,FREQ,M2,BBAND)
      CALL MAXMIN(MAGAVE,FREQ,MAXMAG,MAXFREQ,M,M2)
      CALL PLOTTER(MAGAVE,FREQ,M,M2,MAXMAG,MINMAG,MAXFREQ,OPTION,
     *             SLOPE,YINT,FIT,LOLIMIT,HILIMIT)
      PRINT*,"DO YOU WISH TO STORE THE SPECTRAL INDEX?     1--YES"
      PRINT*,"                                             2--NO"
      READ*,S
      IF(S .EQ. 2)GOTO 60
      CALL STORE(SLOPE,YINT,LTIME,STIME,SMPTIME,N)

60    PRINT*,"ARE YOU FINISHED?                 1-YES"
      PRINT*,"                                  2-NO"
      READ*,S
      IF(S .EQ. 1)STOP
      PRINT*,"NEW TIME, SAME ANALYSIS?     1--YES"
      PRINT*,"                             2--NO"
      READ*,REPEAT
      GOTO 10
      STOP
      END
```

```
  SUBROUTINE LOAD READS A SPECIFIED CHANNEL FROM A
  PDP2COC CONVERTED TAPE AND STORES THIS DATA IN ARRAY
  DATA.  THE NUMBER OF DATA POINTS TO BE READ AND THE
  TIME CORRESPONDING TO THE FIRST DATA POINT ARE ENTERED
  BY THE USER.  IF THE STARTING TIME ENTERED DOES NOT
  CORRESPOND TO A SPECIFIC DATA POINT, THE FIRST DATA
  POINT OF THE DESIRED CHANNEL FOLLOWING THE GIVEN
  STARTING TIME WILL BE THE FIRST TO BE READ.  FOLLOWING
  IS A LIST OF THE SUBROUTINE VARIABLES.
  (NOTE -- THE NUMBER IN PARENTHESES IN THE READ STATEMENT
  SPECIFIES THE DEVICE TO BE READ.  THIS SHOULD BE MODIFIED
  IN ACCORDANCE WITH THE USER'S PROGRAM STATEMENT.)

    DATA     =ARRAY CONTAINING THE CHANNEL SAMPLES.
    N        =NUMBER OF SAMPLES TO BE READ.
    LTIME    =LAUNCH TIME IN UNIVERSAL TIME (IN SECONDS).
```

```
      STIME    =TIME CORRESPONDING TO THE FIRST SAMPLE TO BE
                READ (IN SECONDS FROM LAUNCH).
      PTIME    =TIME CORRESPONDING TO FIRST SAMPLE IN A RECORD.
      SMPTIME  =CHANNEL SAMPLING PERIOD.
      TIME     =TIME OF DATA POINT IN UNIVERSAL TIME (LTIME+
                STIME).
      FRAME    =THE FRAME NUMBER (A FRAME IS A SET OF FIVE DATA POINTS).
      CHANNEL  =THE DESIRED CHANNEL TO BE READ.
      POINT    =THE DATA POINT CORRESPONDING TO TIME
      IPOINT   =THE LARGEST INTEGER LESS THAN OR EQUAL TO POINT.
      STPOINT  =THE FIRST DATA POINT TO BE READ (STARTING POINT).


      SUBROUTINE LOAD (DATA,N,CHANNEL,LTIME,STIME,SMPTIME)
      REAL DATA(N),ARRAY(1251),LTIME,STIME,TIME,SMPTIME,PTIME,POINT
      INTEGER IARRAY(1250),IPOINT,STPOINT,CHANNEL
      EQUIVALENCE(ARRAY(2),IARRAY(1))
      TIME=LTIME+STIME
      READ(3) ARRAY
      PTIME=ARRAY(1)
      READ(3) ARRAY
      SMPTIME=(ARRAY(1)-PTIME)/250.0
      REWIND 3
   10 READ(3) ARRAY
      IF(ARRAY(1) .GT. TIME)GOTO 20
      GOTO 10
   20 BACKSPACE 3
      BACKSPACE 3
      READ(3) ARRAY
      POINT=(TIME-ARRAY(1))/(SMPTIME/5.0)+1.0
      IPOINT=POINT
      IF(POINT-FLOAT(IPOINT) .LT. 0.000001) GOTO 30
      IPOINT=IPOINT+1
      IF(IPOINT .LE. 1250) GOTO 30
      READ(3) ARRAY
      IPOINT=1
   30 FRAME=(IPOINT-1)/5+1
      STPOINT=(FRAME-1)*5+CHANNEL
      IF(IPOINT .LE. STPOINT) GOTO 40
      STPOINT=STPOINT+5
      IF(STPOINT .LE. 1250) GOTO 40
      READ(3) ARRAY
      STPOINT=CHANNEL
   40 DO 100 I=1,N
        DATA(I)=FLOAT(IARRAY(STPOINT))
      STPOINT=STPOINT+5
      IF(STPOINT .LE. 1250) GOTO 100
      READ(3) ARRAY
      STPOINT=CHANNEL
  100 CONTINUE
      RETURN
      END



   SUBROUTINE CALIB PERFORMS THE NECESSARY
   CALIBRATIONS SO THAT THE DATA IS REPRESENTATIVE
   OF THE OUTPUT FROM THE EXPERIMENT.  THESE
   CALIBRATIONS INCLUDE ADJUSTMENTS FOR EXPERIMENT
```

```
GAIN, DIGITIZER GAIN, SIGNAL OFFSETS, AND
DISCRIMINATOR NON-LINEARITIES.  THE NON-LINEARITIES
ARE REMOVED WITH A CALIBRATION CURVE OBTAINED BY
A PIECEWISE-LINEAR FIT TO THE CALIBRATION VALUES
(BANDCAL(5)).

      SUBROUTINE CALIB (DATA,N,BANDCAL,GAIN)
      REAL DATA(N),BANDCAL(5),GAIN
      INTEGER N
      DO 100 I=1,N
        IF(DATA(I) .GT. BANDCAL(2)) GOTO 10
        DATA(I)=((1.25/(BANDCAL(2)-BANDCAL(1)))*DATA(I)
     *          -(1.25*BANDCAL(1)/(BANDCAL(2)-BANDCAL(1)))-2.5)/GAIN
        GOTO 100
   10   IF(DATA(I) .GT. BANDCAL(3)) GOTO 20
        DATA(I)=((1.25/(BANDCAL(3)-BANDCAL(2)))*DATA(I)
     *          -(1.25*BANDCAL(2)/(BANDCAL(3)-BANDCAL(2)))-1.25)/GAIN
        GOTO 100
   20   IF(DATA(I) .GT. BANDCAL(4)) GOTO 30
        DATA(I)=((1.25/(BANDCAL(4)-BANDCAL(3)))*DATA(I)
     *          -(1.25*BANDCAL(3)/(BANDCAL(4)-BANDCAL(3))))/GAIN
        GOTO 100
   30   DATA(I)=((1.25/(BANDCAL(5)-BANDCAL(4)))*DATA(I)
     *          -(1.25*BANDCAL(4)/(BANDCAL(5)-BANDCAL(4)))+1.25)/GAIN
  100 CONTINUE
      RETURN
      END



SUBROUTINE SPECTRM SEGMENTS THE DATA, REMOVES THE MEAN,
WINDOWS THE DATA, COMPUTES THE PERIODOGRAM, UPDATES AN
AVERAGE OF THE PERIODOGRAMS, AND THEN DISPLAYS THE
INDIVIDUAL PERIODOGRAMS.  AN AVERAGED PERIODOGRAM IS
OBTAINED UPON RETURN FROM THE SUBROUTINE.

      SUBROUTINE SPECTRM(DATA,MAG,MAGAVE,FREQ,X,Z,N,K,M,M2,L,OVLP,
     *                   WINDOWNO,SMPTIME,OPTION,DISPLAY,NUMBER,MINMAG,
     *                   FIT2,LOLIMIT,HILIMIT,FC,FAC,FLE,BBAND,
     *                   LTIME,STIME)
      INTEGER N,K,M,M2,OVLP,D,L,WINDOWNO,IWK(12),DISPLAY,OPTION,
     *        NUMBER,S,BBAND,V
      REAL DATA(N),MAG(M2),MAGAVE(M2),FREQ(M2),X(M),MEAN,WK(1),
     *     SMPTIME,MAXMAG,MINMAG,MAXFREQ,LOLIMIT,HILIMIT,FC,FAC,FLE,
     *     LTIME,STIME,SLOPE,YINT
      COMPLEX Z(M2)

INITIALIZE ARRAYS

      DO 100 I=1,M2
        MAGAVE(I)=0.0
        Z(I)=((0.0,0.0))
  100 CONTINUE
      DO 700 I=1,M
        X(I)=0.0
  700 CONTINUE
      D=(N-OVLP)/K
```

```
      S=1

   BEGIN SPECTRAL ESTIMATION

      DO 200 J=1,K

   READ IN THE APPROPRIATE DATA SEGMENT.

      DO 300 I=1,L
        X(I)=DATA(I+(J-1)*O)
300   CONTINUE

   MEAN REMOVAL

      MEAN=0.0
      DO 400 I=1,L
        MEAN=MEAN+(X(I)-MEAN)/FLOAT(I)
400   CONTINUE
      DO 500 I=1,L
        X(I)=X(I)-MEAN
500   CONTINUE

   APPLY WINDOW TO DATA.

      CALL WINDOW(X,L,M,WINDONO)

   COMPUTE PERIODOGRAM

      CALL FFTRC(X,M,Z,IWK,WK)
      DO 800 I=1,M2          (OPTIONAL)
        Z(I)=CONJG(Z(I))     (OPTIONAL)
800   CONTINUE               (OPTIONAL)
      DO 600 I=1,M2
        MAG(I)=(2.0*SMPTIME/FLOAT(L))*(CABS(Z(I)))**2
        FREQ(I)=(I-1)/(FLOAT(M)*SMPTIME)
600   CONTINUE

   AVERAGE PERIODOGRAMS

      DO 900 I=1,M2
        MAGAVE(I)=(1.0/FLOAT(K))*MAG(I)+MAGAVE(I)
900   CONTINUE

   DISPLAY INDIVIDUAL PERIODOGRAM

      IF(DISPLAY .EQ. 2)GOTO 200
      IF(S .GT. NUMBER)GOTO 200
      CALL FILTCAL(MAG,FREQ,M2,FC,FAC,FLE)
      CALL DEEMPH(MAG,FREQ,M2,BBAND)
      CALL MAXMIN(MAG,FREQ,MAXMAG,MAXFREQ,M,M2)
      CALL PLOTTER(MAG,FREQ,M,M2,MAXMAG,MINMAG,MAXFREQ,OPTION,SLOPE,
     *             YINT,FIT2,LOLIMIT,HILIMIT)
      IF(FIT2 .EQ. 2)GOTO 10
      PRINT*,"DO YOU WISH TO STORE THE SPECTRAL INDEX?   1--YES"
      PRINT*,"                                           2--NO"
      READ*,V
      IF(V .EQ. 1)CALL STORE(SLOPE,YINT,LTIME,STIME,SMPTIME,N)
 10   S=S+1
200   CONTINUE
   RESTORE ARRAY FREQ
      DO 999 I=1,M2
        FREQ(I)=(I-1)/(FLOAT(M)*SMPTIME)
999   CONTINUE
```

ORIGINAL PAGE IS
OF POOR QUALITY

```
      RETURN
      END
```

SUBROUTINE MAXMIN CALCULATES THE VALUES OF MAXMAG,
AND MAXFREQ AND ROUNDS THEM TO APPROPRIATE VALUES FOR AXES
PLOTTING.

```
      SUBROUTINE MAXMIN(MAG,FREQ,MAXMAG,MAXFREQ,M,M2)
      INTEGER M,M2
      REAL MAG(M2),FREQ(M2),MAXMAG,MAXFREQ
      MAXMAG=0.0
      MAXFREQ=FREQ(M2)
      DO 100 I=1,M2
        IF(MAG(I) .GT. MAXMAG) MAXMAG=MAG(I)
100   CONTINUE
      CALL LIMITS(MAXMAG)
      RETURN
      END
```

SUBROUTINE FILTCAL PERFORMS A CALIBRATION TO THE SPECTRUM
IN ORDER TO COMPENSATE FOR THE ROLLOFF EFFECTS OF THE
TELEMETRY FILTER, THE AC AMPLIFIER, AND THE LOGARITHMIC
ELECTROMETER. THE TELEMETRY FILTER IS MODELED AS AN
IDEAL 3-POLE LOW PASS FILTER (SEE ZIMMERMAN,1980). THE
AC AMPLIFIER AND LOG ELECTROMETER ROLLOFFS ARE MODELLED
AS SINGLE POLE LOW PASS FILTERS. THE INPUT PARAMETERS
ARE

```
        FC  --  THE UPPER 3DB FREQUENCY OF THE TELEMETRY FILTER.
       FAC  --  THE UPPER 3DB FREQUENCY OF THE AC AMPLIFIER.
       FLE  --  THE UPPER 3DB FREQUENCY OF THE LOG ELECTROMETER.
```

HC,HAC,HLE ARE THE MAGNITUDES SQUARED OF THE TRANSFER FUNCTIONS
CORRESPONDING TO THE RESPECTIVE FILTER.

```
      SUBROUTINE FILTCAL(MAG,FREQ,M2,FC,FAC,FLE)
      INTEGER M2
      REAL MAG(M2),FREQ(M2),OMEGA,PI,WC,WAC,WLE
      PI=3.14159265
      WC=2.0*PI*FC
      WAC=2.0*PI*FAC
      WLE=2.0*PI*FLE
      DO 100 I=1,M2
        OMEGA=2.0*PI*FREQ(I)
        HC=7.75138*WC**6/(((2.10199*WC**2-OMEGA**2)**2
     *     +8.40165*(WC*OMEGA)**2)*(1.75480*WC**2
     *     +OMEGA**2))
        HAC=WAC**2/(WAC**2+OMEGA**2)
        HLE=WLE**2/(WLE**2+OMEGA**2)
        MAG(I)=MAG(I)/(HC*HAC*HLE)
100   CONTINUE
      RETURN
      END
```

```
C
C  SUBROUTINE DEEMPH PERFORMS DE-EMPHASIS ON THE SPECTRUM
C  OBTAINED FROM THE FINE STRUCTURE EXPERIMENT.  THE PRE-EMPHASIS
C  FILTER IS MODELED AS A SINGLE-POLE HIGH PASS FILTER WITH
C  CUTOFF FREQUENCY EQUAL TO THAT OF THE BROADBAND AMPLIFIER.
C  THE DE-EMPHASIS FILTER IS THEN OBTAINED BY TAKING THE INVERSE
C  OF THE PRE-EMPHASIS FILTER TRANSFER FUNCTION.  DE-EMPHASIS
C  IS REQUIRED FOR PAYLOADS 31,028, 31,029, AND ANY OTHER
C  PAYLOADS WITH THE SAME EXPERIMENT CONFIGURATION.  THE
C  PARAMETERS ARE
C     1) BBAND  --  THIS NUMBER REFERS TO THE NUMBER OF THE
C                   BROADBAND AMPLIFIER WHOSE OUTPUT IS UNDER
C                   ANALYSIS.  FOR BBAND .EQ. 0, DE-EMPHASIS
C                   IS BYPASSED.
C     2) WC  --  THIS IS THE LOWER 3DB CUTOFF FREQUENCY OF THE
C                BROADBAND AMPLIFIER.
C     3) HDE --  THIS IS THE MAGNITUDE SQUARED OF THE DE-EMPHASIS
C                FILTER TRANSFER FUNCTION.
C
      SUBROUTINE DEEMPH(MAG,FREQ,M2,BBAND)
      INTEGER M2,BBAND
      REAL MAG(M2),FREQ(M2),PI,OMEGA,WC,HDE
      PI=3.1415926
      IF(BBAND .EQ. 0)RETURN
C
C PERFORM DE-EMPHASIS
C
      WC=2.0*PI*400.0
      IF(BBAND .EQ. 2) WC=2.0*PI*40.0
      DO 100 I=2,M2
        OMEGA=2.0*PI*FREQ(I)
        HDE=(OMEGA**2+WC**2)/OMEGA**2
        MAG(I)=HDE*MAG(I)
100   CONTINUE
      RETURN
      END
C
C
C
C  SUBROUTINE PLOTTER PLOTS THE POWER DENSITY VERSUS
C  FREQUENCY OR SCALE SIZE  IN LINEAR OR LOGARITHMIC FORM.
C  A LINEAR FIT MAY ALSO BE PERFORMED ON THE LOGARITHMIC PLOT.
C
      SUBROUTINE PLOTTER (MAG,FREQ,M,M2,MAXMAG,MINMAG,MAXFREQ,OPTION,
     *                    SLOPE,YINT,FIT,LOLIMIT,HILIMIT)
      INTEGER M,M2,OPTION,FIT,J
      REAL MAG(M2),FREQ(M2),MAXMAG,MINMAG,MAXFREQ,YINT,SLOPE,
     *     LOLIMIT,HILIMIT,X1(3),Y1(3)
C
C INITIALIZE PLOTTING PARAMETERS
```

ORIGINAL PAGE IS
OF POOR QUALITY

```
      CALL USTART
      CALL USET("XBOTHLABEL")
      CALL USET("YBOTHLABEL")
      CALL USET("OWNSCALE")
      CALL UPSET("XLABEL","F")
      CALL UPSET("YLABEL","F")
      CALL UPSET("TERMINATOR",";")
      CALL UPSET("VERTICAL",3.0)
      CALL UPSET("HORIZONTAL",2.0)
      CALL USET("SOFTWARE")
      CALL UDAREA(0.0,7.0,0.0,5.7)
      CALL UPRINT(40.0,2.0,"FREQUENCY   (HZ)")
      CALL UMOVE(4.0,0.0)
      CALL URUTAT(90.0)
      CALL UPRINT(25.0,0.0,"POWER DENSITY    (DELTA N/N) /HZ")
      CALL UPRINT(79.0,1.5,"2")
      CALL USET("HARDWARE")
      CALL USET("SYSTEM")

    THE FOLLOWING THREE STATEMENTS MAY BE USED TO
    SUPERCEDE THE OUTPUT OF SUBROUTINE MAXMIN.  IF
    THIS IS DESIRED, REMOVE THE COMMENT MARKERS.

      MINMAG=10E-12          (OPTIONAL)
      MAXMAG=10E-5           (OPTIONAL)
      MAXFREQ=1000.0         (OPTIONAL)

      CALL UWINDO(0.0,MAXFREQ,0.0,MAXMAG)
      IF(OPTION .EQ. 2)GOTO 10

    PERFORM LINEAR PLOTTING

      CALL UPLOT1(FREQ,MAG,FLOAT(M2))
      GOTO 20

    PERFORM LOGARITHMIC PLOTTING

 10   CALL UWINDO(1.0,MAXFREQ,MINMAG,MAXMAG)
      CALL USET("XYLOGARITHMIC")
      CALL USET("LOGXAXIS")
      CALL USET("LOGYAXIS")
      J=0
      DO 100 I=1,M2
        IF(MAG(I) .EQ. 0.0) MAG(I)=MINMAG
        IF(FREQ(I) .LE. MAXFREQ) J=J+1
100   CONTINUE
      FREQ(1)=0.01
      CALL UPLOT1(FREQ,MAG,FLOAT(J))
      CALL UFLUSH
      CALL UPAUSE


    PERFORM LINEAR LEAST-SQUARES FIT.


      IF(FIT .EQ. 2)RETURN
      FREQ(1)=0.0

    FLAG DATA POINTS WITH MAGNITUDE EQUAL TO ZERO
    OR WITH FREQUENCY OUT OF LIMITS.
```

```
      DO 200 I=2,M2
        IF(FREQ(I) .LT. LOLIMIT)FREQ(I)=0.0
        IF(FREQ(I) .GT. HILIMIT)FREQ(I)=0.0
        IF(MAG(I) .EQ. MINMAG)FREQ(I)=0.0
        IF(MAG(I) .EQ. 0.0)FREQ(I)=0.0
200   CONTINUE

  REMOVE FLAGGED DATA POINTS AND COMPRESS DATA

      J=1
      DO 300 I=1,M2
        IF(FREQ(I) .EQ. 0.0)GOTO 300
        MAG(J)=ALOG10(MAG(I))
        FREQ(J)=ALOG10(FREQ(I))
        J=J+1
300   CONTINUE

  PERFORM LINEAR FIT

      CALL ULINFT(FREQ,MAG,FLOAT(J-1),SLOPE,YINT)

  GENERATE FITTED CURVE (THREE POINTS ONLY)

      X1(1)=LOLIMIT
      Y1(1)=(10.0**YINT)*(X1(1)**SLOPE)
      X1(2)=(LOLIMIT+HILIMIT)/2.0
      Y1(2)=(10.0**YINT)*(X1(2)**SLOPE)
      X1(3)=HILIMIT
      Y1(3)=(10.0**YINT)*(X1(3)**SLOPE)

  PLOT FITTED LINE

      CALL USET("LINE")
      CALL USET("OLDSCALE")
      CALL UPLOT1(X1,Y1,3.0)
 20   CALL UFLUSH
      CALL UPAUSE
      CALL UERASE
      CALL UEND
      RETURN
      END



  SUBROUTINE STORE STORES THE SPECTRAL INDEX DATA IN ARRAY
  INDEX IN THE FOLLOWING FORMAT-  TIME,SPECTRAL INDEX,
  MAGNITUDE.  ARRAY INDEX THEN SERVES AS THE INPUT ARRAY
  FOR PROGRAM SPINDEX.


      SUBROUTINE STORE (SLOPE,YINT,LTIME,STIME,SMPTIME,N)
      INTEGER N
      REAL SLOPE,YINT,LTIME,STIME,SMPTIME,AVTIME
      AVTIME=((LTIME+STIME)+(FLOAT(N)*SMPTIME))/2.0
      WRITE(4,11) AVTIME,SLOPE,(10.0**YINT)
11    FORMAT(1X,F9.2,1X,F10.5,1X,E13.6)
      RETURN
      END
```

```
C  SUBROUTINE WINDOW APPLIES A SPECIFIED WINDOW TO THE DATA
C  SEGMENT X.  THE WINDOW IS SPECIFIED BY WINDONO.  THE
C  WINDOWED DATA IS ALSO NORMALIZED BY THE INCOHERENT
C  POWER GAIN OF THE WINDOW (IPG).

      SUBROUTINE WINDOW (X,L,M,WINDONO)
      INTEGER L,J,R,WINDONO,M
      REAL X(M),PI,IPG
      PI=3.14159265
      GOTO(10,20,30,40,50,60)WINDONO

C  RECTANGULAR WINDOW

 10   RETURN

C  BARTLETT WINDOW

 20   J=L/2
      R=J+1
      IPG=0.0
      DO 100 I=1,J
        WEIGHT=FLOAT(I-1)/FLOAT(J)
        X(I)=X(I)*WEIGHT
        IPG=WEIGHT**2+IPG
100   CONTINUE
      DO 200 I=R,L
        WEIGHT=FLOAT(L-I+1)/FLOAT(J)
        X(I)=X(I)*WEIGHT
        IPG=WEIGHT**2+IPG
200   CONTINUE
      IPG=IPG/FLOAT(L)
      DO 201 I=1,L
        X(I)=X(I)/SQRT(IPG)
201   CONTINUE
      RETURN

C  HANNING WINDOW

 30   IPG=0.375
      DO 300 I=1,L
        WEIGHT=0.5*(1.0-COS(2.0*PI*(I-1)/L))
        X(I)=X(I)*WEIGHT/SQRT(IPG)
300   CONTINUE
      RETURN

C  HAMMING WINDOW

 40   IPG=0.3974
      DO 400 I=1,L
        WEIGHT=0.54-0.46*COS(2.0*PI*(I-1)/L)
        X(I)=X(I)*WEIGHT/SQRT(IPG)
400   CONTINUE
      RETURN

C  BLACKMAN WINDOW
```

```
 50   IPG=0.3046
      DO 500 I=1,L
        WEIGHT=0.42-0.5*COS(2.0*PI*(I-1)/L)+0.08*COS(4.0*PI*(I-1)/L)
        X(I)=X(I)*WEIGHT/SQRT(IPG)
500   CONTINUE
      RETURN

   BLACKMAN-HARRIS WINDOW (4-TERM)

 60   IPG=0.289672277
      DO 600 I=1,L
        WEIGHT=0.40217-0.49703*COS(2.0*PI*FLOAT(I-1)/L)
     *         +0.09392*COS(4.0*PI*FLOAT(I-1)/L)
     *         -0.00183*COS(6.0*PI*FLOAT(I-1)/L)
        X(I)=X(I)*WEIGHT/SQRT(IPG)
600   CONTINUE
      RETURN
      END



   SUBROUTINE LIMITS ROUNDS THE VALUE OF MAX FOR EASE IN AXES
   PLOTTING.  FOR 10**(N+1) > MAX > 10**N , (N GREATER THAN OR
   EQUAL TO 1.0), LIMITS ROUNDS THE VALUE OF MAX UP TO THE
   NEXT (N-1)TH POWER OF TEN.  FOR 10**-(N-1) > MAX > 10**-N ,
   (N LESS THAN 1.0), LIMITS ROUNDS THE VALUE OF MAX UP TO
   THE NEXT -(N+1)TH POWER OF TEN.

      SUBROUTINE LIMITS (MAX)
      REAL Z,Y,FACTOR,MAX,DELTA
      IF(MAX .GE. 10.) GOTO 10
      DO 100 I=1,15
        Z=10.0**(I-14)
100   IF(MAX .GT. Z)FACTOR=10.0**(I-14)
      Y=(AINT(10.0*MAX/FACTOR))/10.0
      MAX=FACTOR*(Y+.1)
      RETURN
 10   DO 200 I=1,8
        Z=10.0**I
200   IF(MAX .GT. Z)FACTOR=10.0**(I-1)
      DELTA=0.0
      IF(AMOD(MAX,FACTOR) .GE. 0.0001)DELTA=1.0
      MAX=FACTOR*(AINT(MAX/FACTOR)+DELTA)
      RETURN
      END
```